The Complete Electrode Model in Bioelectromagnetism: Analysis, Implementation and Evaluation

by

Fatih Karpuz

A master thesis in mathematics

at the
University of Münster
2025

Supervision was given by
First Supervisor: Professor Doctor Christian Engwer
Second Supervisor: Professor Doctor Carsten Wolters

Declaration of Academic Integrity

I hereby confirm that this thesis on “The Complete Electrode Model in Bioelectromagnetism: Analysis, Implementation and Evaluation” is solely my own work and that I have used no sources or aids other than the ones stated. All passages in my thesis for which other sources, including electronic media, have been used, be it direct quotes or content references, have been acknowledged as such and the sources cited.

I agree to have my thesis checked in order to rule out potential similarities with other works and to have my thesis stored in a database for this purpose.

Acknowledgements

I want to thank my first supervisor Prof. Dr. Christian Engwer for offering me the topic for my thesis in this interdisciplinary field of mathematics, informatics, and neuroscience with its clear application. Working on this thesis was a very enriching experience and answered a lot of questions for me.

I want to thank my second supervisor Prof. Dr. Carsten Wolters in whose work-group SIM-Neuro at the Institute for Biomagnetism and Biosignalanalysis I spent most of my time for the thesis. He offered me a great environment for my work. I want to thank him for his suggestions, guidance and also for the opportunity to write my thesis in this interdisciplinary field. The talks we had during lunch breaks were always very interesting and exciting.

A big thank you also goes to the doctoral student Malte Höltershinken, who I was lucky enough to share an office with. His patience, extraordinary enthusiasm, and expertise in his work taught me a lot and are a big reason why writing this thesis was such a wonderful and enriching experience. He was always very open to questions and discussions and contributed a large part of the supervision.

I thank Prof. Dr. Sampsa Pursiainen for the kind welcome and discussions at the Tampere University and for the great time we spent there.

This work was supported by DAAD project 57756407; by ERA PerMed as project ERAPERMED2020-227, PerEpi (Bundesministerium für Gesundheit (BMG), project ZMI1-2521-FSB006, by the Deutsche Forschungsgemeinschaft (DFG), projects WO1425/10-2 and WO1425/11-1 and by DFG through the Cluster of Excellence ”Mathematics Münster: Dynamics - Geometry - Structure” (EXC 2044-390685587). I want to thank them for supporting this project.

Last but not least, I want to thank my family and friends for their great support. Sevginiz ve desteğiniz için çok mutluyum.

Contents

List of Figures

List of Tables

Chapter 1

Introduction

Neurological disorders such as Alzheimer's disease, Parkinson's disease, and epilepsy continue to present substantial challenges to researchers and clinicians. An essential step in developing more effective therapies is to improve the understanding of the complex structure of the brain and the way it functions. To achieve this, both non-invasive and invasive techniques are employed to measure, modulate, and analyze neural activity. Among the most prominent techniques are electroencephalography (EEG) [4], intracranial EEG (iEEG) [51], transcranial electrical stimulation (tES) [52], and deep brain stimulation (DBS) [6].

EEG and iEEG enable the observation of electrical brain activity by measuring voltage differences on the scalp or directly within the brain, respectively. In both cases, there is an important computational challenge which is the inverse problem in which we determine the location and magnitude of the neural sources from measured potentials. Solving this inverse problem requires that we solve the associated forward problem, which is the computation of the electric potential in the head given a source in the brain, often using source spaces with 10^4 nodes (i.e., solving the forward problem 10^4 times). Therefore, accurate and efficient numerical solvers for the forward problem are needed.

To model the electric potential in the head, we use a quasi-static approximation of Maxwell's equations which is very common in the field of bioelectromagnetism, which leads to a second-order elliptic partial differential equation (PDE) defined over an inhomogeneous domain Ω [4]. Due to the complex geometry of the human head and the discontinuities in tissue conductivities, these equations cannot be solved analytically in realistic head models and must instead be solved or approximated using numerical methods. In this work, we use the finite element method (FEM), which handles the complex geometries and material interfaces present in realistic head models well [20].

A crucial aspect of the modeling of bioelectric fields that is based on FEM is the representation of electrodes. The most common used model is the point electrode model (PEM) [19], where electrodes are treated as points on the boundary of the domain in the EEG and tES case and as points in the volume conductor for the iEEG and DBS case. This model is computationally efficient [19] and widely used, but neglects physical effects such as the spatial extent of the electrodes. In contrast, the complete electrode model (CEM) [37][53] takes into account both the geometric area of the electrodes and the contact impedance between the electrode and the tissue, leading to a more realistic model. The CEM was shown to be relevant in neonatal EEG [38].

This thesis presents the implementation and evaluation of the CEM within the DUNEuro software framework, which provides FEM-based solutions for problems in bioelectromagnetism [47][20]. While the PEM is already supported in DUNEuro, this work includes the CEM for applications in EEG, tES and also iEEG and DBS.

The main contributions of this work are the following:

The CEM is mathematically analyzed and implemented in DUNEuro for EEG, iEEG, tES, and DBS simulations and is compared with PEM in these modalities. Although studies are made for the comparison of CEM and PEM in EEG and tES [37][39][12], the cases of iEEG and DBS are conducted for the first time with this thesis. In addition, a short investigation of the use of the CEM for epicranial application of stimulation electrodes is given. The local subtraction source model [20] is extended to support CEM, allowing more accurate source modeling in complex head geometries, including interesting interfaces such as electrode-brain interfaces in iEEG and DBS. The convergence behavior of the CEM toward the PEM is analyzed by letting the electrode radius increase to zero to show the theoretical link between the CEM and the PEM. The principle of reciprocity [60][55] is mathematically demonstrated for the CEM and is used to simplify the implementation of stimulation solvers by using the existing EEG and iEEG solvers for tES and DBS respectively. The Schur complement and transfer matrix approach [62] are applied to the CEM to enable efficient repeated forward computations, which is needed to significantly decrease the computation time in solving the inverse problem.

Extensive numerical experiments are made in both spherical and realistic head models to investigate the differences between the CEM and PEM across various modalities. These include for the spherical head models the EEG and iEEG measurement setups as well as stimulation settings for tES and DBS. For EEG and tES, we also use a realistic head model. Here, attention is also given to the impact of electrode size and contact impedance and the convergence of the CEM to PEM for electrode interfaces that consist of a single boundary face and higher impedances.

The remainder of the thesis is structured as follows: Chapter 2 introduces the neurophysiological foundation and the introduction of EEG, iEEG, tES, and DBS. Chapter 3 presents the mathematical models underlying the electric field simulations and discusses weak formulations for the two electrode models. Chapter 4 provides numerical background on FEM and its application to the CEM and PEM. Chapter 5 describes the implementation of the CEM in DUNEuro. Chapter 6 presents simulation results and the comparison of CEM with PEM in various scenarios. Finally, Chapters 7 and 8 are the discussion and the conclusion of this thesis.

Chapter 2

Neuroscientific Foundations

This work focuses on the simulation of electrical currents in the brain, an area located within the larger field of computational modeling in neuroscience and bioelectromagnetism. To lay the foundations for this research, it is helpful to understand the fundamental concepts and mechanisms of brain activity.
To motivate the mathematical modeling approaches that we apply in EEG, tES, iEEG, and DBS, we give an overview of relevant neurophysiological principles in the next following pages. The information given here is based on [18], [40], [27], and [4].

2.1 Neurophysiological Foundations

The human body consists of various organs, each with distinct functions and tasks. Among them, the brain is arguably the most complex, as it processes and regulates - together with the spinal cord - the information flow within the nervous system.

Neuron

Neurons are the units that process information. The brain contains at least 10^{10} neurons in the cerebral cortex, which forms the outermost layer of the brain and is $2-4$ mm thick and has an area of approximately 2500 cm^2.
A typical neuron has three main parts (see figure 2.1): The cell body (or soma) contains the nucleus and much of the metabolic machinery of the cell. The dendrites are thread-like extensions that receive signals from other neurons. The axon is a single fiber that carries the nerve impulses from the body of the cell to other neurons or target cells.
The dendrites and cell bodies are densely populated with thousands of synapses formed by connections with other neurons. These synapses are responsible for the information transfer between the dendrites and the cell bodies. Neurons actively process signals through more than 10^{14} interconnections or synapses. Synapses can be classified into excitatory synapses, which increase the membrane potential of the neuron and make it more likely to fire an action potential, and into inhibitory synapses, which decrease the membrane potential and make the neuron less likely to fire.

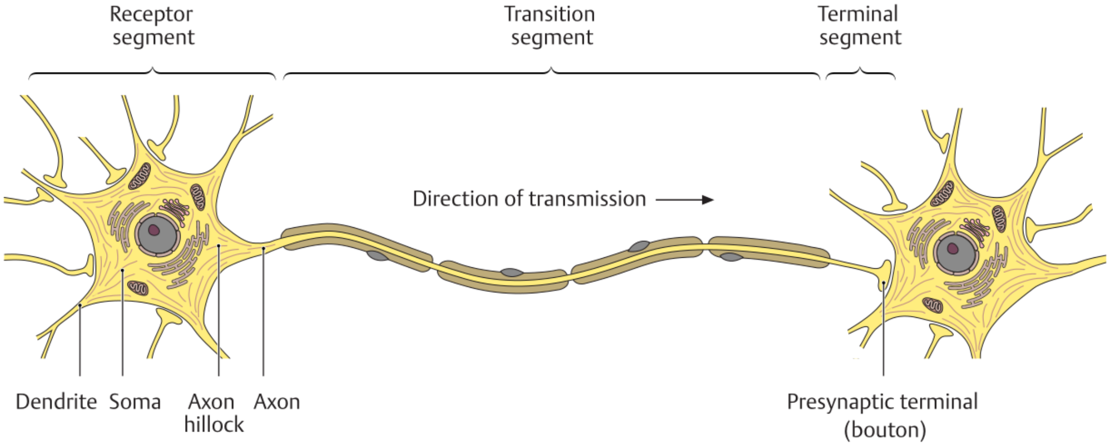

Figure 2.1: This is a schematic illustration of the fine structure of a neuron from [27].

Action Potential

Neurons are cells that are capable of transmitting electrical impulses, known as action potentials, to other neurons in the brain. The action potential begins in the axon hillock, where the signals from the neuron's dendrites converge. These dendrites are connected to other neurons through their axons, creating inputs that can generate a potential in the axon hillock. If this potential reaches a certain threshold, an action potential is triggered. So, an action potential is essentially a brief but powerful electrical signal that travels along the axon. Then it leads to the release of neurotransmitters at the axon terminals. This process is the foundation for the communication of neurons with each other.

The sum of many synchronized postsynaptic potentials generates current sources. These, in turn, produce electric potentials that are detectable by electrodes placed on or in the head by EEG and iEEG respectively.

Following [30], it is sufficient to model the current source as a mathematical dipole, because we only detect the macroscopic currents that result from microscopic neuronal activity. This abstraction captures the essential aspects for solving the forward and inverse problems in bioelectromagnetism.

Compartments

The anatomy affects how electrical events in neurons produce measurable current sources. The different tissues and compartments with their conductivities also influence the way the currents are conducted [57].

The neuronal tissue gets mainly subdivided into white matter and gray matter. The mapping of the tissue to white or gray matter is done via the data from magnetic-resonance imaging (MRI). White matter is tissue that is rich in axons. It is occupied by nerve fibers. Gray matter is tissue that is rich in cell bodies. In neuronal tissue, there are other structures, such as blood vessels and the ventricle system. The ventricle system is a system of spaces that are filled with cerebrospinal fluid (CSF), which is a clear liquor that serves as a buffer between the brain and the skull, and also has various regulating functions.

The brain can also be subdivided into regions that cover different tasks. Knowledge about the tasks of the different brain regions is helpful in inverse procedures.

2.2 EEG, iEEG, tES and DBS

Brain activity can be detected and measured in several ways. Some common methods are electroencephalography (EEG) and intracranial electroencephalography (iEEG). Common methods for modulating brain activity are transcranial electrical stimulation (tES) and deep brain stimulation (DBS).

EEG

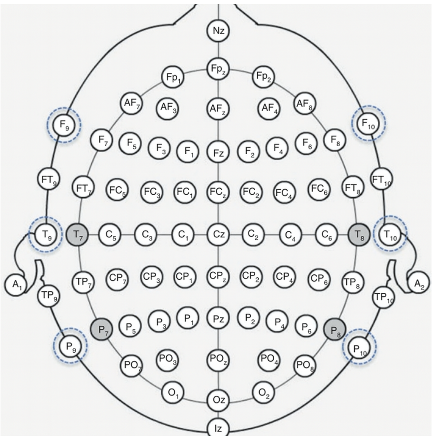

Figure 2.2: This figure shows the $10-10$ system and is from [28].

Electroencephalography (EEG) is a non-invasive method that measures the electrical activity of the brain by placing electrodes on the head. These electrodes detect voltage fluctuations caused by firing neurons, primarily those located in the cerebral cortex [4]. EEG is widely used in clinical settings and in research to understand cognitive functions, brain states, and neuronal mechanisms. It is also easier available and significantly cheaper than magnetoencephalography (MEG), because - among others - it does not require liquid helium for the superconducting magnets that exist in the MEG. EEG can be used in parallel with other methods such as MEG where it is proven to be beneficial [31] and tES [39]. There are standardized systems of electrode montages that are referred to as the $10-20$ and $10-10$ systems. These range from 21 electrodes for the $10-20$ system to more than 70 electrodes for the $10-10$ system [28], see figure 2.2. For EEG and also tES, a highly conducting gel is applied between the electrodes and the scalp.

tES

Not only is the non-invasive measurement and detection of electrical activity in the brain of importance but also to find ways to treat certain diseases non-surgically.

One way to do this is transcranial electrical stimulation (tES). This refers to a family of non-invasive techniques, including transcranial direct current stimulation (tDCS) (see [64]) and transcranial alternating current stimulation (tACS) (see [7]). tES can be used for both therapeutic and research purposes, with applications ranging from improving cognitive function and motor skills to treating neurological and psychiatric disorders [39][59][32]. It can be particularly helpful in the treatment of epilepsy [52].

In tES, a low-level electrical current is passed through the brain via electrodes placed on the scalp. This current can influence the excitability of the underlying neurons, either facilitating or inhibiting neuronal firing depending on the direction of the current flow.

The applied electric fields can modulate cortical activity and influence synaptic plasticity and neuronal synchronization [39].
A common montage to stimulate via tES is to use one anode and one cathode, which have an area of the interface of 25 - 35 cm^2 where the cathode is placed over the target [52]. In [25] a montage with 8 electrodes is discussed and the advantages investigated in [24]. The combination of EEG and tES is investigated in [39] and offers an approach to perform brain stimulation and monitoring simultaneously.

iEEG

While EEG measures the potentials at the scalp of the patient, in some cases this is not sufficient, i.e. extratemporal lobe epilepsy or non-lesional temporal lobe epilepsy (see [51]). The electric potential can then be measured by placing electrodes on the surface or the substance of the brain. This procedure is highly invasive, so this kind of EEG is called invasive electroencephalography or intracranial electroencephalography (iEEG) [65]. The electrodes used can be subdural grid electrodes and/or depth electrodes. In this thesis, we focus on the depth electrodes. The depth electrodes have $4-10$ contacts placed on a hollow plastic tube that can be inserted into the brain tissue itself. These depth electrodes are inserted through burr holes. In figure 2.3 the placement of such depth electrodes is shown. Since this method requires neurosurgical intervention, severe complications can appear, but the rates are low [51].

DBS

Deep brain stimulation (DBS) is an invasive method to stimulate and thus modulate neuronal activity. As in iEEG, the electrodes used for DBS can be different (see [65]), but in this thesis, we only consider the case of stereoelectroencephalography in which the depth electrodes are placed in the head of the patient. This plays an important role in localizing, for example, the epileptogenic zone in patients with epilepsy [65].
In DBS, low-intensity electrical pulses are applied to specific areas of the brain using depth electrodes. These pulses temporarily activate nearby nerve fibers close to the stimulating electrodes. The effects in regions that are not near each other depend on whether the stimulated neurons are excitatory or inhibitory. Like tES, DBS can improve symptoms of some conditions by changing the activity of brain networks [6].
DBS is a treatment that targets symptoms. It has to run continuously, typically 24 hours a day. For more information, we refer to [6].

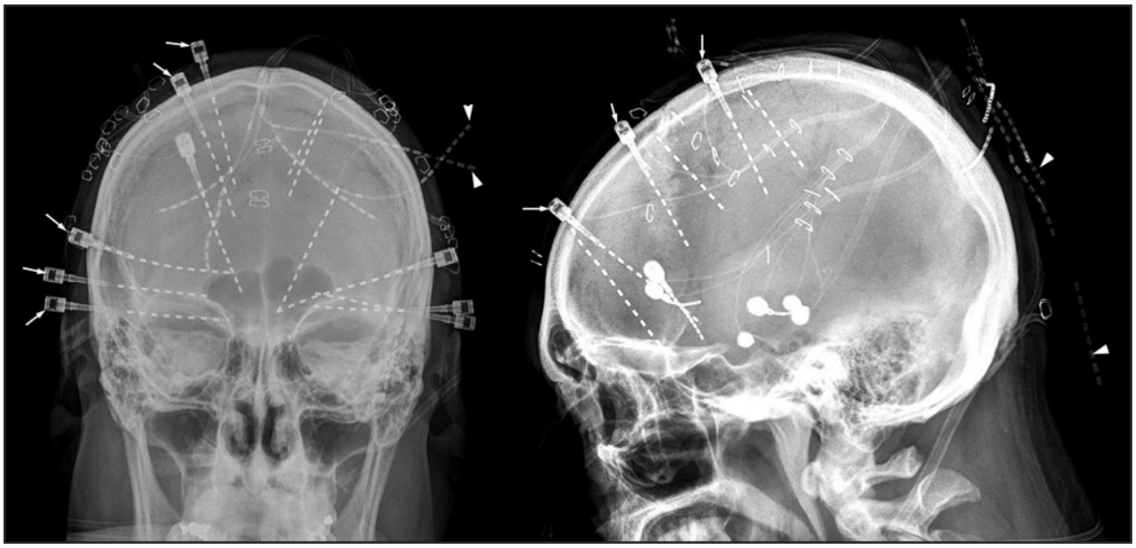

Figure 2.3: This figure shows an X-ray after implanting multiple depth electrodes. The depth electrodes that are secured with an anchor to minimize possible movements after the implantation are shown by the arrows point at the anchors. The figure is from [51].

Chapter 3

Mathematical Background

In this chapter, we will create the mathematical theory and the right frame for the models that we use and investigate.
We will start with the derivation of the main PDE that we will use to approximate the electric potential in the patients head and thus the measured potentials with the electrodes.

3.1 The Maxwell Equations

From a modeling point of view, the head can be understood as a volume conductor with different compartments and thus different conductivities in which electrical currents appear.
Neuronal activity is based on electric currents, which in turn generate electric and magnetic fields which can be measured on the outside of the head. The relationship between neuronal activity and its generated electric and magnetic fields is described by Maxwell's equations. The Maxwell equations are a system of four coupled differential equations which describe electric and magnetic fields, which we will use to derive the PDEs for the EEG and tES problem.
The four Maxwell equations are:

1. $\nabla \cdot \mathbf{E} = \frac{\rho}{\epsilon_0}$
2. $\nabla \cdot \mathbf{B} = 0$
3. $\nabla \times \mathbf{E} = -\frac{\partial \mathbf{B}}{\partial t}$
4. $\nabla \times \mathbf{B} = \mu_0(\mathbf{J} + \epsilon_0 \frac{\partial \mathbf{E}}{\partial t})$.

Here, $\mathbf{E}$ is the electric field, $\mathbf{B}$ the magnetic field, ρ the electric charge density, and $\mathbf{J}$ the current density. ϵ_0 is the vacuum permittivity and μ_0 the vacuum permeability.
For a more detailed description of the equations, see [16].

Quasistatic Approximation of Maxwell's Equations

An important and common simplification in the field of bioelectromagnetism is the quasistatic approximation of Maxwell's equations. We use the notion of being quasistatic in

the way it is used in bioelectromagnetism. The low-frequency assumption justifies this approximation, which says that in EEG and MEG measurements, the frequencies of interest (typically in the range of 0.1 Hz to several hundred Hz) are low compared to the speed of light. This means that the propagation of electromagnetic waves can be considered negligible over short distances and timescales. As a result, the time-varying electric and magnetic fields are slow enough so that changes in the fields can be approximated as quasi-static. The term $\mu_0\epsilon_0\frac{\partial \mathbf{E}}{\partial t}$ in the fourth equation represents the displacement current, which becomes significant at higher frequencies or in situations where the electric field changes rapidly. This can be fully understood in ([18], chapter III.A).
Thus, the system of equations that we work with is

1. $\nabla \cdot \mathbf{E} = \frac{\rho}{\epsilon_0}$
2. $\nabla \cdot \mathbf{B} = 0$
3. $\nabla \times \mathbf{E} = 0$
4. $\nabla \times \mathbf{B} = \mu_0 \mathbf{J}$.

From Quasistatic Maxwell's Equations to the PDE

Now, we will look at the fourth equation, which is

$$\nabla \times \mathbf{B} = \mu_0 \mathbf{J}$$

and divide it by the constant μ_0 on both sides and use the identity $\nabla \cdot (\nabla \times B) = 0$, which can be easily proven by a straight-forward calculation and get

$$0 = \nabla \cdot (\nabla \times B) = \nabla \cdot \mathbf{J}.$$

We denoted the current density by $\mathbf{J}$ and split the current density in a primary current $\mathbf{J}^p$, which is the neural activity and a return current $\sigma \mathbf{E}$ with $\sigma \in \mathbb{R}^{3\times 3}$ being the conductivity tensor. By the quasistatic equations, the electric field $\mathbf{E}$ can be represented as $\mathbf{E} = -\nabla u$ with u being the electric potential ([16], chapter 2).
The PDE that we will work with is

$$\nabla \cdot (\sigma \nabla u) = f \tag{3.1}$$

with $f = \nabla \cdot \mathbf{J}^p$. We have this PDE over a domain $\Omega \subset \mathbb{R}^3$ which is the volume conductor. The electrode models differ in their boundary conditions on $\partial\Omega$ that we will introduce in the next pages.

3.2 Electrode Models

The different electrode models differ in the boundary conditions that we additionally have for the PDE 3.1.
We denote the L electrodes by $e_1, ..., e_L$, the head domain by Ω and the boundary of the head by $\partial\Omega$. The electrode interface for the l-th electrode e_l is also denoted by e_l and the

area of the l-th electrode interface by $|e_l| \in \mathbb{R}$.
In the case of tES, a current is applied. The applied current with the l-th electrode is denoted by I_l. The sum of the applied current must be zero, $\sum_{l=1}^{L} I_l = 0$ - referred to as Kirchhoff's law - so that the total potential of the head does not increase with the stimulation. The sum of the injected current should not exceed a total of $8mA$, because of safety reasons (see [1]), so in sum, a positive charge of $+4mA$ and a corresponding negative charge of $-4mA$ are possible.

3.2.1 Point Electrode Model

The point electrode model (PEM) is very straightforward. The electrode gets approximated as a point on the boundary of the head. So, the measured potential by an electrode is the computed electric potential u at the corresponding point [19].
So, the PEM in the EEG forward problem has the assumption that no current is leaving the head on the boundary and is

$$\nabla \cdot (\sigma \nabla u) = f \qquad \text{in } \Omega \tag{3.2}$$

$$\sigma \frac{\partial u}{\partial n} = 0 \quad \text{on } \partial\Omega \tag{3.3}$$

with $f = \nabla \cdot \mathbf{J}^p$.
In the tES case, the right-hand side of the PDE is zero, because we do not model a source in the brain in this case and the stimulation is represented in the boundary condition by Dirac functions. If in this case the electrode positions are denoted by $p_1, ..., p_L$, the boundary condition is

$$\nabla \cdot (\sigma \nabla u) = 0 \qquad\qquad \text{in } \Omega \tag{3.4}$$

$$\sigma \frac{\partial u}{\partial n}(x) = \sum_{l=1}^{L} I_l \delta_{p_l} \quad \text{on } \partial\Omega, \tag{3.5}$$

see ([19], chapter 2.2). We point out that in the case of anisotropic σ the term $\frac{\partial u}{\partial n}$ is replaced by $\langle \sigma \nabla u, n \rangle$.

3.2.2 Complete Electrode Model

Together with the skin-electrode interface, the CEM incorporates the normal current distribution at this interface, because the attached electrodes to the head offer the current new paths to flow through the electrode instead of the skin compartment. This normal current distribution is called the shunting effect and thus describes the current that circulates on the contact surface, which affects the electric potential underneath the electrode [39]. This effect gets bigger when the contact impedances are low.

The CEM has the following boundary conditions for the PDE 3.2 which are

$$\sigma\frac{\partial u}{\partial n}(x) = 0 \qquad \forall x \in \partial\Omega \setminus \cup_{l=1}^{L} e_l \tag{3.6}$$

$$\int_{e_l} \sigma\frac{\partial u}{\partial n}(x)dS = I_l \qquad \forall l \in \{1, ..., L\} \tag{3.7}$$

$$(u + Z_l\sigma\frac{\partial u}{\partial n})|_{e_l} = U_l \qquad \forall l \in \{1, ..., L\}. \tag{3.8}$$

The first boundary condition (3.6) says that no current leaves the head except at the electrode interfaces. Equation (3.7) describes how the applied current I_l at the l-th electrode flows through the interface e_l. In the EEG forward problem, we have $I_l = 0$, $\forall l \in \{1, ..., L\}$. In the CEM, additionally, we have the effective contact impedances (ECI) Z_l for the l-th electrode respectively, which are the product of the measured average contact impedance (ACI) at the l-th electrode multiplied by the area $|e_l|$ of the l-th electrode interface. In applications, an attempt is made that the measured ACIs are below 5 kΩ for each electrode to have a conduction between the electrode and the scalp that is considered good enough. For this, a highly conductive gel is used between the electrode and the scalp [37]. The third condition (3.8) describes how the electrode potential U_l and the potential u beneath the electrode are connected and how the effective contact impedance Z_l plays a role. For anisotropic σ we again replace the term $\frac{\partial u}{\partial n}$ by $\langle \sigma\nabla u, n\rangle$. This was paid attention to in the implementation of the CEM.

When we integrate on both sides over the electrode interface, the third boundary condition in the EEG case ($I = 0$) becomes by using 3.7

$$\frac{\int_{e_l} u(x)\, dx}{|e_l|} = U_l, \tag{3.9}$$

so, in this case, U_l is the integral mean on the whole electrode interface of the potential u. In the tES case, we get for the same procedure

$$U_l = \frac{\int_{e_l} u\, dV + Z_l I_l}{|e_l|}.$$

So, the measured electrode potential is the mean of the potential under the electrode, plus the contribution of the product of the effective contact impedance and the injected current scaled by the electrode area, so $\frac{Z_l I_l}{|e_l|}$.

We take a look at the units: For the measured potentials, we have μV and for the conductivity tensor $\frac{S}{\text{mm}}$ and for ∇u the unit $\frac{\mu V}{\text{mm}}$, so naturally Z_l must have the unit Ωmm^2. The measured ACIs have the unit Ω. The ACI of the l-th electrode, ACI_{e_l}, is $\frac{Z_l}{|e_l|}$ and fulfills - by integrating and doing a straightforward calculation - the equation

$$\frac{\int_{e_l} U_l - u\, dS}{|e_l|} = ACI_{e_l} \cdot I_l.$$

3.3 The Reciprocal (Adjoint) Approach for the EEG Forward Problem

A very interesting and helpful principle in our field of bioelectromagnetism is the principle of reciprocity.

The principle of reciprocity links the act of measuring and stimulating and reverse the roles of sources and sensors. In the case of EEG for example, it says that having a dipole in the brain and measuring on the head surface is the adjoint problem to stimulating with electrodes on the head surface and measuring the electric potential in the brain at the position of the dipole. First, we give the general mathematical formulation of the adjoint problem and follow [55] and [61] for this.

The solution of the EEG forward problem with PEM is denoted by u:

$$\begin{aligned} \nabla \cdot (\sigma \nabla u) &= \nabla \cdot (M \cdot \delta_{x_0}) && \text{in } \Omega \\ \langle \sigma \nabla u, n \rangle &= 0 && \text{on } \partial\Omega \end{aligned}$$

and the solution of the tES problem with PEM and with the i-th and j-th electrode used for the stimulation is denoted by w:

$$\begin{aligned} \nabla \cdot (\sigma \nabla w) &= 0 && \text{in } \Omega \\ \langle \sigma \nabla w, n \rangle &= \delta_{e_i} - \delta_{e_j} && \text{on } \partial\Omega \end{aligned}$$

with δ_{e_i} denoting the Dirac delta distribution at the electrode position p_i of the electrode e_i.

The principle of reciprocity links the two solutions in the form:

$$\langle M, \nabla w(x_0) \rangle = u(p_i) - u(p_j).$$

for $x_0 \in \Omega$.

3.3.1 The EEG/tES Reciprocity for CEM

We will only show the proof for the principle of reciprocity for the CEM since the proof for the PEM can be easily derived from the proof for the CEM. The proof can also be found in [22].

In this case, we will specifically formulate the injection of the current through the normal derivatives at the electrode interface and the Kronecker delta function, which is denoted by $\widetilde{\delta}_{ij}$ for indices i and j, representing the applied current, distinguishing it from the Dirac distribution δ. Here, we use the notation $\langle \nabla -, n \rangle$ for the normal derivative.

The solution of the EEG forward problem is denoted by u

$$\begin{aligned} \nabla \cdot (\sigma \nabla u) &= \nabla \cdot (M \cdot \delta_{x_0}) && \text{on } \Omega \\ \langle \sigma \nabla u, n \rangle &= 0 && \text{on } \partial\Omega \setminus \cup_{l=1}^{L} e_l \\ \int_{e_l} \langle \sigma \nabla u, n \rangle dS &= 0 && \forall l \in \{1, ..., L\} \\ (u + Z_l \langle \sigma \nabla u, n \rangle)|_{e_l} &= U_l && \text{on } e_l \end{aligned}$$

and the solution of the tES problem with the i-th and j-th electrode used for the stimulation is denoted by w:

$$\begin{array}{lcll} \nabla\cdot(\sigma\nabla w) & = & 0 & \text{on } \Omega \\ \langle\sigma\nabla w, n\rangle & = & 0 & \text{on } \partial\Omega \setminus \cup_{l=1}^{L} e_l \\ \int_{e_l}\langle\sigma\nabla w, n\rangle dS & = & \widetilde{\delta}_{il} - \widetilde{\delta}_{jl} & \forall l \in \{1,...,L\} \\ (w + Z_l\langle\sigma\nabla w, n\rangle)|_{e_l} & = & W_l & \text{on } e_l. \end{array}$$

We want to show the reciprocity for the CEM, which is

$$\langle M, \nabla w(x_0)\rangle = U_i - U_j.$$

In the following calculations, we use for functions a and b several times

$$\int_\Omega (\nabla\cdot a)\cdot b\, dV = \int_{\partial\Omega}\langle a, n\rangle \cdot b\, dS - \int_\Omega \langle a, \nabla b\rangle\, dV. \tag{3.10}$$

We start with

$$\langle M, \nabla w(x_0)\rangle = \langle M, \int_\Omega \delta_{x_0}\cdot\nabla w\, dV\rangle = \int_\Omega \langle M, \delta_{x_0}\cdot\nabla w\rangle\, dV = \int_\Omega \langle M\cdot\delta_{x_0}, \nabla w\rangle\, dV$$

and use (3.10):

$$\int_\Omega \langle M\cdot\delta_{x_0}, \nabla w\rangle\, dV = \int_{\partial\Omega} w\langle M\delta_{x_0}, n\rangle dS - \int_\Omega \nabla\cdot(M\delta_{x_0})\cdot w\, dV$$

the summand $\int_{\partial\Omega} w\langle M\delta_{x_0}, n\rangle dS$ equals zero, because δ_{x_0} is zero on the boundary of the head, so

$$\underbrace{\int_{\partial\Omega} w\langle M\delta_{x_0}, n\rangle dS}_{=0} - \int_\Omega \nabla\cdot(M\delta_{x_0})\cdot w\, dV = -\int_\Omega \nabla\cdot(M\delta_{x_0})\cdot w\, dV$$

and this equals with the first equation of the PDE

$$-\int_\Omega \nabla\cdot(M\delta_{x_0})\cdot w\, dV = -\int_\Omega \nabla\cdot(\sigma\nabla u) w\, dV.$$

Using (3.10) again and the symmetry of σ, we get

$$-\int_\Omega \nabla\cdot(\sigma\nabla u) w\, dV = -\int_{\partial\Omega} w\langle\sigma\nabla u, n\rangle dS + \underbrace{\int_\Omega \langle\nabla w, \sigma\nabla u\rangle\, dV}_{=\int_\Omega \langle\sigma\nabla w, \nabla u\rangle\, dV}$$

Again, with (3.10), the right-hand side equals

$$-\int_{\partial\Omega} w\langle\sigma\nabla u, n\rangle dS + \int_{\partial\Omega} u\langle\sigma\nabla w, n\rangle\, dS - \underbrace{\int_\Omega u\, \underbrace{(\nabla\cdot\sigma\nabla w)}_{=0}}_{=0}$$

Due to the boundary condition, which says that there is no outflow outside of the electrode interfaces, we can just consider the boundary of the head $\partial\Omega$ which belongs to an electrode interface e_l:

$$\int_{\partial\Omega} u\langle\sigma\nabla w, n\rangle\, dS - \int_{\partial\Omega} w\langle\sigma\nabla u, n\rangle dS = \sum_{l=1}^{L}(\int_{e_l} u\langle\sigma\nabla w, n\rangle\, dS - \int_{e_l} w\langle\sigma\nabla u, n\rangle dS).$$

We take a closer look at the first integral and add a zero:

$$\int_{e_l} u\langle\sigma\nabla w, n\rangle\, dS = \int_{e_l} (u - U_l)\langle\sigma\nabla w, n\rangle\, dS + \widetilde{\delta}_{il}\int_{e_l} U_l\langle\sigma\nabla w, n\rangle\, dS + \widetilde{\delta}_{jl}\int_{e_l} U_l\langle\sigma\nabla w, n\rangle\, dS,$$

and also

$$\int_{e_l} w\langle\sigma\nabla u, n\rangle dS = \int_{e_l} (w - W_l)\langle\sigma\nabla u, n\rangle\, dS.$$

Together with the third boundary condition we get

$$(u - U_l)\langle\sigma\nabla w, n\rangle = -Z_l\langle\sigma\nabla u, n\rangle\langle\sigma\nabla w, n\rangle$$

and

$$(w - W_l)\langle\sigma\nabla u, n\rangle = -Z_l\langle\sigma\nabla w, n\rangle\langle\sigma\nabla u, n\rangle$$

and this gives us

$$\langle M, \nabla w(x_0)\rangle = U_i\int_{e_i}\langle\sigma\nabla w, n\rangle\, dS + U_j\int_{e_j}\langle\sigma\nabla w, n\rangle\, dS.$$

The first integral equals 1 and the second integral equals -1, so in total we have

$$\langle M, \nabla w(x_0)\rangle = U_i - U_j.$$

So we have shown that the principle of reciprocity also exists for the CEM. This gives us benefits in the numerical implementation that will be seen in chapter 4.5.

Convergence of CEM to PEM

There are different ways to show that the CEM converges for the radius r going to zero. A simple way is to show it by additionally assuming $Z_l \to \infty$ for all $l \in \{1, ..., L\}$:
From 3.8 we get

$$\sigma\frac{\partial u}{\partial n}(x) = \frac{1}{Z_l}(U_l - u) \qquad \text{on } e_l, \quad \forall l \in \{1, ..., L\}. \tag{3.11}$$

With $Z_l \to \infty$, we have

$$\sigma\frac{\partial u}{\partial n}(x) = 0 \quad \text{on } e_l \tag{3.12}$$

for all electrodes and thus for the entire boundary $\partial\Omega$ of the domain which leads us to the boundary condition of the PEM, 3.3.

Intuitively, we can see this by interpreting the limit of the impedances Z_l as the electrodes not effecting the current flux underneath them in any way, which is the case for the PEM.

There is also an argument for the convergence which does not require the impedances going to infinity in the analytical setting, but leaving them fixed, using the main result of [19] and the principle of reciprocity for CEM and PEM. This argument is shown in the Appendix A.1.
The convergence is also shown in the numerical setting in chapter 4.6 and in a simulation in chapter 6.2.2.

3.4 Weak Formulation of PDEs

Now that we know the mathematical foundations of our studies, we look at methods and tools to approximate solutions for the PDE 3.2 with different boundary conditions of the electrode models.
PDEs can be, in general, very difficult or impossible to solve analytically. There exist even PDEs where a classical solution does not exist under certain regularity assumptions. Such an example is the shock wave equation ([10], chapter 3.4, example 1).
We can weaken these assumptions and work in the framework of weak solutions.
The classical approach requires that the function u is sufficiently smooth, so in this case it is at least twice differentiable to have well-defined terms in the PDE and boundary condition. However, in modeling of real-world phenomena often situations where the solution is not sufficiently smooth are involved, or where the domain is more complicated, leading to difficulties in the classical treatment. In our case, the conductivity jumps between the compartments are represented in σ, which leads to a non-smooth electric potential u. In such cases, we use the weak formulation, which relaxes the pointwise requirements for the regularity and focuses on integral forms of the PDE.
The weak formulation is the foundation for the finite element methods (FEM) which we will investigate in detail in chapter 4.
The weak formulation is achieved by multiplying the classical PDE by test functions v from a suitable space and integrating over the domain Ω. This process involves the application of integration by parts to reduce the order of differentiation, which allows - for our particular PDE 3.2 - solutions with lower regularity.

For this setting, we need the notion of Sobolev spaces and weak derivatives. We expect the reader to know the basics of functional analysis, including the notion of a Banach space, a Hilbert space, a norm, and a Lebesgue space $L^2(\Omega)$ with its corresponding norm and properties. This can be learned and seen in [3], [41] and [2].

Weak Derivatives

In the Lebesgue space $L^2(\Omega)$ the elements are not defined in a pointwise sense. So, it makes sense to introduce a notion of a derivative, which also depends on the global behavior and does not depend on the pointwise values. First, we need the multi-index notation for partial derivatives, which takes a n-tuple $\alpha \in \mathbb{N}_0^n$ of non-negative integers $\alpha_i \in \mathbb{N}_0$. Here,

$\mathbb{N}_0$ denotes the set of non-negative integers. We define

$$|\alpha| := \sum_{i=1}^{n} \alpha_i.$$

Let $C^\infty(\Omega)$ denote the space of smooth functions on Ω. For $\Phi \in C^\infty$ we denote by $\partial^\alpha \Phi$ the function $(\frac{\partial}{\partial x_1})^{\alpha_1} \cdots (\frac{\partial}{\partial x_n})^{\alpha_n} \Phi$. For a vector x, we define $x^\alpha := x_1^{\alpha_1} \cdots x_n^{\alpha_n}$.
The support of a function $f \colon X \to Y$ is the closure of the set $\{x \in X | u(x) \neq 0\}$. If the support is a compact set and is a subset of the interior of X, then we say that f has a compact support. In the case of a bounded set Ω, a function with compact support vanishes in a neighborhood of the boundary $\partial\Omega$.

Definition 1. Let $\Omega \subset \mathbb{R}^n$. $C_0^\infty(\Omega) \subset C^\infty(\Omega)$ is defined to be the subset of smooth functions with compact support in Ω.

We now get to the definition of weak derivatives, which will play a role in our theory.

Definition 2. Let $\Omega \subset \mathbb{R}^n$ and $u \in L^1_{\text{loc}}(\Omega)$ be in the space of locally integrable functions $L^1_{\text{loc}}(\Omega)$. We call a function $v \in L^1_{\text{loc}}(\Omega)$ the weak derivative of u to the multi-index α and denote it by $v = \partial^\alpha u$ if

$$\int_\Omega \varphi \cdot v \, dV = (-1)^{|\alpha|} \int_\Omega \partial^\alpha \varphi \cdot u \, dV \quad \text{for all } \varphi \in C_0^\infty(\Omega).$$

Since we multiply $\varphi \in C_0^\infty(\Omega)$ which vanish on the boundary, this equation can be brought back to partial integration where v replaces the derivative. It can also be easily seen that in the case where the (classical) derivative exists and is continuous, the classical derivative and the weak derivative coincide.
A simple example of a weak derivative is $f' \colon \mathbb{R} \to \mathbb{R}$ with $f'(x) = -1$ for $x < 0$ and $f'(x) = 1$ for $x > 0$ of the function f, which maps a real number to its absolute value. We see that f is continuous everywhere, but not differentiable at $x = 0$. Nevertheless, it has a weak derivative, even though the classical derivative does not exist at the point $x = 0$.

Sobolev Spaces

In the frame of weak derivatives the solutions are most commonly in a - so called - Sobolev space. For this, let $\Omega \subset \mathbb{R}^n$ be an open subset. The Sobolev space $H^k(\Omega)$ is defined as the set of functions $u \in L^2(\Omega)$ whose weak derivatives up to order k exist and also belong to $L^2(\Omega)$. Formally,

$$H^k(\Omega) = \left\{ u \in L^2(\Omega) : \partial^\alpha u \in L^2(\Omega), \forall \alpha \in \mathbb{N}_0^L \text{ with } |\alpha| \leq k \right\}.$$

The space $H^k(\Omega)$ is equipped with the norm

$$\|u\|_{H^k(\Omega)} = \left(\sum_{|\alpha| \leq k} \|D^\alpha u\|^2_{L^2(\Omega)} \right)^{1/2},$$

so weak derivatives are incorporated in this norm.
The Sobolev spaces $H^k(\Omega)$ are Banach spaces and together with the inner product

$$(u,v)_{H^k(\Omega)} = \sum_{|\alpha|\leq k} \int_\Omega D^\alpha u \cdot D^\alpha v \, dx,$$

they are also Hilbert spaces.
An important special case is $H^1(\Omega)$, where we will neglect the 1 in the subsequent chapters and simply write $H(\Omega)$. The space $H(\Omega)$ consists of functions $u \in L^2(\Omega)$ whose first-order weak derivatives also belong to $L^2(\Omega)$. Its norm is given by

$$\|u\|_{H(\Omega)} = \left(\|u\|^2_{L^2(\Omega)} + \|\nabla u\|^2_{L^2(\Omega)}\right)^{1/2}.$$

Now that we have our mathematical setting, we will introduce the weak formulation of PDEs specifically with our PDE 3.2 and the two different sets of boundary conditions for our different electrode models.

3.4.1 Weak Formulation with PEM

We are looking for a $u \in H(\Omega)$ that fulfills the initial PDE (3.2)-(3.3) in a weak sense, so we first multiply both sides with a test function $\varphi \in H(\Omega)$ and integrate over our domain Ω:

$$\textstyle\int_\Omega \nabla \cdot (\sigma\nabla)\varphi \, dV \quad = \quad \int_\Omega (\nabla \cdot J^p)\varphi \, dV.$$

We will use Gauss's divergence theorem on the left-hand side first:

$$\textstyle\int_\Omega \nabla \cdot (\sigma\nabla)\varphi \, dV \quad = \quad -\int_\Omega \sigma\nabla u \cdot \nabla\varphi \, dV + \int_{\partial\Omega} \sigma \frac{\partial u}{\partial n}\varphi \, dS.$$

If we are not stimulating, we have $\sigma\frac{\partial u}{\partial n} = 0$ on $\partial\Omega$, so the weak formulation for the EEG forward problem is to find a $u \in H^1(\Omega)$, such that

$$\textstyle\int_\Omega \sigma\nabla u \cdot \nabla\varphi \, dV \quad = \quad -\int_\Omega (\nabla \cdot J^p)\varphi \, dV, \qquad \forall\varphi \in H(\Omega).$$

In the tES case, we have $\sigma\frac{\partial u}{\partial n}(x) = \sum\limits_{l=1}^{L} I_l \delta_{e_l}$ on $\partial\Omega$, so the boundary integral is

$$\int_{\partial\Omega} \sigma\frac{\partial u}{\partial n}\varphi \, dS = \int_{\partial\Omega} \sum_{l=1}^{L} I_l\delta_{e_l}\varphi \, dS = \sum_{l=1}^{L} I_l \int_{\partial\Omega} \delta_{e_l}\varphi \, dS = \sum_{l=1}^{L} I_l\varphi(p_l),$$

where p_l denotes again the position of the l-th electrode. Therefore, the weak formulation for the tES case is

$$\int_\Omega \sigma\nabla u \cdot \nabla\varphi \, dV = \sum_{l=1}^{L} I_l\varphi(p_l). \tag{3.13}$$

If we are putting the tES and EEG forward problem together, we get

$$\int_\Omega \sigma \nabla u \cdot \nabla \varphi \, dV = \sum_{l=1}^{L} I_l \varphi(p_l) - \int_\Omega (\nabla \cdot J^p)\varphi \, dV, \quad \forall \varphi \in H(\Omega). \tag{3.14}$$

In total, we get the bilinear and linear form with the elements $u, \varphi \in H(\Omega)$

$$a^{\text{PEM}}(u, \varphi) = \int_\Omega \sigma \nabla u \cdot \nabla \varphi \, dV$$

and

$$l^{\text{PEM}}(\varphi) = \sum_{l=1}^{L} I_l \varphi(p_l) - \int_\Omega (\nabla \cdot J^p)\varphi \, dV.$$

We call $u \in H(\Omega)$ a weak solution of our PDE 3.2-3.3 if it fulfills

$$a^{\text{PEM}}(u, \varphi) = l^{\text{PEM}}(\varphi) \tag{3.15}$$

for all $\varphi \in H(\Omega)$. We note that strictly speaking, the linear form l^{PEM} is not well-defined on $H(\Omega)$ due to the point evaluations $\varphi(p_l)$. To derive the weak formulation for PEM mathematically more rigorously, a setting is required like it is presented in ([12], problem 7).

3.4.2 Weak Formulation of CEM

We do the same for the CEM. We first multiply a $\varphi \in H(\Omega)$ and then integrate over Ω and again get

$$\textstyle\int_\Omega \nabla \cdot (\sigma \nabla)\varphi \, dV \quad = \quad \int_\Omega (\nabla \cdot J^p)\varphi \, dV.$$

The left-hand side is

$$\textstyle\int_\Omega \nabla \cdot (\sigma \nabla)\varphi \, dV \quad = \quad -\int_\Omega \sigma \nabla u \cdot \nabla \varphi \, dV + \int_{\partial\Omega} \sigma \frac{\partial u}{\partial n} \varphi \, dS. \ .$$

The third boundary condition of the CEM 3.8 gives us

$$\sigma \frac{\partial u}{\partial n}(x) = \frac{1}{Z_l}(U_l - u(x)) \quad \forall x \in e_l.$$

Using this for the boundary integral and for all electrodes, we get with the zero outflow at the boundary that does not belong to an electrode interface that

$$\sum_{l=1}^{L} \int_{e_l} \frac{1}{Z_l}(U_l - u)\varphi \, dS - \int_\Omega \sigma \nabla u \cdot \nabla \varphi \, dV = \int_\Omega (\nabla \cdot J^p)\varphi \, dV. \tag{3.16}$$

We rearrange the two boundary conditions (3.7), (3.8) and get

$$Z_l I_l = \int_{e_l} Z_l \sigma \frac{\partial u}{\partial n} \, dS = \int_{e_l} (U_l - u) \, dS$$

and thus

$$\frac{1}{Z_l}\int_{e_l}(U_l - u)\,dS = I_l, \quad \forall l \in \{1, ..., L\}. \tag{3.17}$$

The left-hand side of 3.16 itself is not a coercive bilinear form. So, we take an arbitrary $\Phi \in \mathbb{R}^L$ with entries $\Phi_l \in \mathbb{R}$ for $l \in \{1, ..., L\}$. Then it holds - after multiplying with -1 on both sides - that

$$\sum_{l=1}^{L}\int_{e_l}\frac{1}{Z_l}(U_l - u)(\Phi_l - \varphi)\,dS + \int_\Omega \sigma\nabla u\cdot\nabla\varphi\,dV$$

$$= \sum_{l=1}^{L}\underbrace{\int_{e_l}\frac{1}{Z_l}(U_l - u)\Phi_l\,dS}_{\overset{3.17}{=}I_l\Phi_l} - \underbrace{(\sum_{l=1}^{L}\int_{e_l}\frac{1}{Z_l}(U_l - u)\varphi\,dS - \int_\Omega \sigma\nabla u\cdot\nabla\varphi\,dV)}_{=\int_\Omega(\nabla\cdot J^p)\varphi\,dV},$$

so we get in total

$$\sum_{l=1}^{L}\int_{e_l}\frac{1}{Z_l}(U_l - u)(\Phi_l - \varphi)\,dS + \int_\Omega \sigma\nabla u\cdot\nabla\varphi\,dV$$

$$= \sum_{l=1}^{L} I_l\Phi_l - \int_\Omega(\nabla\cdot J^p)\varphi\,dV.$$

This is the weak formulation with which we will mainly work. The test and trial space are generally $H(\Omega)\oplus\mathbb{R}^L$ while $H(\Omega)$ captures the nodes of the mesh and $\mathbb{R}^L$ the measured potentials with the L electrodes. So, we get the bilinear and linear form with the elements $(u, U), (\varphi, \Phi) \in H(\Omega)\oplus\mathbb{R}^L$ and

$$a^{\text{CEM}}((u, U), (\varphi, \Phi)) = \sum_{l=1}^{L}\int_{e_l}\frac{1}{Z_l}(U_l - u)(\Phi_l - \varphi)\,dS + \int_\Omega \sigma\nabla u\cdot\nabla\varphi\,dV$$

and

$$l^{\text{CEM}}((\varphi, \Phi)) = \sum_{l=1}^{L} I_l\Phi_l - \int_\Omega(\nabla\cdot J^p)\varphi\,dV.$$

We call $(u, U) \in H(\Omega)\oplus\mathbb{R}^L$ a weak solution of the PDE 3.2 with the CEM boundary conditions 3.6-3.8 if it fulfills

$$a^{\text{CEM}}((u, U), (\varphi, \Phi)) = l^{\text{CEM}}((\varphi, \Phi)) \tag{3.18}$$

for all $(\varphi, \Phi) \in H(\Omega)\oplus\mathbb{R}^L$.

Uniqueness and Existence of a Weak Solution

For the uniqueness and existence of weak solutions of elliptic PDEs, the Lax-Milgram theorem is a common tool to show this (see [10], chapter 6.2.1). We can see in ([53], chapter 3) and ([12], chapter 1.3.2.) that for the uniqueness of the solution for PEM, the Sobolev space $H(\Omega)$ gets restricted to

$$H_*(\Omega) = \{u \in H(\Omega) : \int\limits_{\Omega} u \, dV = 0\}$$

and for CEM $H(\Omega) \oplus \mathbb{R}^L$ gets restricted to

$$(H(\Omega) \oplus \mathbb{R}^L)_* = \{(u, U) \in H(\Omega) \oplus \mathbb{R}^L : \int\limits_{\Omega} u \, dV = -\sum_{l=1}^{L} U_l\}$$

since these are isometrically isomorphic to the quotient spaces $H(\Omega)/\mathbb{R} \cdot 1$ and $H(\Omega) \oplus \mathbb{R}^L/\mathbb{R} \cdot (1, 1)$, respectively.

3.5 Source Model

Modeling in neuroscience also has to include modeling the electric current sources in the brain. There are different ways of doing this. The source is captured in the right-hand side of the PDE 3.2. In the approach that we will use for these simulations, the source is modeled as a current dipole with moment M, $f(x) = \nabla \cdot (M \delta_{x_0}(x)) = \nabla \cdot (M \delta(x_0 - x))$ with δ being the Dirac distribution. Approaches such as the multipolar Venant approach [58] and the $H(div)$ approach [29] embed the singularity by substituting the point dipole with an object which is dipole-like and shows more regularity. On the other hand, subtraction approaches handle the dipole analytically by taking the singularity out of the formulation. After dealing with the achieved regular problem, in subtraction approaches we add the singularity back in [63],[8],[20].

In this work, we will focus on the local subtraction source model, due to its rigorous mathematical foundation and its high numerical accuracy [20].

This method is based on the classical subtraction approach that was already investigated in [63]. Compared to the classical subtraction approach, the local subtraction approach uses only the analytical solution for a small patch $\Omega^\infty \subset \Omega$ around the dipole at a position x_0. This leads to a sparse right-hand side vector in the FEM formulation and thus good computation times. We start straight with the local subtraction approach with the classical boundary condition of PEM 3.3 and then derive a local subtraction approach for the CEM using its boundary conditions.

3.5.1 Local Subtraction Approach for PEM

In source analysis, the forward problem has to be calculated for sources of the order of $\geq 10^4$. So, assembling the right-hand sides for the classical subtraction approach takes too much time since the right-hand sides are dense in this case.

Instead of formulating the problem in the weak sense over the entire domain including the source, we subtract a suitable function u^{∞} from the potential u and derive a weak formulation for $u^{\text{corr}} = u - u^{\infty}$ [20].
We first assume that the conductivity tensor σ is constant in a neighborhood of our source position $x_0 \in \mathbb{R}^3$. Denote this conductivity tensor by $\sigma^{\infty} \in \mathbb{R}^{3\times 3}$.
In the subtraction approach, we look at the equation

$$\nabla \cdot (\sigma^{\infty} \nabla u^{\infty}) = \nabla \cdot (M \cdot \delta_{x_0}) \quad \text{on } \mathbb{R}^3,$$

which is PDE in an unbounded homogeneous conductor. Here, we work with an existing analytical solution for u^{∞} in the isotropic case, which is (see [46])

$$u^{\infty}(x) = \frac{1}{4\pi\sigma^{\infty}} \frac{\langle M, x - x_0 \rangle}{|x - x_0|^3}.$$

We will have a look at the resulting PDE for the correction potential u^{corr}:
We have $\sigma^{\text{corr}} := \sigma^{\infty} - \sigma$, $u = u^{\text{corr}} + u^{\infty}$ and $\nabla \cdot (\sigma^{\infty} \nabla u^{\infty}) = \nabla \cdot (M \cdot \delta_{x_0})$ and thus derive for 3.2 and 3.3

$$\begin{aligned} \nabla \cdot (\sigma \nabla u) &= \nabla \cdot (\sigma \nabla u^{\text{corr}}) + \nabla \cdot (\sigma^{\text{corr}} \nabla u^{\infty}) + \nabla \cdot (\sigma^{\infty} \nabla u^{\infty}) \\ &= \nabla \cdot (\sigma \nabla u^{\text{corr}}) + \nabla \cdot (\sigma^{\text{corr}} \nabla u^{\infty}) + \nabla \cdot (M \cdot \delta_{x_0}). \end{aligned} \tag{3.19}$$

If we subtract the equation $\nabla \cdot (\sigma \nabla u) = \nabla \cdot (M \cdot \delta_{x_0})$ from 3.19, the initial PDE becomes

$$\begin{aligned} \nabla \cdot (\sigma \nabla u^{\text{corr}}) &= -\nabla \cdot (\sigma^{\text{corr}} \nabla u^{\infty}) \quad \text{in } \Omega, \\ \sigma \frac{\partial u^{\text{corr}}}{\partial n} &= -\sigma \frac{\partial u^{\infty}}{\partial n} \quad \text{on } \partial\Omega. \end{aligned}$$

We can see that the right-hand side of the PDE for the correction potential u^{corr} contains u^{∞}. In this moment, the right-hand side will be non-zero for a large part of the domain which leads to a bigger effort for the assembly of the right-hand side.
In the local subtraction approach, we work with a $\chi \colon \Omega \to \mathbb{R}$ that is 1 in a neighborhood of the source position. We call this neighborhood the patch and denote it by $\Omega^{\infty} \subset \Omega$.
In the case of a continuous Galerkin method (see [33], chapter 1.2), where the computed potential is required to be a continuous function, which we will use in this thesis, some additional regularity is required for χ. We need χ to be continuous and to be contained in the space $H(\Omega)$. We achieve this by not only having a patch Ω^{∞}, but also having a transition region $\tilde{\Omega}$ where χ goes continuously from 1 to 0. We can see this in figure 3.1. We have that $\Omega^{\infty} \cap \tilde{\Omega} = \emptyset$. For the local subtraction approach, we define the correction potential as

$$u^{\text{corr}} := u - \chi \cdot u^{\infty}. \tag{3.20}$$

It is important to note that the conductivity σ is not assumed to be constant in Ω^{∞}, but that Ω^{∞} contains a neighborhood of x_0 where the conductivity is constant, so the patch can also include tissue compartments that have different conductivities and even the patch

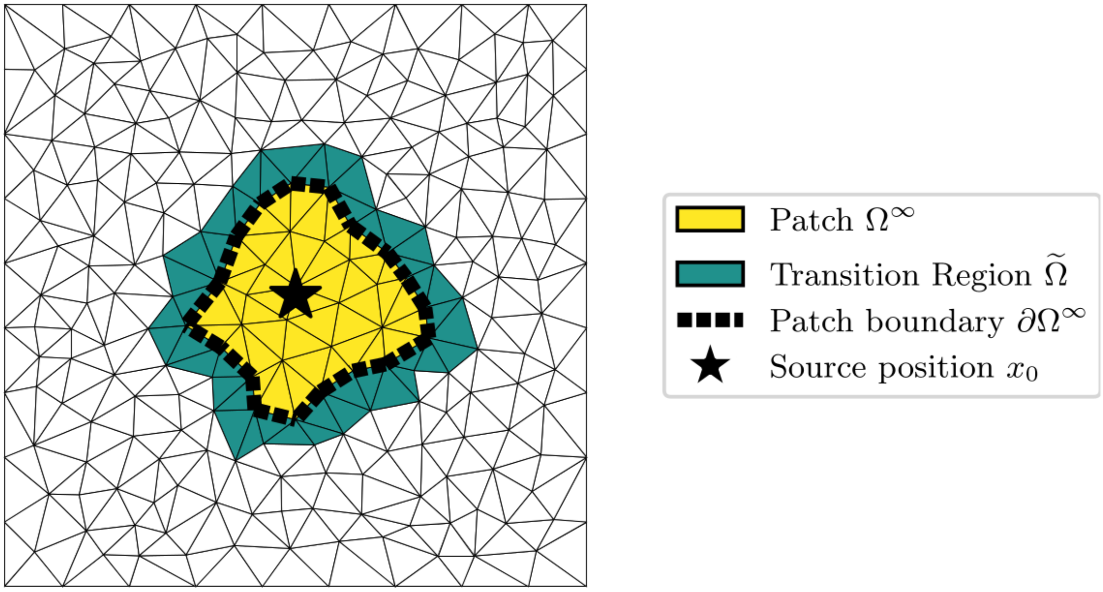

Figure 3.1: This figure shows a two dimensional visualization of the patch Ω^∞ and the transition region $\widetilde{\Omega}$ of a source at the position x_0. The function χ is 1 in the yellow colored patch and transitions continuously to 0 in the green colored transition region $\widetilde{\Omega}$. This figure is from [20].

is allowed to touch the boundary of the domain Ω.
Now, similar to the common subtraction approach we calculate with $\sigma^{\text{corr}} := \sigma - \sigma^\infty$, $u = u^{\text{corr}} + \chi \cdot u^\infty$ and $\nabla \cdot (\sigma^\infty \nabla u^\infty) = \nabla \cdot (M \cdot \delta_{x_0})$ and get

$$\nabla \cdot (\sigma \nabla u) = \nabla \cdot (\sigma \nabla u^{\text{corr}}) + \nabla \cdot (\sigma^{\text{corr}} \nabla \chi u^\infty) + \nabla \cdot (\sigma^\infty \nabla \chi u^\infty)$$

$$= \nabla \cdot (\sigma \nabla u^{\text{corr}}) + \nabla \cdot (\sigma^{\text{corr}} \nabla \chi u_\infty) + \nabla \cdot (\sigma^\infty \nabla (\chi - 1) u^\infty) + \nabla \cdot (M \cdot \delta_{x_0}).$$

So, the initial PDE becomes

$$\begin{aligned} \nabla \cdot (\sigma \nabla u^{\text{corr}}) &= -\nabla \cdot (\sigma^{\text{corr}} \nabla \chi u^\infty) - \nabla \cdot (\sigma^\infty \nabla (\chi - 1) u^\infty) \quad \text{in } \Omega, \\ \sigma \frac{\partial u^{\text{corr}}}{\partial n} &= -\sigma \frac{\partial (\chi u^\infty)}{\partial n} \quad \text{on } \partial\Omega. \end{aligned}$$

In the patch, we naturally have $\sigma^{\text{corr}} = 0$ and $\chi - 1 = 0$ since χ is constant 1 in the patch. So, there is no singularity in the formulation of the problem anymore. It is possible to integrate after multiplying a test function φ to the left-hand side. With the boundary condition, we get

$$\begin{aligned} \int_\Omega (\nabla \cdot (\sigma \nabla u^{\text{corr}})) \varphi \, dV &= \int_{\partial\Omega} \sigma \frac{\partial u^{\text{corr}}}{\partial n} \varphi \, dS - \int_\Omega \sigma \nabla u^{\text{corr}} \cdot \nabla \varphi \, dV \\ &= -\int_{\partial\Omega} \sigma \frac{\partial (\chi u^\infty)}{\partial n} \varphi \, dS - \int_\Omega \sigma \nabla u^{\text{corr}} \cdot \nabla \varphi \, dV. \end{aligned}$$

We continue with the right-hand side and multiply a test function φ and then do partial integration:

$$\begin{aligned}\int_\Omega \big(-\nabla \cdot (\sigma^{\text{corr}} \nabla(\chi u^\infty))\varphi - \nabla \cdot (\sigma^\infty \nabla((\chi - 1)u^\infty))\varphi \big)\, dV \\ = -\int_{\partial\Omega} \sigma^{\text{corr}} \frac{\partial(\chi u^\infty)}{\partial n} \varphi \, dS - \int_{\partial\Omega} \sigma^\infty \frac{\partial((\chi-1)u^\infty)}{\partial n} \varphi \, dS \\ + \int_\Omega \sigma^{\text{corr}} \nabla(\chi u^\infty) \cdot \nabla\varphi \, dV + \int_\Omega \sigma^\infty \nabla((\chi-1)u^\infty) \cdot \nabla\varphi \, dV.\end{aligned}$$

and with $\chi = 1$ on Ω^∞, we get

$$\begin{aligned}\text{r.h.s.} = -\int_{\partial\Omega} \sigma \frac{\partial(\chi u^\infty)}{\partial n} \varphi \, dS + \int_{\partial\Omega} \sigma^\infty \frac{\partial u^\infty}{\partial n} \varphi \, dS \\ + \int_{\Omega^\infty} \sigma^{\text{corr}} \nabla u^\infty \cdot \nabla\varphi \, dV + \int_{\Omega\setminus\Omega^\infty} \sigma \nabla(\chi u^\infty) \cdot \nabla\varphi \, dV - \int_{\Omega\setminus\Omega^\infty} \sigma^\infty \nabla u^\infty \cdot \nabla\varphi \, dV.\end{aligned}$$

We split the boundary of the patch into the part that intersects the boundary of the head and the part that does not and see that

$$\int_{\partial\Omega} \sigma^\infty \frac{\partial u^\infty}{\partial n} \varphi \, dS - \int_{\Omega\setminus\Omega^\infty} \sigma^\infty \nabla u^\infty \cdot \nabla\varphi \, dV$$

$$= \int_{\partial\Omega} \sigma^\infty \frac{\partial u^\infty}{\partial n} \varphi \, dS - \int_{\partial(\Omega\setminus\Omega^\infty)} \sigma^\infty \frac{\partial u^\infty}{\partial n} \varphi \, dS - \underbrace{\int_{\Omega\setminus\Omega^\infty} \nabla \cdot (\sigma^\infty \nabla u^\infty)\varphi \, dV}_{=0}$$

$$= \int_{\partial\Omega^\infty} \sigma^\infty \frac{\partial u^\infty}{\partial n_{\Omega^\infty}} \varphi \, dS,$$

because we can split the boundary integrals.
So, we have

$$\begin{aligned}\int_\Omega \sigma \nabla u^{\text{corr}} \cdot \nabla\varphi \, dV = -\int_{\tilde\Omega} \sigma \nabla(\chi u^\infty) \cdot \nabla\varphi \, dV - \int_{\partial\Omega^\infty} \sigma^\infty \frac{\partial u^\infty}{\partial n_{\Omega^\infty}} \varphi \, dS \\ - \int_{\Omega^\infty} \sigma^{\text{corr}} \nabla u^\infty \cdot \nabla\varphi \, dV,\end{aligned}$$

which finally leads to the weak formulation:
Let $a\colon H(\Omega) \times H(\Omega) \to \mathbb{R}$ be the bilinear form

$$a(w, v) = \int_\Omega \sigma \nabla w \cdot \nabla v \, dV$$

and let $l\colon H(\Omega) \to \mathbb{R}$ be the bilinear form

$$l(v) = -\int_{\tilde{\Omega}} \sigma \nabla(\chi \cdot u^{\infty}) \cdot \nabla v \, dV - \int_{\partial\Omega^{\infty}} \sigma^{\infty} \frac{\partial u^{\infty}}{\partial n} v \, dS \\ - \int_{\Omega^{\infty}} \sigma^{\mathrm{corr}} \nabla u^{\infty} \cdot \nabla v \, dV.$$

The continuous Galerkin method with the local subtraction approach is then given by finding $u^{\mathrm{corr}} \in H(\Omega)$ such that

$$a(u^{\mathrm{corr}}, v) = l(v)$$

for all $v \in H(\Omega)$ and then calculating $u = \chi u^{\infty} + u^{\mathrm{corr}}$.
If we look at $v \in H(\Omega)$ with $v = 0$ almost everywhere on $\Omega^{\infty} \cup \tilde{\Omega}$ we get $l(v) = 0$. So only the test functions whose support intersects the Ω^{∞} or $\tilde{\Omega}$ will give entries in the right-hand side that are non-zero, so the right-hand side vector is sparse, which leads to the significantly lower computation time compared to the classical subtraction approach [20]. When choosing Ω to be the entire patch Ω^{∞}, so $\Omega^{\infty} = \Omega$, the local subtraction approach becomes the classical subtraction approach. For a detailed evaluation of its performance and the existence and uniqueness of the solution, we refer to [20].

3.5.2 Local Subtraction Approach for CEM

We first want to derive a weak formulation for the PDE 3.2 with the boundary conditions for CEM 3.6 - 3.8. Our Hilbert space is the direct sum of $H(\Omega)$ and $\mathbb{R}^L$. We are looking for a bilinear form $a\colon (H(\Omega) \oplus \mathbb{R}^L) \times (H(\Omega) \oplus \mathbb{R}^L) \to \mathbb{R}$ and a linear form $l\colon H(\Omega) \times \mathbb{R}^L \to \mathbb{R}$, such that

$$a((u, U), (\varphi, \Phi)) = l((\varphi, \Phi))$$

for all $(\varphi, \Phi) \in H(\Omega) \oplus \mathbb{R}^L$.
Again, we have $u = u^{\mathrm{corr}} + \chi u^{\infty}$ and $\sigma = \sigma^{\mathrm{corr}} + \sigma^{\infty}$. This leads to the boundary conditions for the CEM:

$$\begin{array}{rcll} \nabla \cdot (\sigma \nabla u^{\mathrm{corr}}) & = & -\nabla \cdot (\sigma^{\mathrm{corr}} \nabla \chi u^{\infty}) - \nabla \cdot (\sigma^{\infty} \nabla (\chi - 1) u^{\infty}) & \text{in } \Omega, \\ \sigma \frac{\partial u^{\mathrm{corr}}}{\partial n}(x) & = & -\sigma \frac{\partial \chi u^{\infty}}{\partial n}(x) & \forall x \in \partial\Omega \setminus \cup_{l=1}^{L} e_l \\ \int_{e_l} \sigma \frac{\partial u}{\partial n}(x) dS & = & I_l & \forall l \in \{1, ..., L\} \\ \sigma \frac{\partial u^{\mathrm{corr}}}{\partial n}(x) & = & \frac{1}{Z_l}(U_l - u) - \sigma \frac{\partial \chi u^{\infty}}{\partial n} & \text{on } e_l, \forall l \in \{1, ..., L\}. \end{array}$$

We multiply again the left-hand side with φ, integrate over Ω and do partial integration and get

$$\int_{\Omega} (\nabla \cdot (\sigma \nabla u^{\mathrm{corr}})) \varphi \, dV = \int_{\partial\Omega} \sigma \frac{\partial u^{\mathrm{corr}}}{\partial n} \varphi \, dS - \int_{\Omega} \sigma \nabla u^{\mathrm{corr}} \cdot \nabla \varphi \, dV$$

$$= \int_{\partial\Omega \setminus \cup_{l=1}^{L} e_l} \sigma \frac{\partial u^{\mathrm{corr}}}{\partial n} \varphi \, dS + \sum_{l=1}^{L} \int_{e_l} \sigma \frac{\partial u^{\mathrm{corr}}}{\partial n} \varphi \, dS - \int_{\Omega} \sigma \nabla u^{\mathrm{corr}} \cdot \nabla \varphi \, dV.$$

and with the first and third boundary condition this becomes

$$-\int_{\partial\Omega\setminus\cup_{l=1}^{L}e_l}\sigma\frac{\partial\chi u^\infty}{\partial n}\varphi\,dS+\sum_{l=1}^{L}\int_{e_l}\frac{1}{Z_l}(U_l-u)\varphi\,dS-\sum_{l=1}^{L}\int_{e_l}\sigma\frac{\partial\chi u^\infty}{\partial n}\varphi\,dS-\int_{\Omega}\sigma\nabla u^{\text{corr}}\cdot\nabla\varphi\,dV.$$

We continue with the right-hand side and multiply a test function φ, integrate over Ω and then do partial integration:

$$\begin{aligned}\int_{\Omega}\big(-\nabla\cdot(\sigma^{\text{corr}}\nabla(\chi u^\infty))\varphi-\nabla\cdot(\sigma^\infty\nabla((\chi-1)u^\infty))\varphi\big)\,dV&\\ =-\int_{\partial\Omega}\sigma^{\text{corr}}\frac{\partial(\chi u^\infty)}{\partial n}\varphi\,dS-\int_{\partial\Omega}\sigma^\infty\frac{\partial((\chi-1)u^\infty)}{\partial n}\varphi\,dS&\\ +\int_{\Omega}\sigma^{\text{corr}}\nabla(\chi u^\infty)\cdot\nabla\varphi\,dV+\int_{\Omega}\sigma^\infty\nabla((\chi-1)u^\infty)\cdot\nabla\varphi\,dV.&\end{aligned}$$

Just like in ([20], page 6), this is

$$=\int_{\partial\Omega^\infty}\sigma^\infty\frac{\partial u^\infty}{\partial n}\varphi\,dS-\int_{\partial\Omega}\sigma\frac{\partial\chi u^\infty}{\partial n}\varphi\,dS+\int_{\Omega^\infty}\sigma^{\text{corr}}\nabla u^\infty\cdot\nabla\varphi\,dV+\int_{\Omega\setminus\Omega^\infty}\sigma\nabla\chi u^\infty\cdot\nabla\varphi\,dV$$

for the right-hand side. Multiplying both sides with -1 and then equating the two sides gives us

$$\int_{\partial\Omega\setminus\cup_{l=1}^{L}e_l}\sigma\frac{\partial\chi u^\infty}{\partial n}\varphi\,dS-\sum_{l=1}^{L}\int_{e_l}\frac{1}{Z_l}(U_l-u)\varphi\,dS+\sum_{l=1}^{L}\int_{e_l}\sigma\frac{\partial\chi u^\infty}{\partial n}\varphi\,dS+\int_{\Omega}\sigma\nabla u^{\text{corr}}\cdot\nabla\varphi\,dV$$

$$=-\int_{\partial\Omega^\infty}\sigma^\infty\frac{\partial u^\infty}{\partial n}\varphi\,dS+\int_{\partial\Omega}\sigma\frac{\partial\chi u^\infty}{\partial n}\varphi\,dS-\int_{\Omega^\infty}\sigma^{\text{corr}}\nabla u^\infty\cdot\nabla\varphi\,dV.-\int_{\Omega\setminus\Omega^\infty}\sigma\nabla\chi u^\infty\cdot\nabla\varphi\,dV.$$

Again, we use $u=u^{\text{corr}}+\chi u^\infty$ and transform the equation to

$$\int_{\Omega}\sigma\nabla u^{\text{corr}}\cdot\nabla\varphi\,dV-\sum_{l=1}^{L}\int_{e_l}\frac{1}{Z_l}(U_l-u^{\text{corr}})\varphi\,dS$$

$$=-\int_{\partial\Omega\setminus\cup_{l=1}^{L}e_l}\sigma\frac{\partial\chi u^\infty}{\partial n}\varphi\,dS-\sum_{l=1}^{L}\int_{e_l}\sigma\frac{\partial\chi u^\infty}{\partial n}\varphi\,dS-\int_{\partial\Omega^\infty}\sigma^\infty\frac{\partial u^\infty}{\partial n}\varphi\,dS+\int_{\partial\Omega}\sigma\frac{\partial\chi u^\infty}{\partial n}\varphi\,dS$$

$$-\int_{\Omega^\infty}\sigma^{\text{corr}}\nabla u^\infty\cdot\nabla\varphi\,dV-\int_{\Omega\setminus\Omega^\infty}\sigma\nabla\chi u^\infty\cdot\nabla\varphi\,dV-\sum_{l=1}^{L}\int_{e_l}\frac{1}{Z_l}\chi u^\infty\varphi\,dS.$$

Due to

$$0=-\int_{\partial\Omega\setminus\cup_{l=1}^{L}e_l}\sigma\frac{\partial\chi u^\infty}{\partial n}\varphi\,dS-\sum_{l=1}^{L}\int_{e_l}\sigma\frac{\partial\chi u^\infty}{\partial n}\varphi\,dS+\int_{\partial\Omega}\sigma\frac{\partial\chi u^\infty}{\partial n}\varphi\,dS$$

and

$$-\int_{\Omega\setminus\Omega^\infty} \sigma\nabla\chi u^\infty \cdot \nabla\varphi \, dV = -\int_{\tilde{\Omega}} \sigma\nabla\chi u^\infty \cdot \nabla\varphi \, dV$$

the equation gets simplified to

$$\int_\Omega \sigma\nabla u^{\text{corr}} \cdot \nabla\varphi \, dV - \sum_{l=1}^{L} \int_{e_l} \frac{1}{Z_l}(U_l - u^{\text{corr}})\varphi \, dS$$

$$= -\int_{\partial\Omega^\infty} \sigma^\infty \frac{\partial u^\infty}{\partial n}\varphi \, dS - \int_{\Omega^\infty} \sigma^{\text{corr}}\nabla u^\infty \cdot \nabla\varphi \, dV - \int_{\tilde{\Omega}} \sigma\nabla\chi u^\infty \cdot \nabla\varphi \, dV - \sum_{l=1}^{L} \int_{e_l} \frac{1}{Z_l}\chi u^\infty \varphi \, dS.$$

Again, we want to have a bilinear form a on the left-hand side and a linear form on the right-hand side, so we introduce $\Phi \in \mathbb{R}^L$ and formulate the weak formulation as the following:
Find $(u, U) \in H(\Omega) \oplus \mathbb{R}^L$, such that

$$\int_\Omega \sigma\nabla u^{\text{corr}} \cdot \nabla\varphi \, dV + \sum_{l=1}^{L} \int_{e_l} \frac{1}{Z_l}(U_l - u^{\text{corr}})(\Phi_l - \varphi) \, dS$$

$$= -\int_{\partial\Omega^\infty} \sigma^\infty \frac{\partial u^\infty}{\partial n}\varphi \, dS - \int_{\Omega^\infty} \sigma^{\text{corr}}\nabla u^\infty \cdot \nabla\varphi \, dV$$

$$-\int_{\tilde{\Omega}} \sigma\nabla\chi u^\infty \cdot \nabla\varphi \, dV + \sum_{l=1}^{L} \int_{e_l} \frac{1}{Z_l}\chi u^\infty(\Phi_l - \varphi) \, dS. \tag{3.21}$$

for all $(\varphi, \Phi) \in H(\Omega) \oplus \mathbb{R}^L$.
This leads us to the same left-hand side as in the general weak formulation of the CEM and the right-hand side is the same as in the local subtraction approach for PEM, but additionally with the term $\sum_{l=1}^{L} \int_{e_l} \frac{1}{Z_l}\chi u^\infty(\Phi_l - \varphi) \, dS$, which is only non-zero if the patch or the transition region intersects with the electrode interfaces.
Since the additional term $\sum_{l=1}^{L} \int_{e_l} \frac{1}{Z_l}\chi u^\infty(\Phi_l - \varphi) \, dS$ is zero for $1 \in H(\Omega) \oplus \mathbb{R}^L$, which is defined as the element which has the coefficient 1 for each basis element in the linear combination, the argument of uniqueness and the existence of [20] also holds for the CEM with the local subtraction approach.

Chapter 4

Numerical Methods

4.1 Finite Element Method

After having the models in the continuous case, the natural next step is to make the solution or approximation of the solution computable. In this step, it is necessary to bring it to a discrete setting. There are different methods that can be used. Three very common methods in our field are the boundary element method (BEM) (see [26]) and the finite element method (FEM). Finite element methods seem to deal very well with complex geometries and anisotropic conductivities [8].
While we were looking for a $u \in H(\Omega)$, with $H(\Omega)$ being - in general - an infinite dimensional Sobolev space we now restrict ourselves on a finite dimensional subspace of H of dimension N, namely $S_N \subset H(\Omega)$, for the test and trial space and approximate the potential on this space. This will bring us to an equation of the form $Ax = b$. We denote the bilinear form as a with test functions φ and the linear functional on the right-hand side as l, so in the weak formulation, we have to find a $u \in H(\Omega)$, which fulfills

$$a(u, \varphi) = l(\varphi)\,, \quad \forall \varphi \in H(\Omega).$$

We denote the solution in the finite dimensional subspace $S_N \subset H(\Omega)$ as u_N:

$$a(u_N, \varphi) = l(\varphi) \;\; \forall \varphi \in S_N.$$

We have a finite basis $\{\psi_1, ..., \psi_N\}$ of S_N, so it is sufficient to make sure that the equation above is fulfilled for every basis function, because of the linearity in the argument φ:

$$a(u_N, \psi_i) = l(\psi_i) \quad \forall i \in \{1, ..., N\}.$$

We can also represent u_N as a linear combination of the basis functions with $x_j \in \mathbb{R}$ for $j \in \{1, ..., N\}$:

$$u_N = \sum_{j=1}^{N} x_j \psi_j.$$

So, in the finite dimensional spaces, computing u_N is equivalent to solving the linear system

$$a(\sum_{j=1}^{N} x_j\psi_j, \psi_i) = \sum_{j=1}^{N} x_j a(\psi_j, \psi_i) = l(\psi_i),\ \forall i \in \{1, ..., N\}$$

which can be described by a matrix-vector equation of the form

$$A \cdot x = b$$

with $A_{ij} = a(\psi_j, \psi_i)$, $x = (x_1, ..., x_N)^{\intercal}$ and $b = (l(\psi_1), ..., l(\psi_N))^{\intercal}$. The coefficients of the linear combination of u_N that are captured in x are calculated.

The method that approximates the solution on finite dimensional subspaces is called the Galerkin method. The theory is described in detail in ([2], chapter II §4) where the convergence of the approximations on the subspaces with increasing dimension to the solution in the space of infinite dimension is also investigated.

Now, that we know the general idea, we take a look at the construction of finite element spaces, which are used as the finite dimensional subspaces $S_N \subset H(\Omega)$ of the Sobolev spaces for the trial and test spaces in the Galerkin method.

For this, we divide the problem domain into smaller and simpler subdomains, which are called finite elements. These elements can have different shapes, while commonly used shapes are tetrahedra or hexahedra. In this thesis, we exclusively use tetrahedral elements. We introduce some basic definitions and use the same notations as in [2]:

Definition 3. Let $K \subset \mathbb{R}^n$ be a bounded and closed set with a non-empty interior and piecewise smooth boundary, which we call the element domain.

1. Let $\mathcal{P}$ be a finite-dimensional space of functions on K, which is called the space of shape functions.
2. Let $\mathcal{N} = \{N_1, ..., N_k\}$ be a basis for the dual space $\mathcal{P}'$, which are called the nodal variables.

$(K, \mathcal{P}, \mathcal{N})$ is called a finite element.

Definition 4. Let $(K, \mathcal{P}, \mathcal{N})$ be a finite element. The nodal basis of $\mathcal{P}$ is the basis $\{\varphi_1, ..., \varphi_k\}$ of $\mathcal{P}$, which is dual to $\mathcal{N}$, which means $N_i(\varphi_j) = \widetilde{\delta_{ij}}$ with $\widetilde{\delta_{ij}}$ being the Kronecker delta.

Within each finite element, the solution is approximated by a simple function and the global solution is constructed by combining the local solutions over all elements.

A common choice for a finite element for a domain Ω is the polynomials of degree less than or equal to k, $\mathcal{P}_k$ and the nodal variables $\mathcal{N} = \{N_0, ..., N_k\}$ where $N_i(v) = v(r_i)$ with $r_i \in K \subset \Omega$.

We will now introduce our choice of finite elements, which are the Lagrangian elements on a tetrahedral mesh. In this work, we do the simulations on tetrahedral meshes. So, we have 4 nodes per mesh element. We can define a finite element on one mesh element by $K \subset \Omega$ being the tetrahedral mesh element, $\mathcal{P}_1$ being the function space of polynomials of degree less than or equal to 1 in K and the nodal variables $\mathcal{N} = \{N_1, ..., N_4\}$ being the evaluation of the polynomials at the node positions.

We set the nodal basis of $\mathcal{P}_1$ to be the linear functions $\{\varphi_1, ..., \varphi_4\}$ where $N_i(\varphi_j) = \widetilde{\delta}_{ij}$. Because $\mathcal{P}$ is chosen to be the space of linear functions, the nodal basis functions are also called hat functions, because of the visualization in the two-dimensional case where the value of the hat functions is shown in the third dimension. Here, the i-th Lagrange function looks like a hat with its hat tip on the i-th node and then linearly decreases to 0 on the other nodes.
In [36] the usage of polynomials of higher degree is considered.

4.2 FEM for PEM

For the FEM with PEM the solution space and test space are $S_N \subset H(\Omega)$. Let $\{\psi_1, ..., \psi_N\}$ be the basis of S_N. Then, for an $i \in \{1, .., N\}$ and $u = \sum\limits_{j=1}^{N} u_j \psi_j$ and $u_j \in \mathbb{R}$ for $j \in \{1, ..., N\}$, we have

$$a\Big(\sum_{j=1}^{N} u_j \psi_j, \psi_i\Big) = \sum_{j=1}^{N} u_j \underbrace{\int_{\Omega} \sigma \nabla \psi_j \nabla \psi_i \, dV}_{=:a_{ij}} . \tag{4.1}$$

So, the FEM becomes the matrix-vector equation

$$Au = l \tag{4.2}$$

with

$$(A)_{i,j} = \int_{\Omega} \sigma \nabla \psi_j \nabla \psi_i \, dV \tag{4.3}$$

and $A \in \mathbb{R}^{N \times N}$, and the coefficients for the linear combination of u, which is also denoted by $u = (u_1, ..., u_N)^\intercal$. The right-hand side is denoted by $l = (l(\psi_1), ..., l(\psi_N))^\intercal$.
Since we want not only the existence of the solution but also uniqueness, it is shown in ([21], theorem 15) that the symmetric matrix A gets symmetric positive definite if we set $u_1 = 0$ and

$$\tilde{A} = \begin{pmatrix} 1 & 0 & \cdots & 0 \\ 0 & (A)_{2,2} & \cdots & (A)_{2,n} \\ \vdots & \vdots & \ddots & \vdots \\ 0 & (A)_{n,2} & \cdots & (A)_{n,n} \end{pmatrix} \quad \text{and} \quad \tilde{l} = \begin{pmatrix} 0 \\ l(\psi_2) \\ \vdots \\ l(\psi_n) \end{pmatrix} \tag{4.4}$$

and thus the system $\tilde{A}u = \tilde{l}$ has a unique solution. This solution also solves $Au = l$.

4.3 FEM for CEM

For the CEM, the discretization with FEM is more difficult since it also has the potentials at the electrodes as L additional dimensions, so with the domain Ω the solution

space and the test space is $S_N \oplus \mathbb{R}^L$. Let $\{\psi_1, ..., \psi_N\}$ be the basis of S_N and the standard basis $\{\tilde{e_1}, ..., \tilde{e_L}\}$ of $\mathbb{R}^L$. We use the tilde here, because the e_l are already used for the electrodes. Then $\{(\psi_1, 0), ..., (\psi_N, 0), (0, \tilde{e_1}), ..., (0, \tilde{e_L}))\}$ is a basis of $S_N \oplus \mathbb{R}^L$. We approximate $(u, U) \in S_N \oplus \mathbb{R}^L$ as a linear combination $(u, U) = (\sum\limits_{j=1}^{N} u_j \cdot (\psi_j, 0)) + (\sum\limits_{l=1}^{L} \tilde{U_l} \cdot (0, \tilde{e}_l))$. Because we chose the standard basis of $\mathbb{R}^L$, we have $\tilde{U_l} = U_l$, so we will simply neglect it and write U_l. We will do the same for Φ in $(\varphi, \Phi) \in S_N \oplus \mathbb{R}^L$. We want to calculate the stiffness matrix and also have
$(\varphi, \Phi) = (\sum\limits_{i=1}^{N} \varphi_i \cdot (\psi_i, 0)) + (\sum\limits_{l=1}^{L} \Phi_l \cdot (0, \tilde{e}_l))$. So we reduce the weak formulation to the basis functions and start with a basis function $(\psi_i, 0)$ for an $i \in \{1, ..., N\}$:

$$a((u, U), (\psi_i, 0)) = -\sum_{l=1}^{L} \int_{e_l} \frac{1}{Z_l}(U_l - u)\psi_i \, dS + \int_\Omega \sigma \nabla u \cdot \nabla \psi_i \, dV.$$

Considering the linear combination of (u, U) brings us to

$$a((u, U), (\psi_i, 0)) = a((\sum_{j=1}^{N} u_j \cdot (\psi_j, 0), U), (\psi_i, 0))$$

$$= -\sum_{l=1}^{L} \int_{e_l} \frac{1}{Z_l} U_l \psi_i \, dS + \sum_{l=1}^{L} \int_{e_l} \frac{1}{Z_l} (\sum_{j=1}^{N} u_j \psi_j) \psi_i \, dS + \int_\Omega \sigma \nabla (\sum_{j=1}^{N} u_j \psi_j) \nabla \psi_i \, dV$$

$$= \sum_{l=1}^{L} U_l \underbrace{(-\frac{1}{Z_l} \int_{e_l} \psi_i \, dS)}_{=b_{il}} + \sum_{j=1}^{N} u_j \underbrace{((\sum_{l=1}^{L} \frac{1}{Z_l} \int_{e_l} \psi_j \psi_i \, dS) + \int_\Omega \sigma \nabla \psi_j \nabla \psi_i \, dV)}_{=a_{ij}}$$

and we set the matrix $A \in \mathbb{R}^{N \times N}$ with $(A)_{ij} = a_{ij}$ and $B \in \mathbb{R}^{N \times L}$ with $(B)_{il} = b_{il}$. Let $x \in \mathbb{R}^N$ be $Au + BU = x$ while we abbreviated the vectors of coefficients $u = (u_1, ..., u_N)^\intercal$ and $U = (U_1, ..., U_L)$.
We will do the same for an arbitrary $l \in \{1, ..., L\}$ and the basis element $(0, \tilde{e}_l)$:

$$a((u, U), (0, \tilde{e}_l)) = \int_{e_l} \frac{1}{Z_l}(U_l - u) \, dS$$

and again

$$a((\sum_{j=1}^{N} u_j \cdot (\psi_j, 0), U), (0, \tilde{e}_l)) = \int_{e_l} \frac{1}{Z_l}(U_l - u) \, dS = U_l \int_{e_l} \frac{1}{Z_l} \, dS + \sum_{j=1}^{N} u_j (-\frac{1}{Z_l} \int_{e_l} \psi_j \, dS).$$

We set $C \in \mathbb{R}^{L \times L}$ as the diagonal matrix with entries $(C)_{ll} = \frac{1}{Z_l} \int_{e_l} dS$ and also write it as $(C)_{ll} = \frac{|e_l|}{Z_l}$. Let $y \in \mathbb{R}^L$ be the result of this equation that we write in a matrix-vector equation:

$$B^\intercal u + CU = y.$$

In total, we can represent the two equations in one matrix-vector equation

$$\begin{pmatrix} A & B \\ B^{\intercal} & C \end{pmatrix} \begin{pmatrix} u \\ U \end{pmatrix} = \begin{pmatrix} x \\ y \end{pmatrix} \tag{4.5}$$

with the matrices $A \in \mathbb{R}^{N\times N}$,$B \in \mathbb{R}^{N\times L}$ and $C \in \mathbb{R}^{L\times L}$ with

$$(A)_{ij} = \int_{\Omega} \sigma \nabla \psi_j \cdot \nabla \psi_i \, dV + \sum_{l=1}^{L} \int_{e_l} \frac{1}{Z_l} \psi_j \psi_i \, dS \tag{4.6}$$

$$(B)_{il} = -\int_{e_l} \frac{1}{Z_l} \psi_i \, dS \tag{4.7}$$

$$(C)_{ll} = \frac{1}{Z_l} \int_{e_l} dS \quad \text{and} \quad (C)_{kl} = 0, \quad \text{for } k \neq l. \tag{4.8}$$

4.4 Transfer Matrix Approach

In an EEG measurement, we only have the measured potentials at the L electrodes. Based on this information, the underlying electric activity needs to be calculated. This is called the inverse problem and requires the forward simulation of a number of sources in the range of tens of thousands of sources. Calculating the whole potential on the entire domain Ω for all these sources is computationally very expensive and thus infeasible. Here, we use the transfer matrix approach. The transfer matrix approach is used to calculate the measured potentials with the electrodes caused by a given dipole without calculating the potential in the entire domain and thus solving the inverse problem more effectively with less computation time [62],([33], chapter 1.2),([21], chapter 2.4).

We will first explain the transfer matrix approach for the PEM. The evaluations of the potential at the electrode positions can be expressed as the application of a linear operator $R\colon \mathbb{R}^N \to \mathbb{R}^L$ resulting in:

$$U = Ru,$$

where $U \in \mathbb{R}^L$ is the vector $U = (U_1, ..., U_L)$ consisting of the measured electric potential U_l with the l-th electrode and u being the electric potential at the N nodes of the mesh. Let $p_1, ..., p_L \in \mathbb{R}^L$ be the positions of the L electrodes. The entries $r_{k,i}$ of the matrix, which represents the linear operator R are defined as:

$$r_{k,i} = \psi_i(p_1) - \psi_i(p_k),$$

where ψ_i denotes the i-th basis function of the finite element space.

Since the solution to the EEG forward problem is determined only up to a constant, the first electrode is selected as the reference electrode and its value is set to zero.

By replacing the solution u with $A^{-1}l$, we can express the potential evaluations at the electrodes as:

$$U = RA^{-1}l = Tl,$$

where $T = RA^{-1} \in \mathbb{R}^{L \times N}$ is the transfer matrix.
The transfer matrix T can be computed by solving

$$A^{\intercal} T^{\intercal} = R^{\intercal},$$

while taking the symmetry of the matrix A into account. The solution can be obtained for each column of T and $R^{\intercal}$ separately and once the transfer matrix T is computed, the potential differences at the electrode positions can be evaluated by assembling the right-hand side vector and performing a matrix-vector multiplication.
Therefore, to compute the measurement vectors U for an arbitrary number of dipoles, the linear system needs to be solved only $(L-1)$ times. It does not have to be solved L times since we have a reference electrode.

4.5 Schur Complement for CEM

We also want to derive a transfer matrix approach for the CEM. Here, the matrix on the left-hand side is more complicated since it consists of three different kind of block-matrices. To find a suitable approach we will use the Schur complement here.
We start with the matrix-vector equation and use the concept of Schur complements. We have

$$\begin{pmatrix} A & B \\ B^{\intercal} & C \end{pmatrix} \begin{pmatrix} u \\ U \end{pmatrix} = \begin{pmatrix} x \\ y \end{pmatrix}$$

and derive the two equations from it

$$Au + BU = x$$

$$B^{\intercal} u + CU = y$$

We multiply the first equation from the left with $B^{\intercal} A^{-1}$ and get

$$B^{\intercal} u + B^{\intercal} A^{-1} B U = B^{\intercal} A^{-1} x.$$

We subtract this from the second equation and have

$$(C - B^{\intercal} A^{-1} B) U = y - B^{\intercal} A^{-1} x.$$

Now, the expression of U is

$$U = (C - B^{\intercal} A^{-1} B)^{-1} y - (C - B^{\intercal} A^{-1} B)^{-1} B^{\intercal} A^{-1} x.$$

This is the expression we use for the EEG forward problem. If the patch for the local subtraction approach does not intersect with at least one electrode interface, y will be zero. This will basically always be the case, because of the number of vertex extensions and the resolution of the mesh. The case where the patch or the transition region intersects electrode interfaces is also implemented.
We calculate and store the matrices $(C - B^{\intercal} A^{-1} B)^{-1}$, $B^{\intercal} A^{-1}$ and $(C - B^{\intercal} A^{-1} B)^{-1} B^{\intercal} A^{-1}$.

We calculate the matrix $B^\intercal A^{-1}$ via the following equation: We set

$$B^\intercal A^{-1} = T^\intercal \Longleftrightarrow T = A^{-1}B \Longleftarrow AT = B$$

and solve this to get T and then transpose it.
For the tES, we look at u and we can do similar calculations and get

$$u = (A - BC^{-1}B^\intercal)^{-1}(x - BC^{-1}y).$$

In the stimulation, we have $x = 0$, because of having no source that we set in the volume conductor, so the expression for u becomes

$$u = -(A - BC^{-1}B^\intercal)^{-1}BC^{-1}y.$$

Now, we have two matrices

$$-(A - BC^{-1}B^\intercal)^{-1}BC^{-1} \text{ and } -(C - B^\intercal A^{-1}B)^{-1}B^\intercal A^{-1}$$

for the EEG forward problem with $y = 0$ and the tES with $x = 0$. Based on the principle of reciprocity - which is also shown for CEM - we can expect that

$$-(A - BC^{-1}B^\intercal)^{-1}BC^{-1} = -[(C - B^\intercal A^{-1}B)^{-1}B^\intercal A^{-1}]^\intercal.$$

The following calculations will show this identity: We begin with the two representations of the inverse that we achieve by the application of Gaussian elimination on the blockmatrix form of the stiffness matrix for CEM:
We get a zero matrix for the lower left block matrix by

$$\begin{pmatrix} I_N & 0 \\ -B^\intercal A^{-1} & I_L \end{pmatrix} \cdot \begin{pmatrix} A & B \\ B^\intercal & C \end{pmatrix} = \begin{pmatrix} A & B \\ 0 & C - B^\intercal A^{-1}B \end{pmatrix}$$

and get a zero matrix for the upper right block matrix by

$$\begin{pmatrix} I_N & 0 \\ -B^\intercal A^{-1} & I_L \end{pmatrix} \cdot \begin{pmatrix} A & B \\ B^\intercal & C \end{pmatrix} \cdot \begin{pmatrix} I_N & -A^{-1}B \\ 0 & I_L \end{pmatrix} = \begin{pmatrix} A & 0 \\ 0 & C - B^\intercal A^{-1}B \end{pmatrix}.$$

We take the inverse of both sides and multiply the two matrices on the left-hand side to the right-hand side and have

$$\begin{pmatrix} A & B \\ B^\intercal & C \end{pmatrix}^{-1} = \begin{pmatrix} I_N & -A^{-1}B \\ 0 & I_L \end{pmatrix} \cdot \begin{pmatrix} A^{-1} & 0 \\ 0 & (C - B^\intercal A^{-1}B)^{-1} \end{pmatrix} \cdot \begin{pmatrix} I_N & 0 \\ -B^\intercal A^{-1} & I_L \end{pmatrix},$$

and by analogous computations, we also have

$$\begin{pmatrix} A & B \\ B^\intercal & C \end{pmatrix}^{-1} = \begin{pmatrix} I_N & 0 \\ -C^{-1}B^\intercal & I_L \end{pmatrix} \cdot \begin{pmatrix} (A - BC^{-1}B^\intercal)^{-1} & 0 \\ 0 & C^{-1} \end{pmatrix} \cdot \begin{pmatrix} I_N & -BC^{-1} \\ 0 & I_L \end{pmatrix}.$$

So the two left-hand sides are equaling each other, so with straight-forward calculations, we have

$$\left(\begin{array}{c|c} A^{-1} + A^{-1}B(C - B^\intercal A^{-1}B)^{-1}B^\intercal A & -A^{-1}B(C - B^\intercal A^{-1}B)^{-1} \\ \hline -(C - B^\intercal A^{-1}B)^{-1}B^\intercal A^{-1} & (C - B^\intercal A^{-1}B)^{-1} \end{array}\right) =$$

$$\left(\begin{array}{c|c} (A - BC^{-1}B^\intercal)^{-1} & -(A - BC^{-1}B^\intercal)^{-1}BC^{-1} \\ \hline -C^{-1}B^\intercal(A - BC^{-1}B^\intercal)^{-1} & C^{-1} + C^{-1}B^\intercal(A - BC^{-1}B^\intercal)^{-1}BC^{-1} \end{array}\right).$$

while the lines are used to make the separation of the entries clearer. This leads to the equality of the upper right entries:

$$-A^{-1}B(C - B^\intercal A^{-1}B)^{-1} = -(A - BC^{-1}B^\intercal)^{-1}BC^{-1},$$

but since the matrices are symmetric, we can exchange the left-hand side with the transposed of the lower left entry and end up with

$$[-(C - B^\intercal A^{-1}B)^{-1}B^\intercal A^{-1}]^\intercal = -(A - BC^{-1}B^\intercal)^{-1}BC^{-1}.$$

This was the desired result. This enables us to implement the tES and DBS easily after we have implemented the EEG and iEEG forward solver, respectively.

4.6 Convergence of CEM to PEM with $r \to 0$ in FEM

The convergence of the CEM to the PEM for the radius r going to zero can also be seen in the FEM. The proof of the convergence is from [22].

We look at the measured potentials U, with $y = 0$ (so the the patch for the dipole does not grow into the electrode interfaces), and have

$$U = -(C - B^\intercal A^{-1}B)^{-1}B^\intercal A^{-1}x.$$

This is also

$$U = -(I_L - C^{-1}B^\intercal A^{-1}B)^{-1}C^{-1}B^\intercal A^{-1}x$$

with the identity matrix $I_L \in \mathbb{R}^{L\times L}$. When we remember the entries of the matrices from A (see 4.6), we see that for $r \to 0$, $A^{-1}x$ converges to the vector with the coefficients for the PEM, because the second term with the integrals over the electrode interfaces vanishes and we end up with the classical FEM for PEM. We denote this vector by $A^{-1}x = u^{\text{PEM}} \in \mathbb{R}^N$

We will have a closer look at $C^{-1}B^\intercal$ before $r \to 0$ and see for the entry in the l-th row and the i-th column that

$$(C^{-1}B^\intercal)_{li} = -\frac{Z_l}{|e_l|}\frac{1}{Z_l}\int\limits_{e_l} \varphi_i \, dS = -\frac{\int\limits_{e_l} \varphi_i \, dS}{|e_l|}$$

and with $r \to 0$, so $|e_l| \to 0$, we have

$$(C^{-1}B^\intercal)_{li} \xrightarrow{r\to 0} -\varphi_i(x_{e_l})$$

with the coordinate of the center of the integral x_{e_l} to where the electrode interface $|e_l|$ has shrunk.
While we have the given convergence for $C^{-1}B^\intercal$ and A^{-1} for the matrix product in the brackets, the matrix B goes to zero for $r \to 0$, so we have

$$U = -(I_L - C^{-1}B^\intercal A^{-1}B)^{-1}C^{-1}B^\intercal A^{-1}x \xrightarrow{r\to} C^{-1}B^\intercal u^{\mathrm{PEM}}$$

and because of $(C^{-1}B^\intercal)_{il} = \varphi_i(x_{e_l})$, we have in the limit

$$U_l = \sum_{i=1}^{N} \varphi_i(x_{e_l})u_i^{\mathrm{PEM}} = u^{\mathrm{PEM}}(x_{e_l})$$

which is the measured potential for the PEM. So, the CEM gives the same U as the PEM for $r \to 0$ without the necessity of the impedances going to infinity.

Chapter 5

Numerical Implementation in DUNEuro

The numerical implementation is made in the DUNEuro software toolbox. It builds up on the software toolbox DUNE. We will only give a quick insight into the software toolbox and refer for more details to [45] and [47].

5.1 DUNEuro

The implementation of the CEM is made in the software toolbox called DUNEuro. DUNEuro is an open-source, C++-based software toolbox, which is designed for the numerical computation of forward solutions in bioelectromagnetism [47]. It has a modular structure which we benefited from in the implementation of CEM. It provides various FEM implementations in neuroscientific applications including EEG and MEG. The PEM was the only and thus the default model in EEG.

DUNEuro supports various source models for solving the EEG forward problem, such as the St. Venant [58], partial integration [60], Whitney [34], and subtraction approaches [63] including the most recent local subtraction approach [20]. The software offers a Python and MATLAB interface. We used the Python interface for the tests and simulations.

DUNEuro is built on the DUNE framework, which is also an open source C++ software toolbox of advanced FEM [45]. In this thesis, the simulations are done with the continuous Galerkin (CG-FEM) and specifically with Lagrange basis functions, even though various FEMs are already implemented and are possible to use.

5.2 Mesh

The choice of the mesh is an important and necessary step in complex modeling to get the problem in a discrete setting. It makes the solution ”computable” by approximating it to a finite number of elements. With the help of imaging techniques like MRI, we can get a more precise model of the head. It allows certain inclusions of realistic model properties depending on how much detail the mesh allows. Naturally, with increasing mesh resolution the computation time also increases, but with the benefit of higher accuracy and realism. There are methods that deal better with certain limitations, e.g. the low resolution, i.e. the discontinuous Galerkin method [8]. This method deals well with so called skull leakages, where due to a low resolution of the skin and CSF compartments are linked through a node and the currents take "short cuts", which lead to non-physical results in the simulations [8]. With the surface-based meshing approaches and resolutions that we deal with in this thesis, the continuous Galerkin method is a legitimate choice.

Both, tetrahedral and hexahedral meshes can be used in solving the EEG forward problem. The tetrahedral meshes have the advantage that smooth tissue surfaces can be well represented in the model, compared to hexahedral meshes, where the surface has to be modeled using cube-like elements, although the generation of tetrahedral meshes from voxel-based MRI data is a more difficult task than the generation of hexahedral meshes [8].

In this work, we use only tetrahedral meshes, with high resolution (1 mm mesh resolution). Specifically, the meshes are the following:

The mesh *sphere1mm* is generated with the software toolbox *Gmsh* which is an open source 3D finite element mesh generator [13][15]. *sphere1mm* is a sphere with 4 layers with the radii 78, 80, 86, 92 mm and the compartments brain, CSF, skull, skin and the conductivities 0.00033, 0.00179, 0.00001 and 0.00043 $\frac{S}{mm}$, respectively. The mesh resolution was set to 1 mm. It has about 2.4 million nodes and 14.6 million tetrahedral elements. The dipoles were generated from a set of points on the unit sphere, which were scaled up to a sphere of radius 78 mm because 78 mm is the radius of the sphere for the brain compartment. The radius is multiplied by the eccentricity of 0.98 attain dipoles that are realistically placed about 1.5 mm away from the next conductivity jump. Radial and tangential moments were assigned to these dipoles positions. This mesh with these dipoles is used for the EEG forward simulations.

Since spherical models do not include the complex folding of the cortex which leads to a more complicated brain-CSF interface (see figure 5.1) which effects the current flow in the head, more realistic models are desired. In this thesis, we also performed simulations on a realistic head model.

For this, T1, T2 and DTI (see [43][54] for DTI) MRI scans (see [23] for T1 and T2 MRI scans) of a healthy adult male subject who gave written informed consent according to the declaration of Helsinki prior to the measurement, which was approved by the ethics committee of the University of Münster (#2015-263-f-S), were measured. Using the CHARM pipeline [35], a realistic volume conductor model was constructed consisting of ca. 730 000 nodes and 4.1 million tetrahedral elements. This mesh is called *realisticMesh*.

We generated 47 983 dipoles which are placed realistically close to the cortex and did the simulations for the choice of all three unit moments $(1, 0, 0)$, $(0, 1, 0)$, and $(0, 0, 1)$ as the moments of the dipole. This mesh with the dipoles is also used for the EEG forward simulations and an investigation on tES.

For the simulations of iEEG and DBS we also created a spherical model with *Gmsh*. For this we created a spherical model with the same layers and conductivities as in *sphere1mm*, but additionally with three cylinders cut out for the depth electrodes, see figure 5.2. The mesh that we used for iEEG and DBS with CEM, we call *sphere_DBS* and it has the three bases (entries given in millimeters) for the cylinders:

$$\text{base}_1 = (145, 127, 127), \quad \text{base}_2 = (127 \cdot \frac{\sqrt{3}}{2}, 136, 127)$$

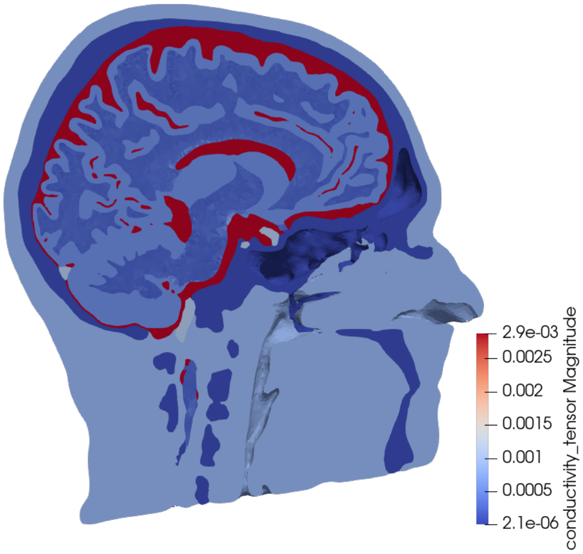

Figure 5.1: This figure shows a clip of *realisticMesh*. The complex foldings of the cortex are visible at the brain-CSF interface (the CSF is marked red because of its higher conductivity) and the more complex representation of the brain compartment. The lighter blue brain compartment is the gray matter and the darker blue brain compartment is the white matter where the anisotropy is included. Here, the magnitude of the conductivity tensor for each element is shown.

$$\text{base}_3 = (127 + 18 \cdot \cos(\frac{\pi}{12}), 127 + 18 \cdot \sin(\frac{\pi}{12}), 127).$$

The direction of them are

$$\text{dir}_1 = (1, 0, 0), \quad \text{dir}_2 = (\frac{\sqrt{3}}{2}, \frac{1}{2}, 0) \quad \text{dir}_3 = (\cos(\frac{\pi}{12}), \sin(\frac{\pi}{12}), 0).$$

The total length of a depth electrode is set to 190 mm, the length of a contact is 2.25 mm with spacings in between with a length of 0.75 mm and the cylinder has a radius of 0.43 mm. The resolution parameter for the electrodes is set to 0.25 mm and the resolution parameter for the rest of the mesh is set to 3 mm. In figure 5.3 a slice of the mesh is visible with the depth electrodes.

For the iEEG and DBS it is a sensible step to create a mesh which also has the higher resolution for the cylinders, but with the cylinders assigned to the compartments where they ly in.. This is what we did for *sphere_DBS_PEM*. The structure of the cylinders are also present in the mesh, but the cylinder parts are assigned to the corresponding 4 compartments of the underlying spherical mesh, which we can see in figure 5.3. Apart from that, *sphere_DBS* and *sphere_DBS_PEM* have same mesh structure. Each of both meshes has about 1.6 million nodes and 10 million tetrahedral elements.

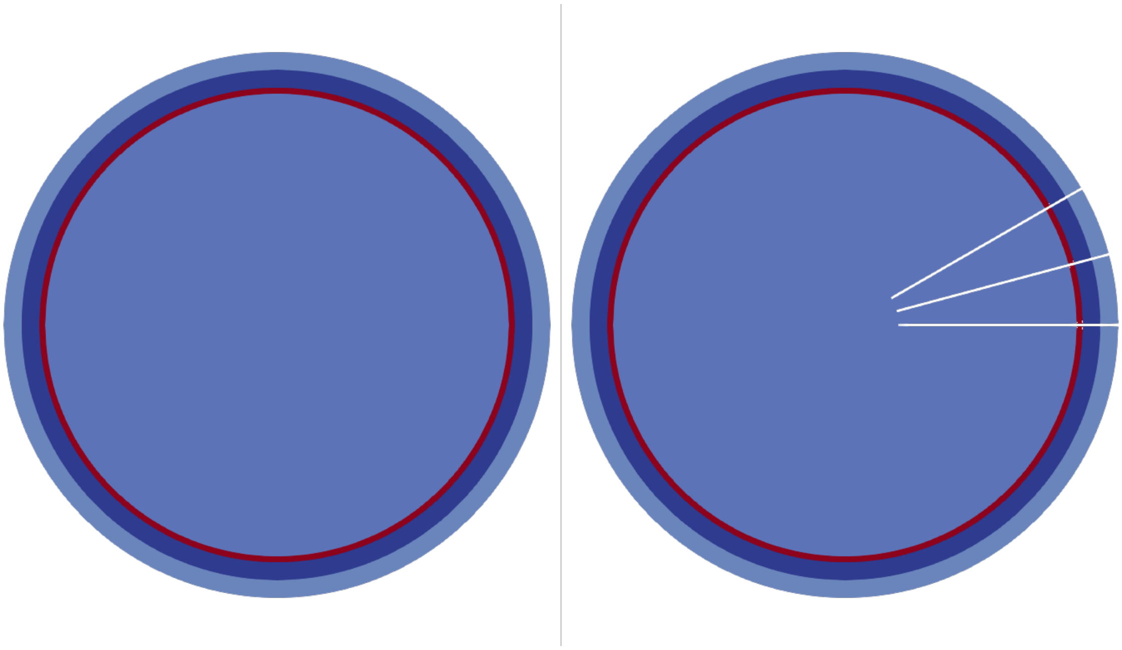

Figure 5.2: This figure shows a slice of the meshes *sphere_DBS_PEM* (left) and *sphere_DBS* (right). The four compartments are also visible.

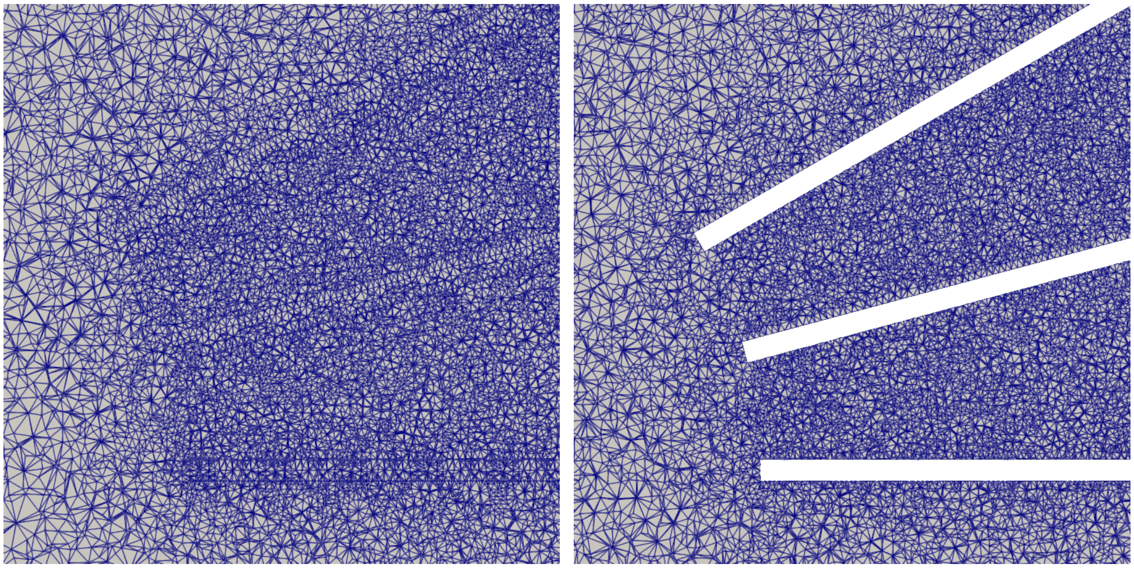

Figure 5.3: This figure shows a slice of *sphere_DBS_PEM* (left) and *sphere_DBS* (right) with visible edges of the mesh elements. It is visible that *sphere_DBS_PEM* also has the depth electrodes in its mesh structure, but also includes their volume.

5.3 CI Pipeline and Example Code

DUNEuro is a software toolbox that started in 2016 and is a collaborative work where the contributions of each contributor can have high interdependencies and thus it is of importance to create an environment in which the usability, coherence and functionality of the code is guaranteed, also on different machines and compiler setups. To guarantee this, a continuous integration (CI) pipeline was setup to have tests that run on different environments as soon as new versions of DUNEuro get committed to DUNEuro's GitLab repository. To this CI pipeline, we additionally integrated a test for CEM, using linear basis functions, the continuous Galerkin method, and the local subtraction approach as the source model to ensure that even future contributions to the DUNEuro framework keep the functionality and utility of the implemented CEM code.

Over the entire simulations, we have high-resolution tetrahedral meshes, the continuous Galerkin method with linear basis functions as the FEM-solver, and the local subtraction approach as the source model.

For the linear systems that we solve in the FEM approach, we use the preconditioned conjugate gradient solver with an algebraic multigrid preconditioner (see [42][44]).

Exemplarily, we show how to set the drivers for CEM and PEM using the Python interface. For the CEM, we additionally need for the electrodes the electrode projection type, impedances and the radius for the electrodes. The impedances are entered as a `impedances.txt` file which holds the ACI values for the *i*-th electrode in the *i*-th line while the radius must be given as one value (in millimeters) and is then the radius for all electrodes. Here, the radius is set to 10 mm for the electrodes and an impedance file `impedances.txt` is chosen. The electrode projection type is `cem_radial` which means that the boundary faces whose centers are less than 10 mm away from the center of the face that is the closest to the electrode coordinate gets added to the corresponding electrode interface. The Python code is shown in the following page:

```
# create driver for PEM
mesh_cfg_pem = {’nodes’ : nodes, ’elements’ : elements}
tensor_cfg_pem = {’labels’ : labels, ’conductivities’ : conductivities}
volume_conductor_cfg_pem = {’grid’ : mesh_cfg_pem, ’tensors’ :
    tensor_cfg_pem}
driver_cfg_pem = {’type’ : ’fitted’, ’solver_type’ : ’cg’, ’element_type
    ’ : ’tetrahedron’, ’electrode_model’ : ’pem’, ’post_process’ : ’true
    ’, ’subtract_mean’ : ’true’}
solver_cfg_pem = {’reduction’ : ’1e-14’, ’edge_norm_type’ : ’houston’, ’
    penalty’ : ’20’, ’scheme’ : ’sipg’, ’weights’ : ’tensorOnly’}
driver_cfg_pem[’solver’] = solver_cfg_pem
driver_cfg_pem[’volume_conductor’] = volume_conductor_cfg_pem

print(’Creating driver for PEM’)
meeg_driver_pem = dp.MEEGDriver3d(driver_cfg_pem)
print(’Driver created for PEM’)

# set source type for PEM
driver_cfg_pem[’source_model’] = source_model_config_database[
    source_model]

# set electrodes for PEM
print(’Setting electrodes for PEM’)
electrode_cfg_pem = {’type’ : ’closest_subentity_center’ , ’codims’ : ’3
    ’}
meeg_driver_pem.setElectrodes(duneuro_electrodes, electrode_cfg_pem)
print(’Electrodes set for PEM’)

# create driver for CEM
mesh_cfg_cem = {’nodes’ : nodes, ’elements’ : elements}
tensor_cfg_cem = {’labels’ : labels, ’conductivities’ : conductivities}
volume_conductor_cfg_cem = {’grid’ : mesh_cfg_cem, ’tensors’ :
    tensor_cfg_cem}
driver_cfg_cem = {’type’ : ’fitted’, ’solver_type’ : ’cg’, ’element_type
    ’ : ’tetrahedron’, ’electrode_model’ : ’cem’, ’post_process’ : ’true
    ’, ’subtract_mean’ : ’true’}
solver_cfg_cem = {’reduction’ : ’1e-14’, ’edge_norm_type’ : ’houston’, ’
    penalty’ : ’20’, ’scheme’ : ’sipg’, ’weights’ : ’tensorOnly’}
driver_cfg_cem[’solver’] = solver_cfg_cem
driver_cfg_cem[’volume_conductor’] = volume_conductor_cfg_cem

print(’Creating driver for CEM’)
meeg_driver_cem = dp.MEEGDriver3d(driver_cfg_cem)
print(’Driver created for CEM’)

# set electrodes for CEM
print(’Setting electrodes for CEM’)
electrode_cfg_cem = {’type’ : ’cem_radial’, ’impedances_file’ :
    impedances.txt, ’radius’ : 10}
meeg_driver_cem.setElectrodes(duneuro_electrodes, electrode_cfg_cem)
print(’Electrodes set for CEM’)

driver_cfg_cem[’source_model’] = source_model_config_database[
    source_model]
```

5.4 Implementation

The version of the code that we use and present here is available at [14].
DUNEuro is a modular software, which means that it uses a lot of template parameters. The first intuitive step was to build a new way of projecting the electrodes for CEM. For this we added to *duneuro/eeg* (or extended) the files:

- *electrode_projection_factory.hh*
- *electrode_projection_interface.hh*
- *cem_radial_electrode_projection.hh*
- *cem_predefined_electrode_projection.hh*

In *electrode_projection_factory.hh* the class *CEMElectrodeProjectionFactory* for the CEM is added, which has the CEM as the electrode model. The two flags we implemented for the electrode projection are *cem_radial* and *predefined_electrodes*.
In *electrode_projection_interface.hh* the class *ProjectedElectrode* was also extended for the CEM and now additionally holds the impedance and a vector of intersections, called *electrodeInterface* which represent the electrode interface. Here the impedance is the ACI which we give in as a flag to later calculate the ECI including the area of the electrode interface in *cem_radial_electrode_projection.hh* and *cem_predefined_electrode_projection.hh*.
In *cem_radial_electrode_projection.hh* the class *CEMRadialElectrodeProjection* also takes the radius as a variable and has the method *setElectrodes*. Here, the boundary faces of the head are added to *electrodeInterface* if the distance between the global coordinate to which the electrode is projected and the center of the boundary face is less than the given radius. This also leads to electrodes which are not perfect circles, but a union of boundary faces. After generating the *electrodeInterface*, the ECI is calculated by multiplying the given ACI with the sum of the areas of the faces in *electrodeInterface*.
In *cem_predefined_electrode_projection.hh* we assume that we already have the faces which create the *electrodeInterface*. This electrode projection is needed for the iEEG and DBS since here the electrode interface is not at the boundary and can not be achieved by calculating distances to a global coordinate. In this file, the ECIs are also calculated by multiplying the given ACIs by the sum of the areas of the faces of the corresponding *electrodeInterface*.
In *duneuro/eeg* we also extended the files

- *local_subtraction_source_model.hh*
- *local_subtraction_cg_local_operator.hh*
- *local_subtraction_cg_p1_local_operator.hh*
- *analytic_utilities.hh*.

Since for the CEM, the local subtraction approach has one additional term for the right-hand side of the PDE 3.2, the method *postProcessCEM* is implemented in *local_subtraction_source_model.hh*. Here, an object of a local operator is created. For this object the method *assembleElectrodeInterfaces* exists which is implemented in *duneuro/common/ele-*

ment_patch_assembler.hh and checks if the patch or the transition region for the local subtraction source model intersects a face of the *electrodeInterface* of the electrodes and adds the integral over this face to the right-hand side (see the last summand in 3.21) if so with the methods *lambda_patch_electrode_intersection* and *lambda_patch_electrode_intersection_U_l* that are implemented in the local operators.

We have different options for the local operator for the local subtraction source model. The computation can be done numerically. For this, *local_subtraction_cg_local_operator.hh* now also holds the method *assembleElectrodeInterfaces.* In *local_subtraction_source_model.hh*, the method *assembleRightHandSide* checks if we use the continuous Galerkin approach and linear functions in our finite elements and if we are in the isotropic case. It then creates a local operator which uses the analytical expressions of the terms for the right-hand side for the local subtraction approach if all of them hold. So, the file *local_subtraction_cg_p1_local_operator.hh* and *analytic_utilities.hh* are extended for this case and used.

In *duneuro/common*, we added

- *cem_electrode_assembler.hh*
- *cem_local_operator.hh*
- *cem_solver.hh*
- *cem_utilities.hh*

In *cem_electrode_assembler.hh* the matrices for the FEM get assembled, which are called the base Jacobian A (see 4.6), the electrode coupling matrix B (see 4.8), and the electrode interface matrix C (see **??**).

In *cem_local_operator.hh* the contribution of a single element of the mesh to the matrices for the FEM gets added to the matrix entries.

In *cem_solver.hh* the core of the solver is implemented. It contains the methods *setElectrodeProjection*, *setSchurMatrices*, *solve*, *solveEEGForward*, *solveTDCSForward* and some private methods that are called for these methods. While *setElectrodeProjection* sets the projected electrodes, the method *setSchurMatrices* sets the matrices needed for the transfer matrix approach with the Schur complement. The method *solve* executes the transfer matrix approach with the Schur complement while *solveEEGForward* does this for multiple dipoles. In contrast to the solvers for PEM, the transfer matrix approach is implemented in this solver and not in *duneuro/eeg/transfer_matrix_solver.hh.* As the name suggests, *solveTDCSForward* solves the TDCS forward problem for a given injection pattern.

In *cem_utilities.hh* we have a class for the vector structure used for CEM, since we have $N + L$ many entries with N being the number of elements of the mesh and L being the number of electrodes, called *CEMDOFVector*.

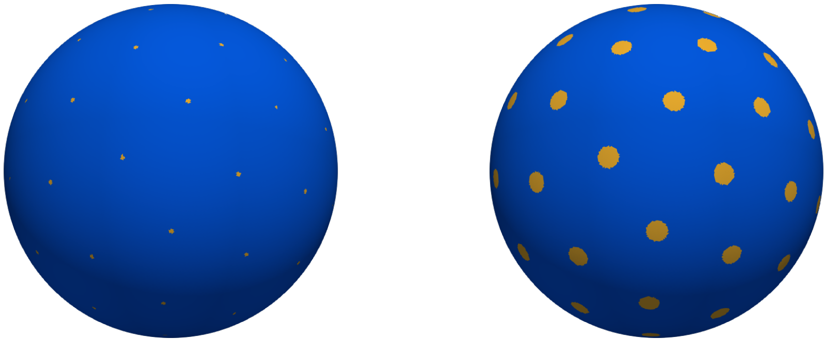

(a) 1mm (b) 5mm

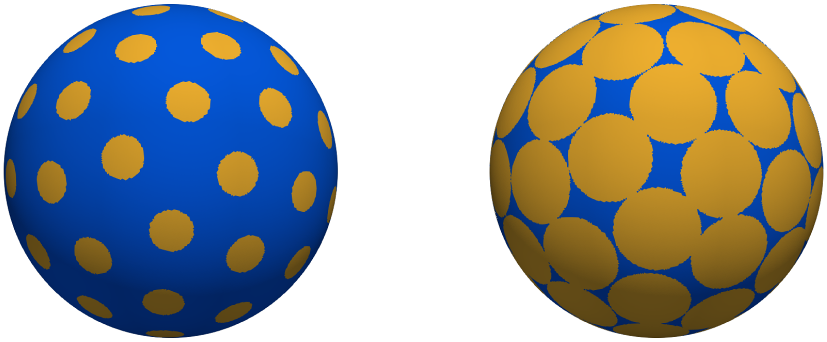

(c) 10mm (d) 20mm

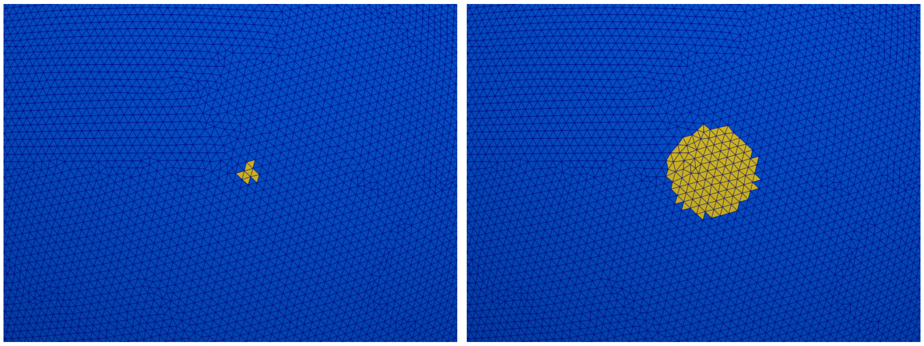

(e) 1mm, close-up with visible edges (f) 5mm, close-up with visible edges

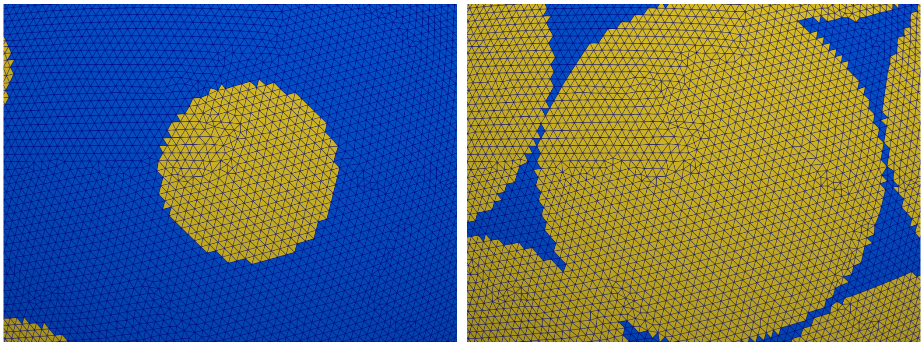

(g) 10mm, close-up with visible edges (h) 20mm, close-up with visible edges

Figure 5.4: Electrodes set with different radii in the spherical model

Chapter 6

Numerical Experiments and Results

While for the PEM, we only need the global coordinates of the electrodes, which are then mapped to a subentity center, the CEM has some additional parameters, which we also give in as flags. These are the radius of the L electrodes and a text file with L-many lines for the average contact impedances of the electrodes. So, it is a natural step to play with these parameters and look at the differences between the CEM and the PEM. The default values for these parameters are 10 mm for the radius, 5000 Ω as the ACI for each electrode and 0.98 as the eccentricity of the dipoles.

6.1 Error Measures

For the comparison of different simulations, we need functions that capture different measures of errors. In the following definitions, the norm is always meant to be the norm in the Lebesgue space $\ell^2(L) = \{(x_1, ..., x_L) \in \mathbb{R}^L : \sum_{i=1}^{L} |x_i|^2 < \infty\}$, which is

$$\|(x_1, ..., x_L)\| = \sqrt{\sum_{i=1}^{L} |x_i|^2}.$$

The relative error (RE) puts the absolute difference of the two potentials in proportion to the reference potential. In this study, the solution with CEM is taken as the reference potential and is denoted by u^{CEM}. Formally, the RE is defined by

$$\mathrm{RE}(u^{\mathrm{PEM}}, u^{\mathrm{CEM}}) = \frac{\|u^{\mathrm{PEM}} - u^{\mathrm{CEM}}\|}{\|u^{\mathrm{CEM}}\|}.$$

We also have the relative difference measure (RDM). By dividing both potentials by their norm, this measure does not take the errors into account that result from different magnitudes. It is defined as

$$\mathrm{RDM}(u^{\mathrm{PEM}}, u^{\mathrm{CEM}}) = \left\| \frac{u^{\mathrm{PEM}}}{\|u^{\mathrm{PEM}}\|} - \frac{u^{\mathrm{CEM}}}{\|u^{\mathrm{CEM}}\|} \right\|.$$

The magnitude error (MAG) measures only the differences in magnitude and does not take the distribution of the potentials into account. Here, the reference potential is also the potential achieved by CEM. It is defined as

$$\mathrm{MAG}(u^{\mathrm{PEM}}, u^{\mathrm{CEM}}) = \frac{\|u^{\mathrm{PEM}}\|}{\|u^{\mathrm{CEM}}\|}$$

and is 1 if u and u^{CEM} have no magnitude error.
To visualize the data, we use the *boxplot* method of *seaborn* (see [50]). The box in the box plot visualize the first three quartiles where the line inside the box is the median, so 50% of the data is below this value. The whiskers extend to show the rest of the distribution, while the points show the outliers.
For the figures, the potential is colored red for positive values and blue for negative value, and the magnitude of the gradient is given as the $\|\cdot\|_2$-norm of the gradient and is colored blue for the lower end of the scale and is colored red for the upper end of the scale.

6.2 EEG Forward Problem

Here we investigate the effects of different eccentricities, radii and impedances for *sphere1mm* and *realisticMesh* and start with the spherical model.

6.2.1 Spherical Head Model

Eccentricity

The eccentricities were logarithmically scaled and rounded to two decimal places for the figures and tables, but listed here after rounding to four decimal places: 0.7832, 0.8712, 0.9098, 0.9348, 0.9534, 0.9681, 0.9804, 0.9908. The ACIs are set to 5000 Ω for all electrodes and the electrode radius is set to 10 mm.
The mean and median of every error measure gets bigger, the higher the eccentricity becomes for radial and tangential dipoles except for the median for radial dipoles, see table 6.1. Here, the errors increase from the eccentricity 0.7832 to 0.9348, but then stay at a similar level or decrease from the eccentricity 0.9534 to 0.9908. This means that for radial dipoles, the outliers are more considerable for higher eccentricities. We can also see this in figure 6.1(a) and 6.1(b). More outliers occur for radial dipoles than for tangential dipoles that also have larger error values.
In figures 6.1(e) and 6.1(f) we can see that the outliers for MAG only appear for higher eccentricities and radial dipoles in a higher number with a larger MAG while for the tangential dipoles the outliers appear for all eccentricities in a lower number with smaller errors. This means that the magnitude difference does not increase much over all eccentricities.
We see the development of the RE and the RDM in the box plots 6.1(a), 6.1(b), 6.1(c)

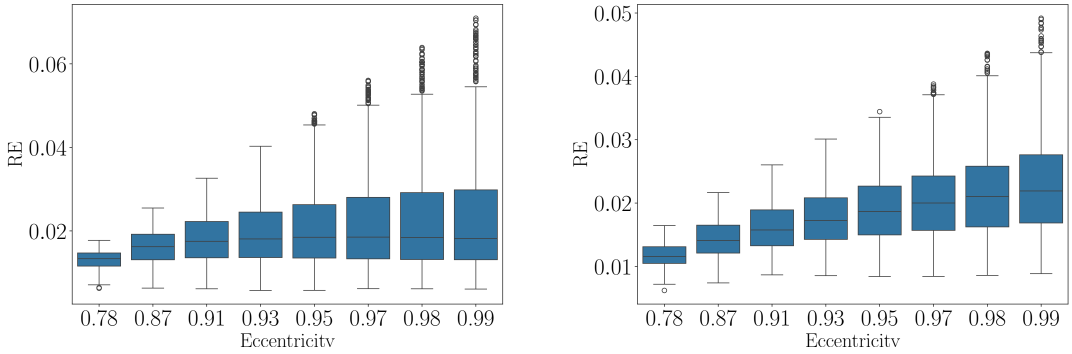

(a) RE, radial (b) RE, tangential

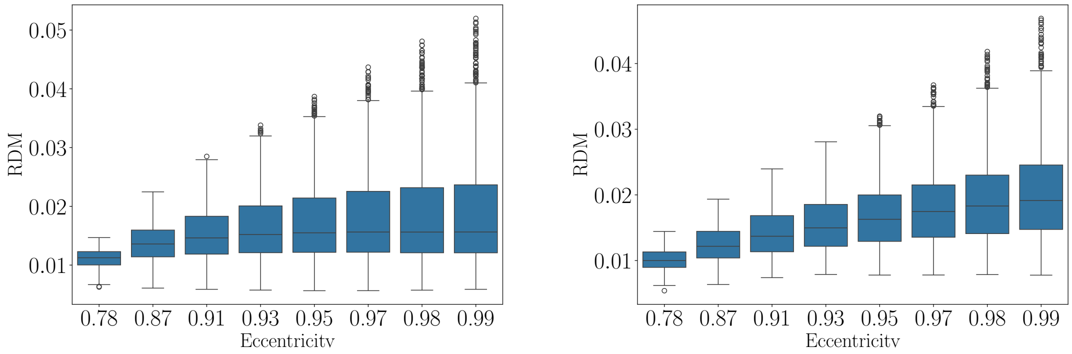

(c) RDM, radial (d) RDM, tangential

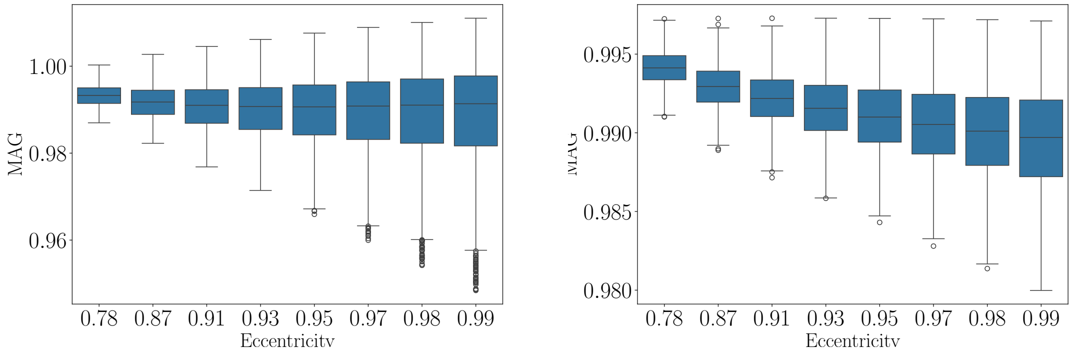

(e) MAG, radial (f) MAG, tangential

Figure 6.1: Error values for PEM and the CEM (reference model) with an electrode radius of 10 mm, ACIs of 5000 Ω, and various eccentricities for the dipoles.

Eccentricities	0.7832	0.8712	0.9098	0.9348	0.9534	0.9681	0.9804	0.9908
Mean error values for radial dipoles								
RE	0.0132	0.0164	0.0183	0.0199	0.0211	0.0223	0.0233	0.0241
RDM	0.0111	0.0138	0.0153	0.0165	0.0173	0.0181	0.0187	0.0191
MAG	1.0067	1.0083	1.0093	1.0101	1.0107	1.0113	1.0118	1.0122
Median error values for radial dipoles								
RE	0.0134	0.0164	0.0177	0.0183	0.0187	0.0187	0.0186	0.0184
RDM	0.0112	0.0136	0.0146	0.0152	0.0155	0.0156	0.0156	0.0156
MAG	1.0068	1.0083	1.0091	1.0094	1.0094	1.0093	1.009	1.0087
Mean error values for tangential dipoles								
RE	0.0118	0.0145	0.0163	0.0179	0.0193	0.0207	0.022	0.0233
RDM	0.0101	0.0125	0.0142	0.0156	0.0169	0.0182	0.0194	0.0205
MAG	1.0059	1.0071	1.0079	1.0086	1.0091	1.0096	1.0101	1.0106
Median error values for tangential dipoles								
RE	0.0116	0.0142	0.0159	0.0174	0.0188	0.0202	0.0213	0.0221
RDM	0.01	0.0122	0.0137	0.015	0.0163	0.0175	0.0183	0.0191
MAG	1.0059	1.0071	1.0079	1.0085	1.0091	1.0096	1.01	1.0104

Table 6.1: Mean and median values of the error measures for PEM and CEM (reference model) for radial and tangential dipoles for various eccentricities

and 6.1(d). We notice that the errors are smaller and the number of outliers is less for the tangential dipoles. This indicates that the CEM makes a bigger difference for radial dipoles with high eccentricities.

Radius

Now, we want to look at the differences between the CEM and the PEM for different radii. The default for the electrode radius for the simulations is 10 mm, which leads to an area of around πcm^2 per electrode interface. Here we investigated the difference between the CEM and the PEM for the radii (in millimeters): 1, 3, 5, 7, 10, 12, 15 and 20.
We look again at the mean and median values for the different measures for 1000 tangential and 1000 radial dipoles with eccentricity 0.98 in table 6.2. This choice is realistic because this brings a distance of 1.5 mm to the next conductivity jump, leading to realistic dipole positions.
Compared to the development of errors for different eccentricities, here, the errors constantly get larger, starting from 3 mm for radial and tangential dipoles. We can see that for tangential dipoles the mean and median values are very close to each other, while for radial dipoles the median and mean differ more. This shows again that for radial dipoles more considerable outliers can appear. We can see this again in the box plots 6.2(a)-6.2(f). We also see that the outliers appear for tangential dipoles also for the smaller radii, but still with smaller errors compared to the case of radial dipoles.
It is interesting to note that the median for all cases in 6.2 decreases or stays the same from 1 mm to 3 mm, but overall we can say that the difference between CEM and PEM increases with bigger radii.

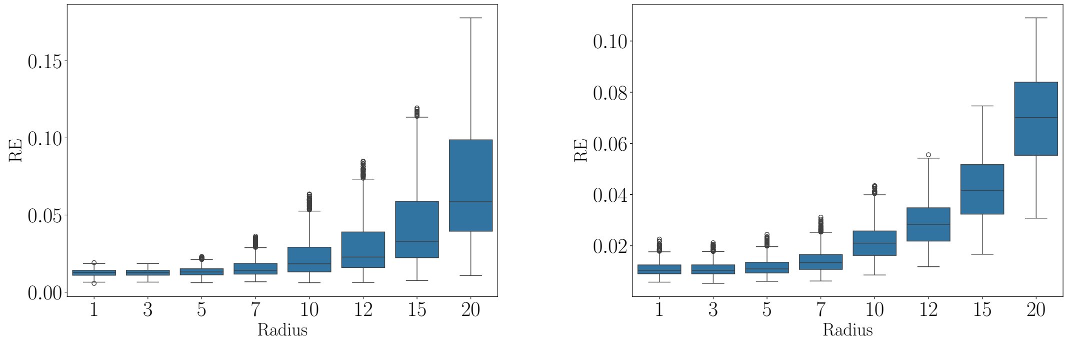

(a) RE, radial

(b) RE, tangential

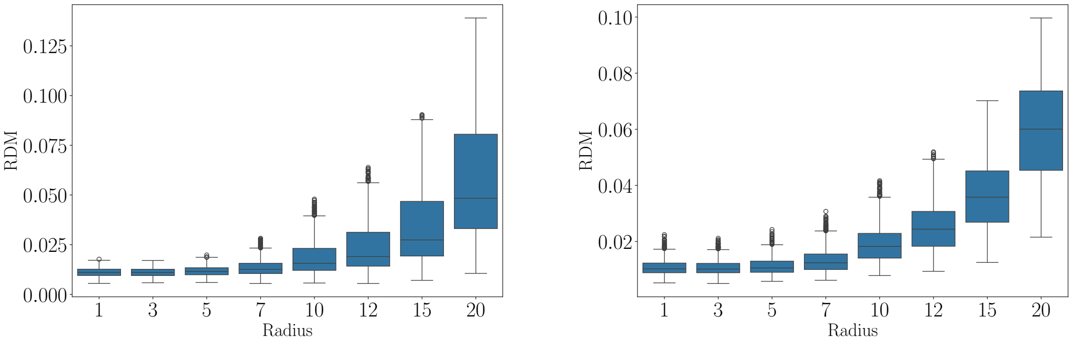

(c) RDM, radial

(d) RDM, tangential

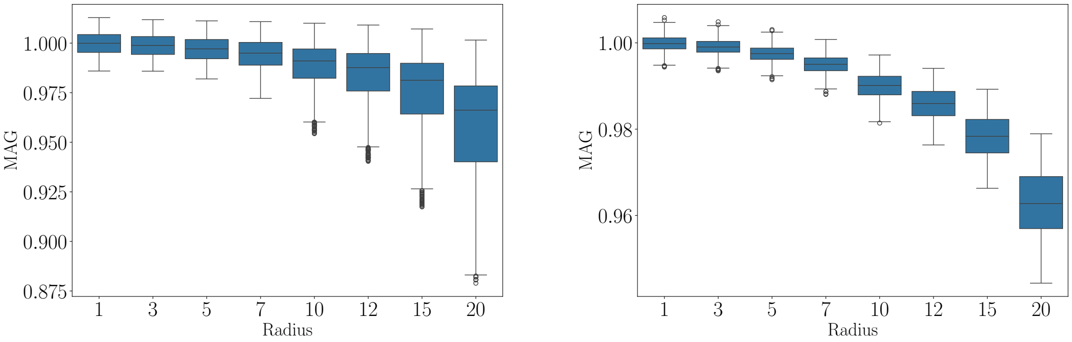

(e) MAG, radial

(f) MAG, tangential

Figure 6.2: Error values for PEM and the CEM (reference model) with various radii for the electrodes, ACIs of 5000 Ω, and an eccentricity of 0.98 for the dipoles.

Radius in mm	1	3	5	7	10	12	15	20
Mean error values for radial dipoles								
RE	0.0126	0.0126	0.0135	0.0161	0.0232	0.0303	0.0444	0.0763
RDM	0.0112	0.0111	0.0117	0.0135	0.0187	0.0239	0.0345	0.0586
MAG	1.0002	1.0011	1.003	1.0058	1.0118	1.0168	1.0263	1.0462
Median error values for radial dipoles								
RE	0.0127	0.0126	0.0131	0.0142	0.0186	0.0231	0.0335	0.0607
RDM	0.0111	0.011	0.0115	0.0126	0.0156	0.019	0.0274	0.0483
MAG	1.0001	1.0012	1.0029	1.0051	1.0091	1.0125	1.0191	1.035
Mean error values for tangential dipoles								
RE	0.011	0.011	0.0118	0.0143	0.022	0.0294	0.0433	0.0722
RDM	0.0109	0.0108	0.0114	0.0133	0.0193	0.0253	0.0365	0.0595
MAG	1.0002	1.001	1.0026	1.0051	1.0101	1.0144	1.0223	1.0388
Median error values for tangential dipoles								
RE	0.0104	0.0104	0.011	0.0134	0.0213	0.0287	0.0426	0.0729
RDM	0.0103	0.0102	0.0106	0.0124	0.0183	0.0244	0.0358	0.0601
MAG	1.0002	1.001	1.0025	1.005	1.01	1.0143	1.0221	1.0387

Table 6.2: Mean and median values of the error measures for PEM and CEM (reference model) for radial and tangential dipoles for various radii

Impedances

We want to look at the effect of different ACIs. Realistically, the ACIs, which are measured and then set before the simulation are between 3000 and 5000 Ω. The question arises of how very low, realistic, and very high impedances effect the simulation. The set of 8 impedance files are abbreviated in the following figures as *5000, 0.00001, 1, rand50, rand5000, rand500000, 500000, rand3000-5000.* Here, the single numbers without the *"rand"* represent the impedance files that have this number as the ACI for all electrodes. The impedance files with the additional *"rand"* and a number x are impedance files that have randomly generated impedances between 0 and x or in the case of *rand3000-5000* numbers between 3000 and 5000 generated by the `numpy.random.rand()` method.

Looking at the mean and median values for the radial and tangential dipoles two main things get clear: We can classify the impedance files into two groups if it comes to their errors: (*0.00001, 1, rand50*) and (*5000, rand5000, rand500000, 500000, rand3000-5000*). In the first group, the errors are considerably high due to the shunting currents. In table 6.3, we see for low impedances a clear difference between the CEM and the PEM. The differences between the mean and median values for radial dipoles and low impedances are comparably low to those of the second group. In the second group, all errors for radial dipoles are quite low, but the difference between the mean and the median is larger. So, we can see that the lower the impedances, the better the model handles possible outliers in the radial dipoles. We can also see this in figures 6.3(a)-6.3(f). We have some nice ways to visualize this. For this, we visualized the gradient and the potential distribution for a radial dipole with the impedance files *5000* and *0.00001* in the figures 6.4 and 6.5 respectively. In figure 6.4 we can clearly see how the potential passes through the electrode,

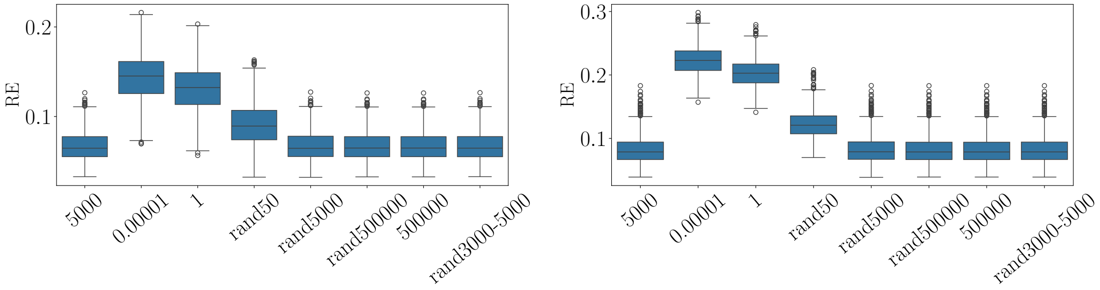

(a) RE, radial (b) RE, tangential

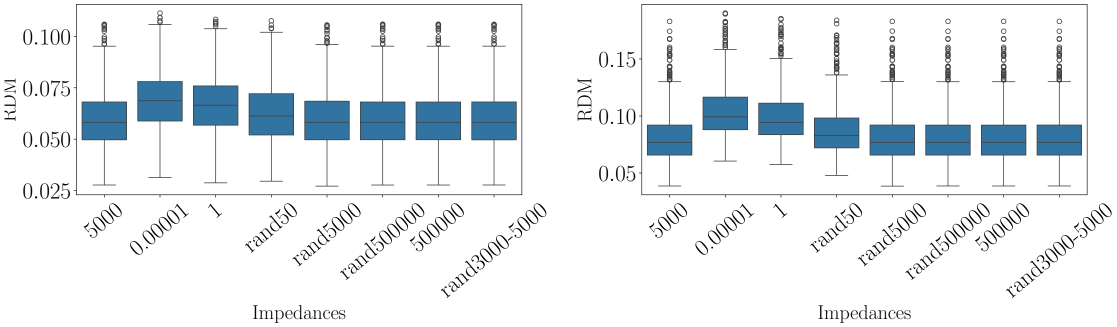

(c) RDM, radial (d) RDM, tangential

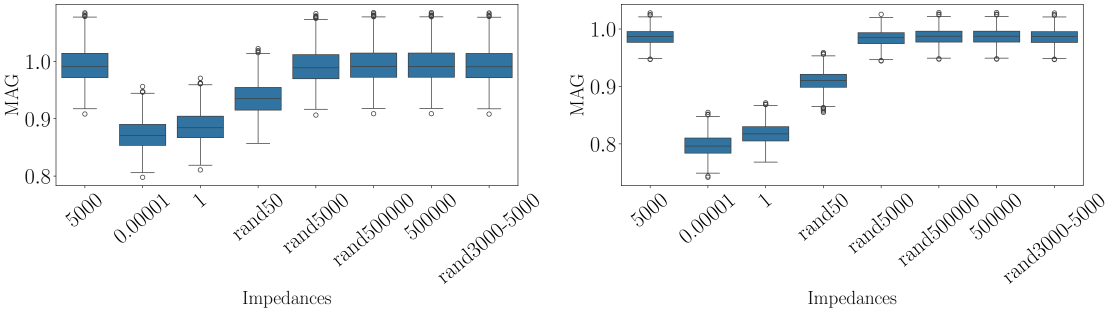

(e) MAG, radial (f) MAG, tangential

Figure 6.3: Error values for PEM and the CEM (reference model) with an electrode radius of 10 mm, various files for the ACIs, and an eccentricity of 0.98 for the dipoles.

Impedance files	*5000*	*0.00001*	*1*	*rand50*	*500000*
Mean error values for radial dipoles					
RE	0.0228	0.1375	0.1234	0.0737	0.0226
RDM	0.0187	0.0422	0.0384	0.0275	0.0186
MAG	0.9885	0.8682	0.882	0.9313	0.9891
Median error values for radial dipoles					
RE	0.0184	0.1359	0.1218	0.0718	0.0181
RDM	0.0156	0.0414	0.0376	0.0265	0.0156
MAG	0.991	0.8697	0.8834	0.933	0.9916
Mean error values for tangential dipoles					
RE	0.0218	0.1317	0.1181	0.0703	0.0215
RDM	0.0193	0.0397	0.0363	0.0265	0.0193
MAG	0.99	0.8737	0.887	0.9347	0.9906
Median error values for tangential dipoles					
RE	0.021	0.1312	0.1176	0.0691	0.0208
RDM	0.0183	0.0389	0.3558	0.0254	0.0182
MAG	0.9901	0.8739	0.8873	0.9354	0.9907

Table 6.3: Mean and median values of the error measures for PEM and CEM (reference model) for radial and tangential dipoles for various impedance files

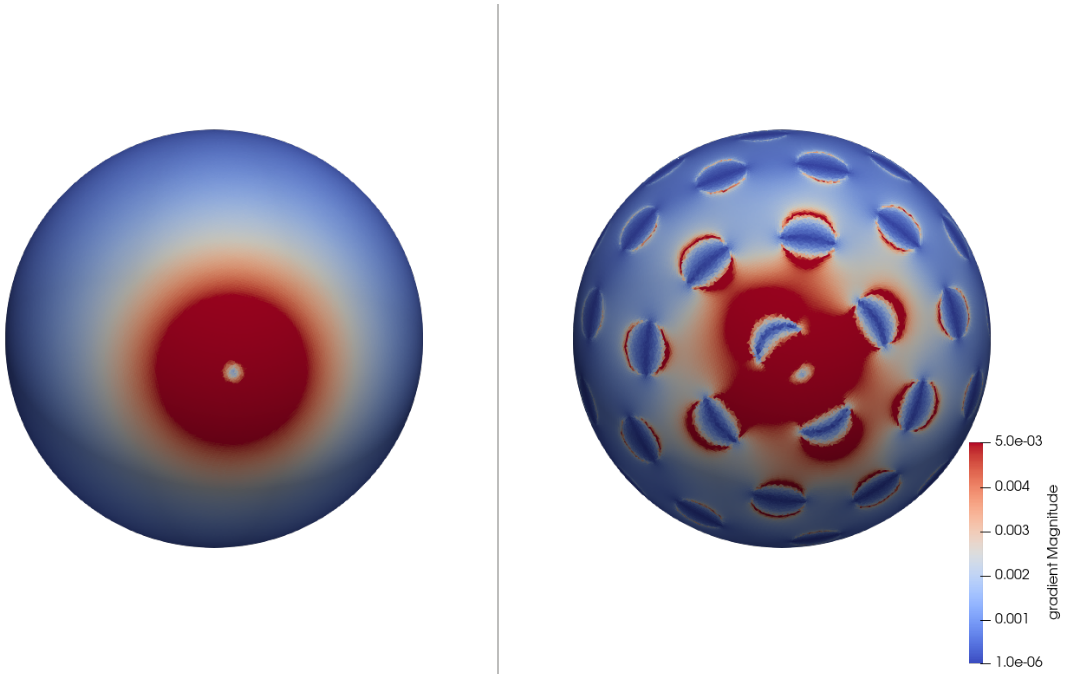

Figure 6.4: The magnitude of the gradient is visualized for a radial dipole and for the cases of a realistic array of impedances *5000* (left) and for an array of unrealistically low impedances *0.00001* (right).

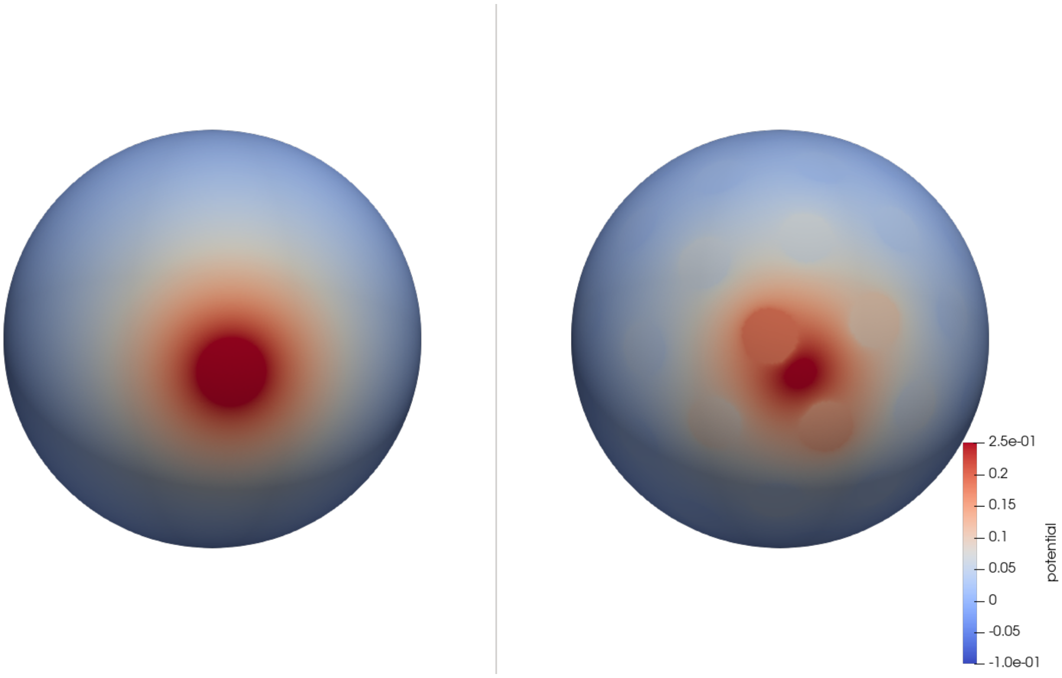

Figure 6.5: The potential distribution for a realistic impedances *5000* (left) and for unrealistically low impedances *0.00001* for a radial dipole is shown.

which is modeled to have infinite conductivity. So, the current flows into the electrode at one part of the edge of the electrode interface and leaves the electrode at that part of the edge that is the most distant to the part of the edge where the current entered the electrode.
In the figure 6.5, we can see the potential distribution. For the impedance file *5000* the electrode interfaces are not clearly visible, while for the impedance file *0.00001* the potential at the electrode interface is averaged. This is due to the third boundary condition 3.8. We see in the figures 6.3(a)-6.3(f) that the difference between very high impedances and realistic impedances is not really notable. A considerable difference appears only for the impedances that are very low.

6.2.2 Realistic Head Model

We want to investigate the effects of different impedances for *realisticMesh*. Recall that here we do the simulations with 143949 dipoles to put the number of outliers in the box plots into perspective. We investigate for the radii 0.00001, 10 and 15 the effects of all impedance files from the previous section. The simulations showed again that the investigation of the impedance files *5000*, *0.00001*, *1*, *rand50*, and *500000* are sufficient. So, for a better representation of the results, we only show the mean and median values for these impedances in the tables.

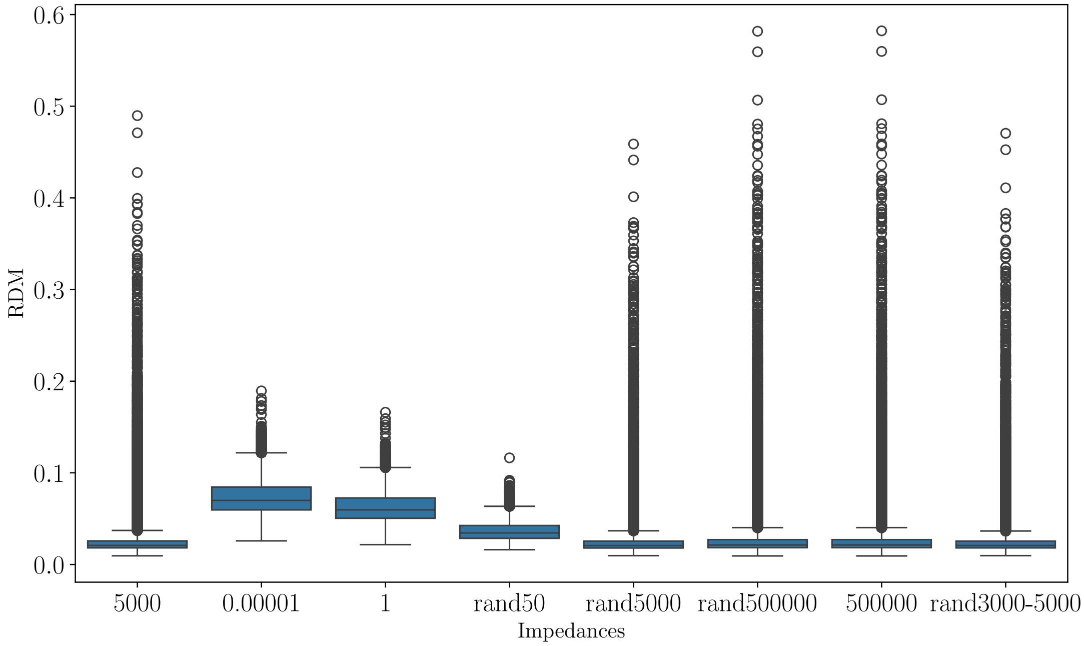

Figure 6.6: RDM between the PEM and the CEM (reference model) for the 143949 dipoles and with 57 electrodes with radius 10 mm and various impedance files.

Radius = 10 mm

First, some issues appeared for the classical case of having electrodes with a radius of 10 mm.

If we look at the RDM in the figures 6.6, we see a very high number of outliers with large RDM values. Having a look at figure 6.7, it is visible that two of the 57 electrodes are placed nonphysically. The electrodes intersect the ear and even the electrode interface at the right ear is not connected. So, this has to be paid attention to by the user of the CEM for realistic head models.

In the next step, we erase these electrodes and have 55 electrodes left. If we now look at the figure 6.8, we see that the number of outliers decreased considerably and the error values of the outliers are also considerably lower.

This shows that the non-physically set electrodes were a considerable source of the error. As we would expect, the errors are getting considerably high for very low impedances and the gradient and potential distribution is again shown in figures 6.9 and 6.10.

Single Face Electrode Interfaces

A sufficiently small radius is chosen (here, it is 0.00001 mm) to include the case in which the electrode interface of an electrode is a single face on the boundary. We can see this in figure 6.11. The PEM was adapted to this case by evaluating the computed potential at the coordinate of the center of this face. By the calculations in 4.6, we expect that the difference between the PEM and the CEM goes to zero for higher impedances. We also check this numerically in this section.

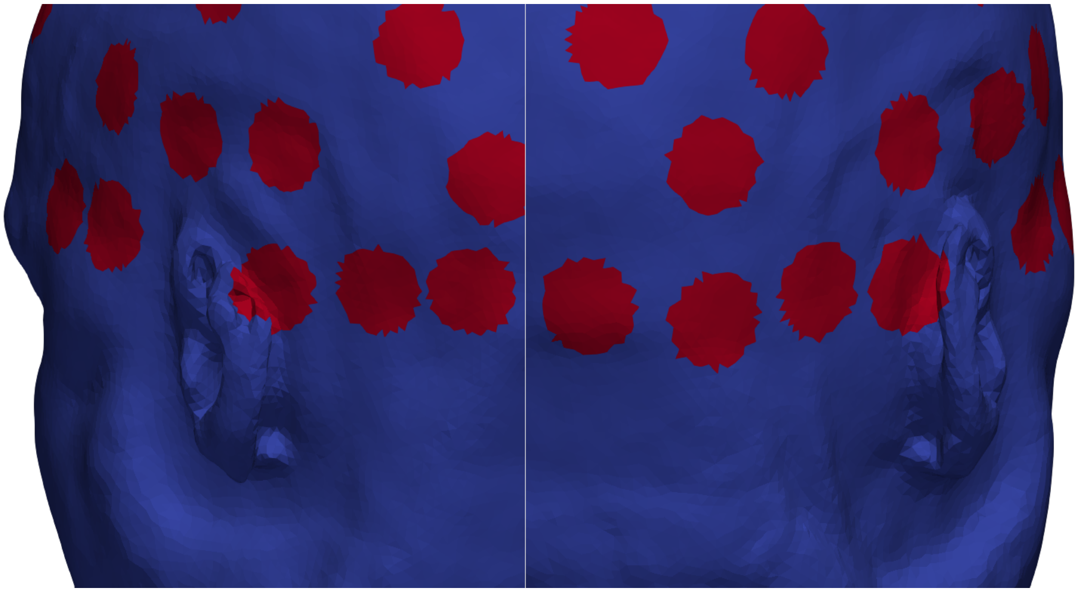

Figure 6.7: This figure shows the electrode interfaces close and at the ears for the montage with 57 electrodes for the realistic head model. We see that the electrodes behind the ears also include boundary faces of the ear.

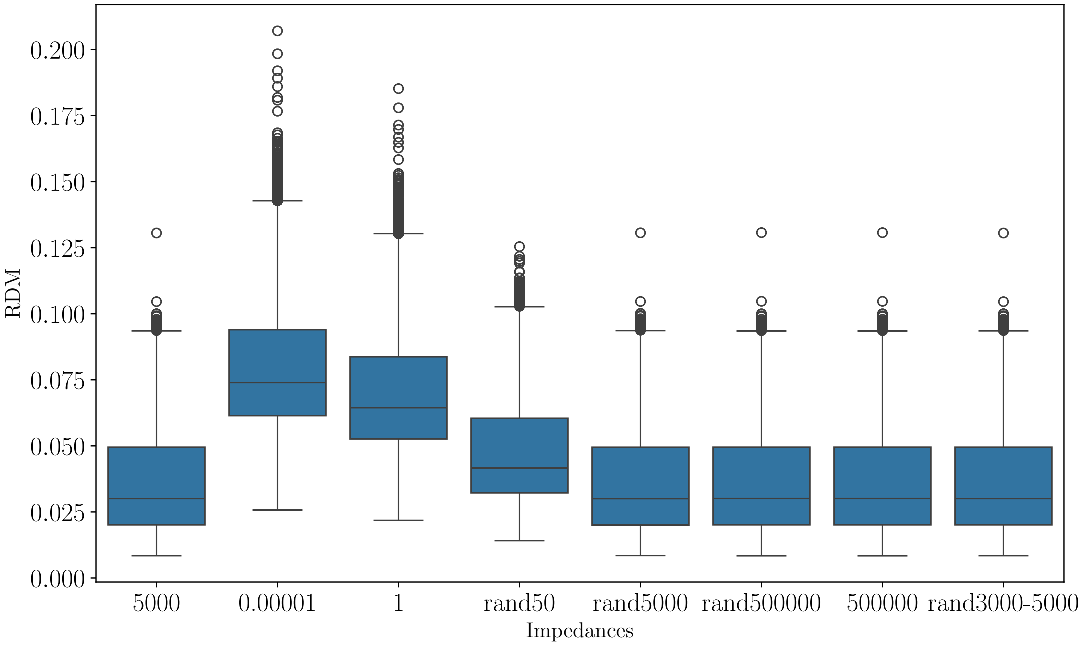

Figure 6.8: RDM of the PEM and the CEM (reference model) for the 143949 dipoles and without the two electrodes that had faces of the ear in their interface. The radius for the remaining 55 electrodes are 10 mm and the simulation is done for various impedance files.

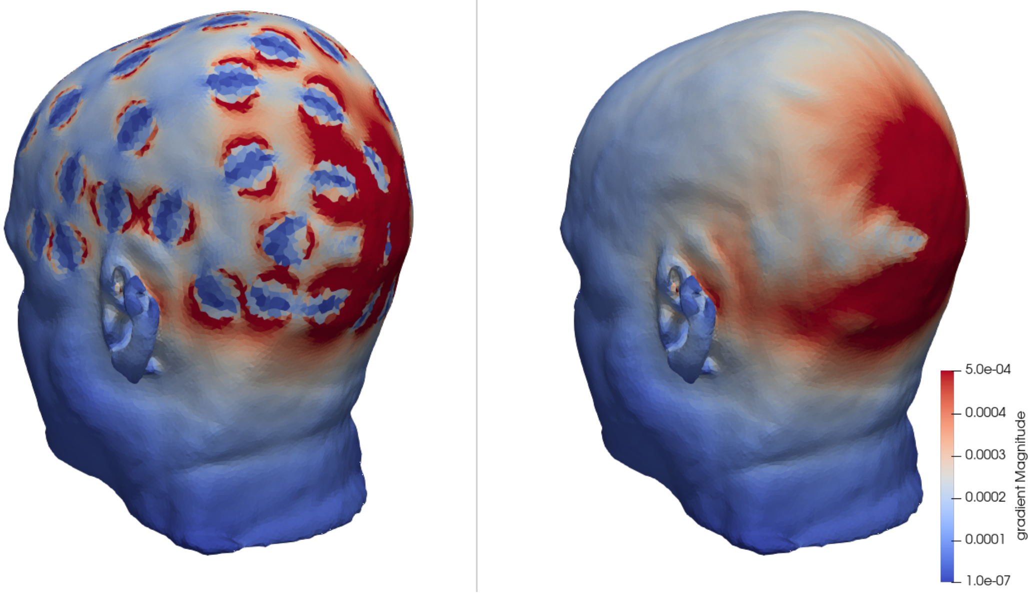

Figure 6.9: This figure shows the magnitude of the gradient for the impedance files *0.00001* (left) and *5000* (right).

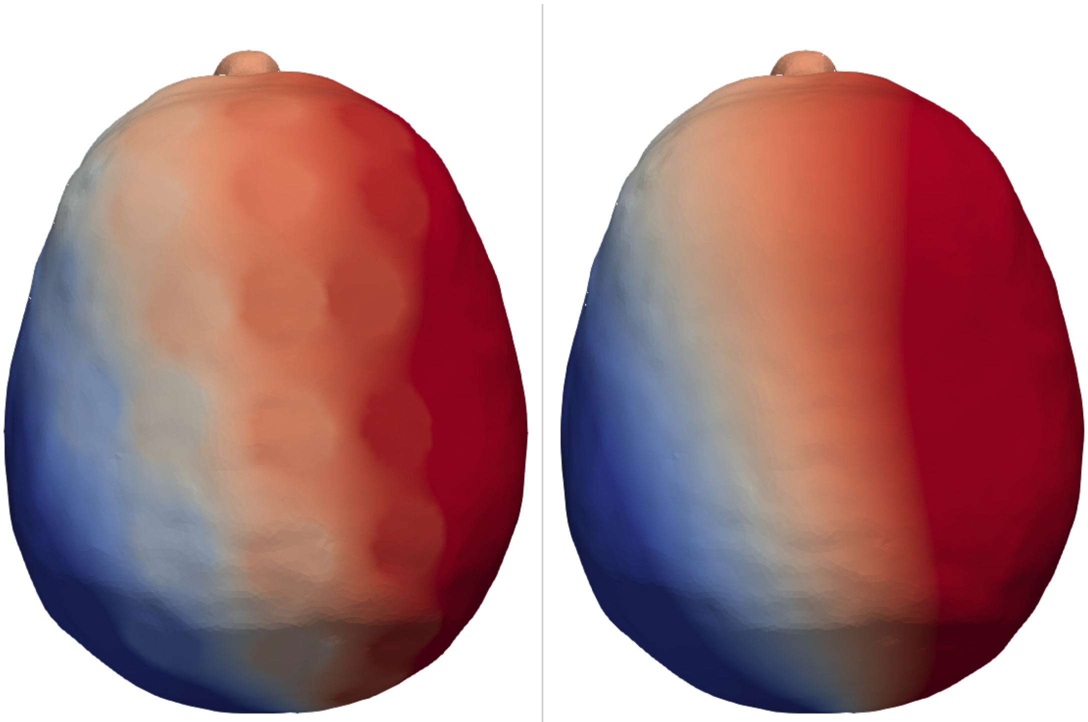

Figure 6.10: This figure shows the potential distribution for the impedance files *0.00001* (left) and *5000* (right). Red colored are the positive values and blue colored are the negative values.

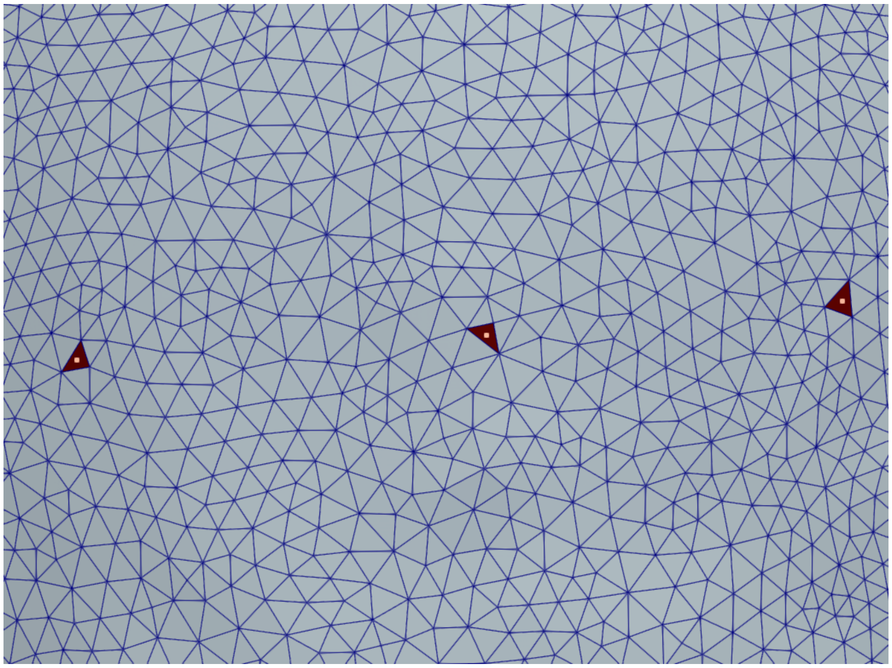

Figure 6.11: Three electrode interfaces are seen which are darker colored on the boundary of the mesh with visible edges. The electrode interfaces consist of single faces and the lighter points in these electrode interfaces show the projected point electrodes. Thus, the PEM takes the potential values at these coordinates.

Impedance files	*5000*	*0.00001*	*1*	*rand50*	*500000*
Mean error values for 143949 dipoles					
RE	$1.6 \cdot 10^{-5}$	0.003028	0.002909	0.001666	0.0
RDM	$1.5 \cdot 10^{-5}$	0.002858	0.002746	0.001574	0.0
MAG	0.999996	0.999186	0.999216	0.999568	1.0
Median error values for 143949 dipoles					
RE	$1.6 \cdot 10^{-5}$	0.002898	0.002787	0.001604	0.0
RDM	$1.5 \cdot 10^{-5}$	0.0027	0.002597	0.001499	0.0
MAG	0.999996	0.999188	0.999219	0.999566	1.0

Table 6.4: Mean and median values of the error measures for 143949 dipoles for PEM and CEM (reference model) for various impedance files and single faces as the electrode interfaces

We see the mean and median error values in table 6.4 and see that these values decrease even more with electrodes that have a single face as the electrode interface compared to the case of larger electrodes. With increasing ACIs, the errors converge to zero also in the numerical setting. It is important and interesting to point out that for these electrode interfaces, the error for the very low impedances also decreased considerably.

6.3 tES

The principle of reciprocity gives us the possibility to perform error investigations for the EEG forward problem and derive from these simulations the errors for the tES. However, current standard two-patch tES is commonly done with two electrodes whose area of the interfaces are between 25 and 35 cm^2 ([24], chapter 1). We thus also feel the necessity to do simulations with an electrode configuration that is suitable for tES.

We do this with *realisticMesh* and use as the target source the same dipolar source that is used in ([20], chapter 4.3) which is used for the analysis of somatosensory evoked responses.

We choose the electrodes for the stimulation for PEM - the anode and cathode - by calculating the potentials for the point electrodes and taking the electrodes with the maximum and minimum potential value as the anode and cathode respectively.

For the CEM we want to do the same, but since the placed electrodes effect the whole potential in the head and especially in the skin compartment close to the electrodes (see [37]), all the possible electrode pairs for the stimulation have to be set for the CEM and the simulated potential values by the electrode have to be calculated for each possible pair. The radius of the electrodes is set to 3 cm, which gives an area of $\approx$ 28.27 cm^2. This is done for all electrode pairs whose centers have a distance that is large enough so that no overlaps of the electrode interfaces occur. This leads to approximately 1300 pairs of electrodes. With the increased radius, unrealistically set electrode interfaces can appear again, so this has to be paid attention to. After the calculated potential values for the pairs of electrodes, the pair with the largest potential difference is chosen to be the pair which is used for the stimulation. This is done for the two impedance files *5000* and *0.00001* to see if very low impedances also effect the choice of stimulation electrodes.

The results show that the simulations give the maximal potential difference for the PEM as 1.2121, for the CEM with the impedance file *5000* as 1.1697 and for the CEM with the impedance file *0.00001* as 1.143 rounded to four decimal places.

For all three cases, the same electrode pair is chosen for the stimulation that is visualized in figure 6.12 and the corresponding potential in figure 6.13. This shows that the CEM may also not make a considerable difference in the choice of two stimulating electrodes with a larger radius even with unrealistically low impedances.

6.4 iEEG Forward Problem

There is interest in the EEG forward problem while using depth electrodes, so in the iEEG forward problem. In general, it is difficult methodologically to find current sources, which are deeper in the brain. For this scenario, depth electrodes are advantageous since they can be placed close to the regions of interest in the brain. We also want to simulate

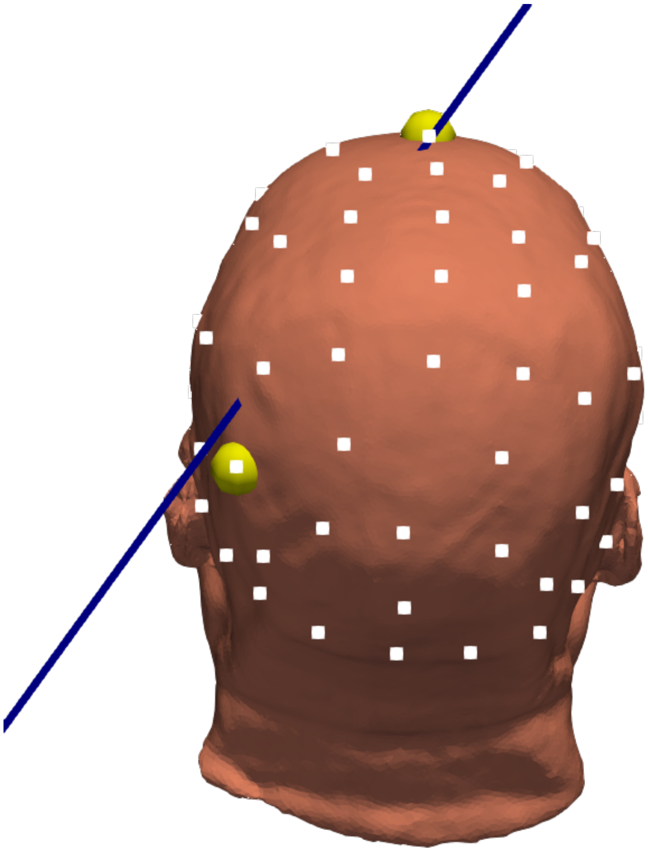

Figure 6.12: This figure shows the chosen pair for the stimulation for all three cases (PEM, CEM with *5000*, and CEM with *0.00001*). This pair is yellow colored. The coordinates of the electrodes are white. The dark blue line goes through the dipole position and has the direction of the dipole moment. It is visible that the chosen pair that is the closest to the intersection of this line and the boundary of the head is also chosen to be the stimulating pair from the simulation results.

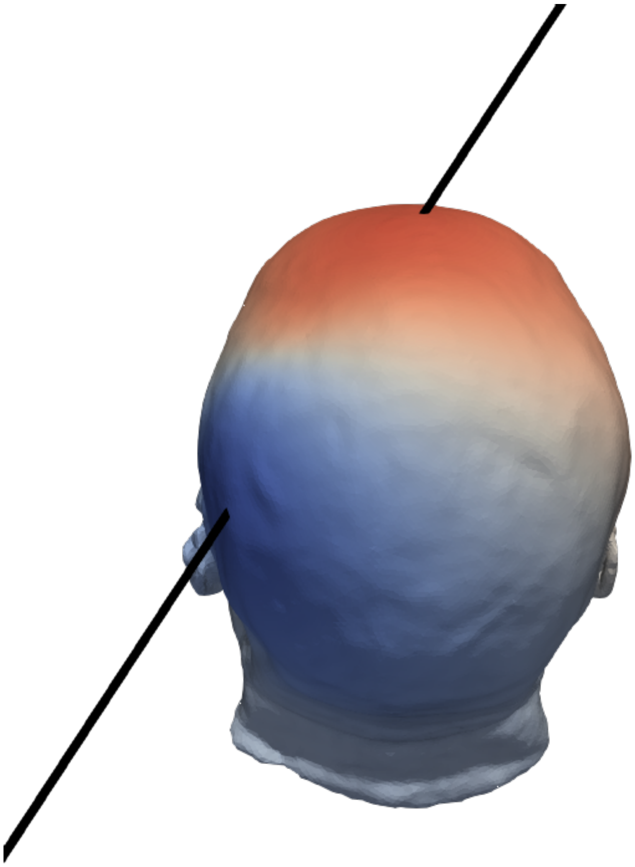

Figure 6.13: This figure shows the potential for the PEM on the boundary of the head. The black line again goes through the dipole position and has the direction of the dipole moment. It is visible that the line intersects the boundary of the head close to the minimal and maximal potential where also the pair of electrodes is the closest to.

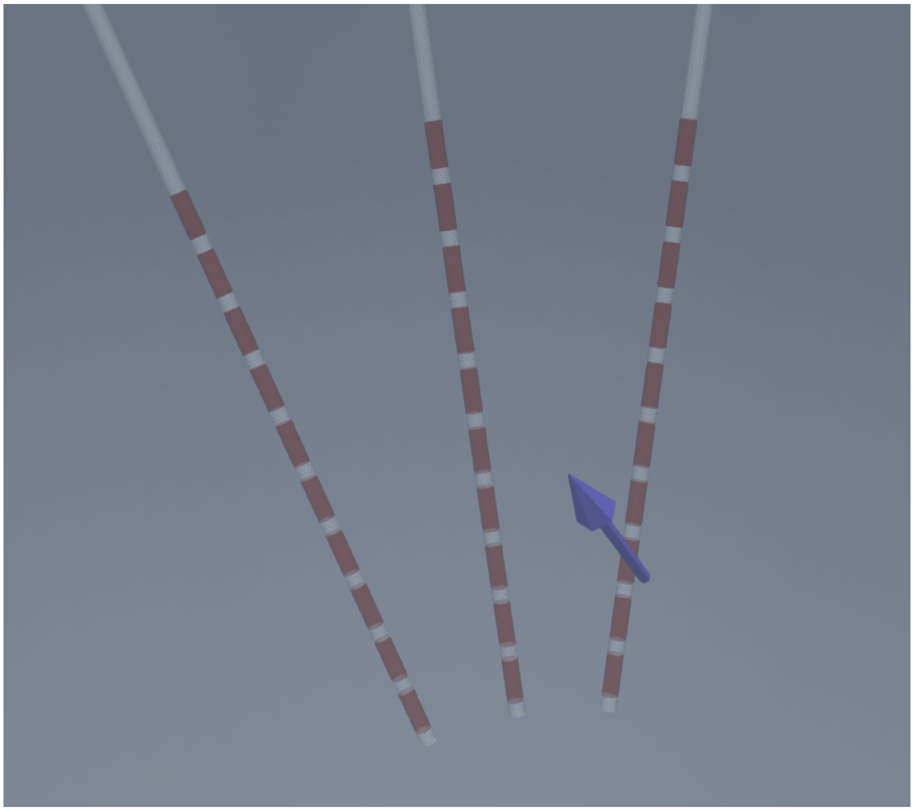

Figure 6.14: This figure shows a dipole with the moment $(\frac{1}{\sqrt{3}}, \frac{1}{\sqrt{3}}, \frac{1}{\sqrt{3}})$ (blue arrow) that is placed in a distance of 3 mm away from an electrode contact. The length of the arrow does not stay in a relation to the dipole strength.

this scenario, so we construct dipole sources close to the electrode interfaces of the depth electrodes and compare CEM with PEM.

The ACIs are randomly generated as float numbers between 500 and 1500 Ω (this is a realistic range according to [5]) with the `numpy.random.rand()` method and this impedance file is called *rand500-1500*. We will again also use the impedance file *0.00001* for an interesting comparison with PEM.

Here, we create dipoles in the following way (see figure 6.14): We have three depth electrodes. These are modeled as cylinders with a starting point and a direction. We calculate two orthonormal vectors to the depth electrodes and place dipoles 3.43 mm away from the electrode centers and in the orthonormal directions. The reason for choosing 3.43 mm is the radius of the cylinder, which is 0.43 mm and an additional distance of 3 mm from the electrode interface. For each dipole position, we have the moment $(\frac{1}{\sqrt{3}}, \frac{1}{\sqrt{3}}, \frac{1}{\sqrt{3}})$ and thus have 60 dipoles. One of such dipoles is visualized in figure 6.14. We take this moment, because the moments $(1, 0, 0)$, $(0, 1, 0)$ and $(0, 0, 1)$ cause that the planes that are perpendicular to the dipoles contain in two cases either three or all 30 contacts and thus have potential values that are zero for PEM and close to zero for CEM. This causes that the error measures are not stable anymore because of the very small values in the denominators for the error measures in 6.1. We can see the error values for the PEM and

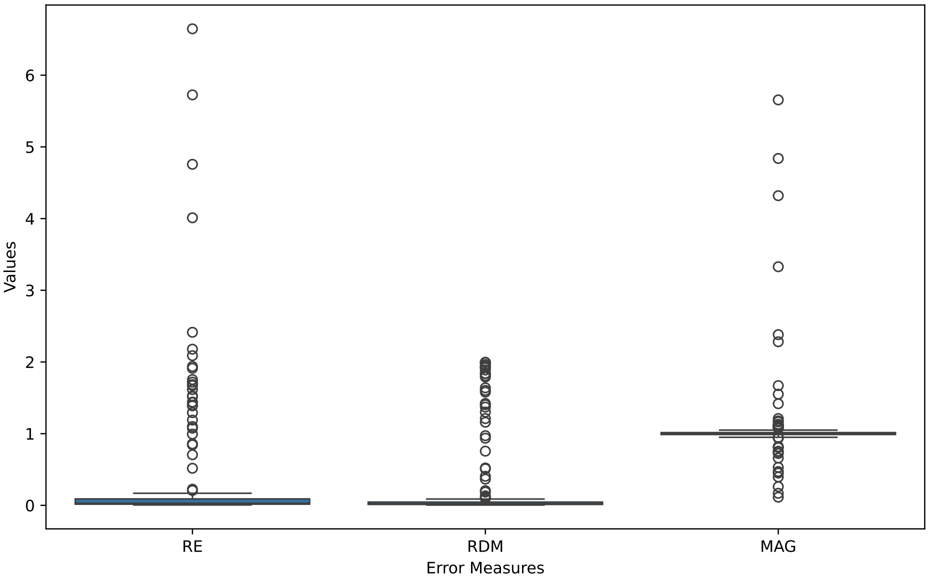

Figure 6.15: This figure shows the error values for the 180 dipoles that have the moment $(1, 0, 0)$, $(0, 1, 0)$ or $(0, 0, 1)$ in the iEEG simulation using the CEM with realistic impedances. We see that some outliers have very large errors.

the CEM as the reference in figure 6.15 and see considerable outliers for these 180 dipoles with very large error values.
For the 60 dipoles with the moment $(\frac{1}{\sqrt{3}}, \frac{1}{\sqrt{3}}, \frac{1}{\sqrt{3}})$ the mean and median values of the error measures are shown in table 6.5 for the cases of making the comparison on all 30 electrode contacts and on $2 - 3$ electrode contacts that are the closest to the corresponding dipole position. We can see that the errors are very small and that even the closest electrode contacts to the dipoles show small errors for realistic impedances.

6.5 DBS

We implemented a way of using the CEM for DBS electrodes. Here, we are stimulating by injecting a current into the brain through depth electrodes that are placed in the head of the patient. The two meshes, we have, are: *sphere_DBS* and *sphere_DBS_PEM*.
We use two different choices of stimulation and start with the more realistic one, where the stimulating electrodes are on the same depth electrode and placed right next to each other. The applied current is $+1$ mA and -1 mA. While 2 electrodes stimulate, the other 28 electrodes are used to measure. So, the computed potentials that are measured by the stimulating electrodes were left out of the comparison since the measured potentials by these electrodes could differ considerably, because of the Dirac function for the stimulation with PEM.
All error values are attained by taking the PEM and the CEM as the reference model.

Impedance files	*rand500-1500*	*0.00001*
Mean error values for 60 dipoles over all electrode contacts		
RE	0.0312	0.1322
RDM	0.0197	0661
MAG	1.0217	1.1098
Median error values for 60 dipoles over all electrode contacts		
RE	0.0144	0.1044
RDM	0.0125	0.0645
MAG	1.0072	1.0811
Mean error values for 60 dipoles over the closest $2-3$ electrode contacts		
RE	0.0322	0.1405
RDM	0.0151	0.0483
MAG	1.0255	1.1275
Median error values for 60 dipoles over the closest $2-3$ electrode contacts		
RE	0.0161	0.1135
RDM	0.013	0.05
MAG	1.0092	1.0993

Table 6.5: This table shows the mean and median values of the error measures for the iEEG forward model with PEM and CEM as the reference model with 60 dipoles for different sets of measured potential values and two impedance files. The first set is over all 30 electrode contacts and the second set is over the two to three electrode contacts that are the closest to the dipole.

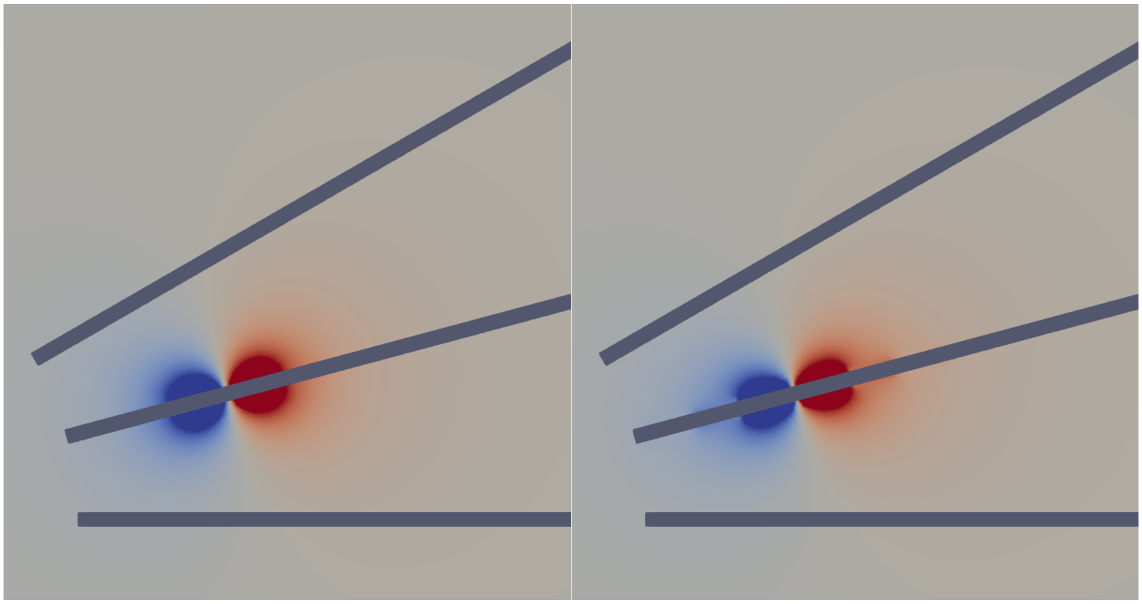

Figure 6.16: In this figure the potential distribution with CEM and the impedance files *rand500-1500* (left) and *0.00001* (right) is shown for DBS with two stimulating electrode contacts.

For the realistic impedance file with ACIs between 500 and 1500 Ω the RE is 0.0555, the RDM is 0.0199, and the MAG is 0.948. Here, we see that the incorporation of the CEM leads to a slightly higher error value for RE even for realistically set paramaters.
For the impedance file *0.00001* the RE is 0.0772, the RDM is 0.0486, and the MAG is 0.9389.
In figure 6.16 we can see the potential distribution for the DBS with CEM and two different impedance files *rand500-1500* and *0.00001*. We see how the electrode interfaces effect the potential with the impedance file *0.00001*. In figure 6.17 we see the magnitude of the gradient for the same comparison and see the effect of the electrode interfaces strongly for *0.00001*, but also slightly for the realistic values in *rand500-1500*.
We can see in figure 6.18 the comparison of the magnitude of the gradient for the PEM case and the CEM with *rand500-1500* for stimulating contacts that are maximally far away from each other over the three depth electrodes. So, the stimulation is done by two contacts that are on two depth electrodes that are the most distant to each other. On one depth electrode the stimulating contact is chosen to be the last one and for the other depth electrode, the stimulating contact is the first one. We can see this by looking approximately at the centers of the red patches in figure 6.18. Here, the RE is 0.0306, the RDM is 0.0169, and the MAG is 0.9743.

6.6 Epicranial Application of Stimulation Electrodes

In optimizing brain stimulation, different methods and considerations are possible. When we stimulate non-surgically, we have electrodes that are placed on the patients head. Commonly, those electrodes are placed on the skin or the hair of the patient. However, if the

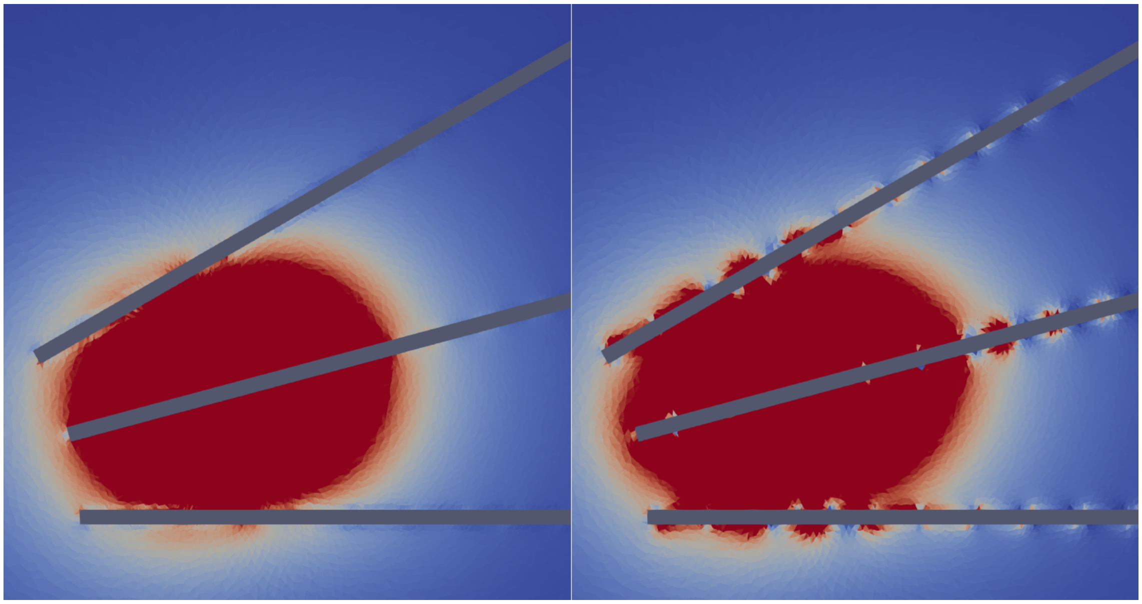

Figure 6.17: In this figure the magnitude of the gradient with CEM and the impedance files *rand500-1500* (left) and *0.00001* (right) is shown for DBS with two stimulating electrode contacts.

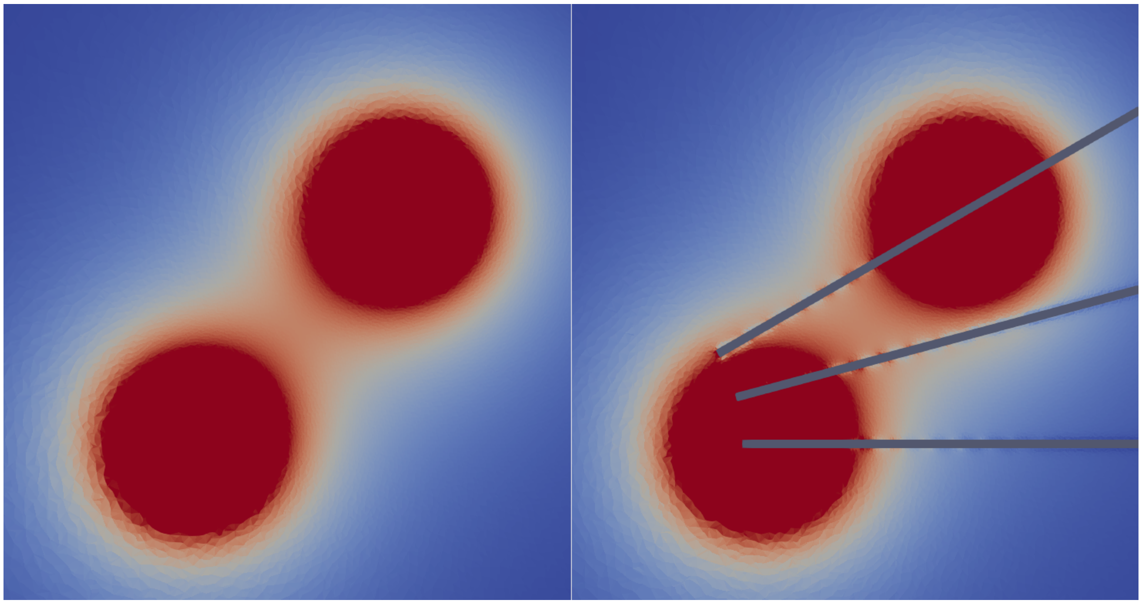

Figure 6.18: In this figure the magnitude of the gradient with PEM (left) and CEM with the impedance file *rand500-1500* (right) is shown for DBS with two stimulating electrodes that are maximally far away from each other.

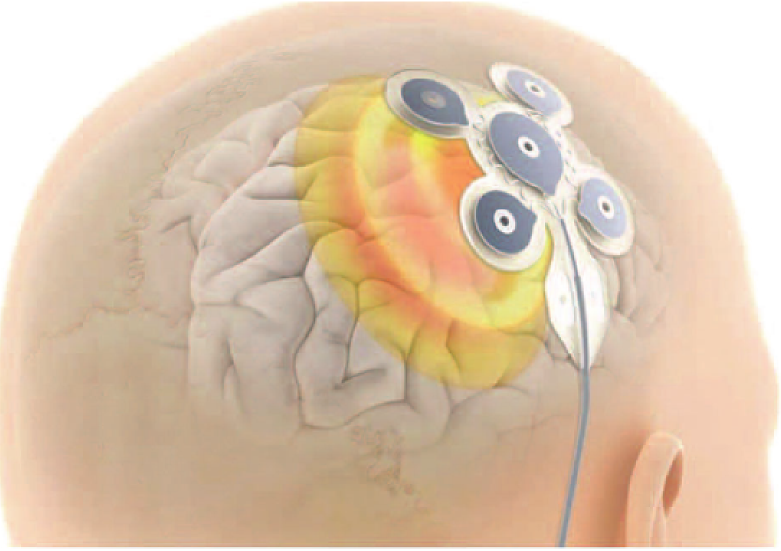

Figure 6.19: This figure shows the EASEE system [48].

stimulating electrodes are placed close to each other, this leads to the disadvantageous case of a high amount of current flowing through the skin from the anode to the cathode and much less flowing through the low conducting skull into the brain regions which are meant to be stimulated. Additionally, this procedure can be experienced as painful for some patients. The company *EASEE* [48] circumvents these problems by intervening minimally - compared to other invasive methods - and placing the stimulating electrodes permanently and directly on the skull. This company offers stimulation to patients with drug-refractory epilepsy where the epileptogenic zone is meant to be stimulated. In ([49], figure 2(B)) it was shown that 6 out of 26 patients who have received stimulation for two years have become seizure-free. For this, the anode and four cathodes (see figure 6.19) are placed close to the epileptogenic zone. For a precise calculation of the electrode placement for optimal stimulation of the epileptogenic zone, the CEM offers an advantageous electrode model. We created two meshes with *Gmsh* where the electrode interfaces are already part of the mesh and labeled as the corresponding electrodes. For the first mesh, the electrodes are placed directly on the skull like in the *EASEE*-system and for the second mesh, the electrodes are placed on the skin. We can see this in 6.20. With the implemented electrode projection *predefined_electrodes* we set the electrode interfaces and have the injection pattern of 4 mA for the anode and -1 mA for the four cathodes.
Figure 6.20 shows that the current reaches deeper into the head and brain in the case of electrodes placed directly on the skull with the CEM. This offers a very interesting field where the benefits and advantages of CEM can be investigated.

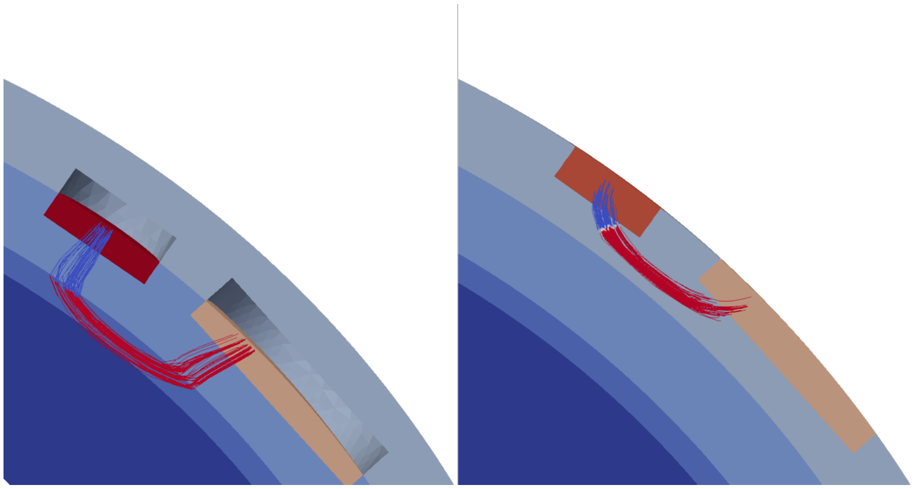

Figure 6.20: In this figure we see a tES with the the EASEE system (left) and with the electrodes placed on the skin (right). In both cases, the CEM is used as the electrode model. We see how the applied current reaches deeper into the head and even reaches the CSF (thinnest compartment) and brain compartment (dark blue) with the EASEE system.

Chapter 7

Discussion

This thesis presented the analysis, evaluation, and implementation within the DUNEuro framework [47] of the CEM for the modalities EEG, tES, iEEG, and DBS. The CEM was successfully integrated into the FEM solver and extended to support the local subtraction source model, the transfer matrix, and the Schur complement approach.

On an analytical level, the convergence of CEM to PEM for the radius r going to zero (chapter A.1) was shown as well as in the FEM setting (chapter 4.6) and also in a numerical simulation (chapter 6.2.2) which shows that the PEM is the limit of the CEM for $r \to 0$.

Through extensive numerical experiments in both spherical (for all modalities) and realistic head models (for EEG and tES), the impact of electrode radius, contact impedance, and electrode placement was investigated. It was shown that the difference between CEM and PEM increases with larger electrodes and lower contact impedances, particularly for radial dipoles with high eccentricities. These results hold with [37].

The implementation and investigation of the CEM for iEEG and DBS applications is a new contribution of this thesis and the effect of the CEM still needs to be evaluated with error metrics that are appropriate for small signals and in various scenarios.

Incorporating more realistic head models with higher resolution (if feasible in the future), layered skull compartments (as in [37]), and anisotropic conductivity, to better assess the full benefits of the CEM are still to be done.

There are several known simplifications and potential sources of error in forward modeling simulations. These include the use of dipole models for current sources, limited mesh resolution, numerical discretization errors, and tissue conductivity variability, inhomogeneity and anisotropy. Also, inaccuracies may arise from the positioning of the electrodes and variations in the application of conductive gel. It is difficult to answer at which point the error introduced by the PEM becomes significant enough compared to the other error sources to justify the necessity of using the more complex CEM.

One can ask whether large electrode areas in tES (25–35 cm^2) can cause different choices of electrode pairs for stimulation between PEM and CEM. This question was only investigated for one specific dipole and remains open for further study.

In this thesis, only the continuous Galerkin method was used. However, in certain situations such as skull leakages [8][56] for low-resolution meshes the discontinuous Galerkin method might be an interesting alternative. A comparison between continuous and discontinuous Galerkin methods using the CEM could be an interesting extension, both in high- and low-resolution settings.

The use of p-FEM and higher-order basis functions (see [17][36]) may improve the accuracy of the solution in these settings. Also, modeling electrodes as circular interfaces and employing methods such as cut-FEM [9] could lead to even more geometrically realistic electrode representations.

With the development of methods to decrease the ECIs, the CEM could become an increasingly attractive option and also in new emerging methods and scenarios, such as the EASEE-system [48][49].

Chapter 8

Conclusion

By including the electrode interface and the ECIs, the CEM produces more realistic results without introducing excessive computational cost. The CEM is easy to use and incorporate by simply changing the flags and giving in the radius and the ACIs and overall, the implementation of the CEM extends the modeling capabilities for realistic bioelectromagnetic simulations in DUNEuro.

This thesis showed that despite the increased realism of the CEM, the PEM remains a valid and efficient simplification in many practical cases including the simulations we conducted with iEEG and DBS, especially when electrodes are small and impedances are high. The occuring errors are larger for radial dipoles with high eccentricities.

As seen in the case of epicranial stimulation (chapter 6.6), new clinical or experimental setups may emerge in which the CEM is not just beneficial, but can be essential. In these scenarios improved realism of CEM could support better therapies that are based on stimulation.

Outlook

For future developments in the field of bioelectromagnetism the effects of CEM should be investigated and therefore for future research, it is highly valuable to have the CEM as a realistic, robust and easy-to-use electrode model within a simulation framework such as DUNEuro.

Currently, the implementation does not give warnings for overlapping electrode interfaces, which can lead to larger errors - especially with lower impedances - in the computed potentials. Future versions should include automated checks. When using the CEM, it should also be verified that electrodes do not intersect non-physical surfaces such as the ears. It could be useful to define boundary faces that are excluded from serving as electrode interface candidates. The user of the CEM could also benefit from warnings when an electrode interface has a value for the area that is not within a realistic interval depending on the mesh resolution.

Future work may include comparisons with discontinuous Galerkin methods, exploration of anisotropic conductivity effects, and – if technically feasible – the inclusion of spatially varying impedance distributions to extend the electrode model even further for the case that the impedance varies over the electrode interface.

The effect of the CEM in combined EEG and MEG like it can be used for the estimation of the epileptogenic zone (see [31]) is also an interesting direction for the research with CEM.

Appendix A

Appendix

A.1 Analytical Convergence of CEM to PEM in the EEG Forward Problem with fixed Impedances and Radius $r \to 0$

In [12] and [19] there is the proof for tES, more precisely the TDCS case for the convergence of the CEM to PEM for $r \to 0$ for fixed impedances. It says that for a domain $\Omega_0 \subset \Omega$ with $\overline{\Omega_0} \subset \Omega$ there exists $r_0 > 0$ and $C > 0$ with

$$\|u^r - u\|_{H^1(\Omega_0)/\mathbb{R}} \leq Cr^2|I| \tag{A.1}$$

for $0 < r < r_0$ and $I \in \mathbb{R}^L$. Here, $H^1(\Omega_0)/\mathbb{R}\cdot 1$ is the quotient of the Sobolev space $H^1(\Omega_0)$ by the space of constant functions, which is isomorphic to $H_\star(\Omega_0)$. Here, the convergence was shown for potentials that are defined up to a constant.

To understand this in full detail, I recommend [12] and [19].

We also want to show the convergence for the EEG forward problem and will use the principle of reciprocity which we have also proven for the CEM case. For this, we follow [22].

We denote the solution of the EEG forward problem for a dipole at position x_0 with moment M by u for the PEM and by (u^r, U^r) for the CEM with radius $r \in \mathbb{R}_+$.

We will take the first electrode as the reference electrode. Let us have the current injection with the first electrode being the anode, so $I_1 = 1$ and the j-th electrode being the cathode, so $I_j = -1$. For this current injection pattern, we denote the solutions of the tES problem for the CEM with radius r by $u_{i,1}^{\text{CEM, tES},r}$ and with the PEM by $u_{i,1}^{\text{PEM, tES}}$ respectively.

Since the principle of reciprocity holds for both electrode models, we have:

$$\begin{aligned} \langle M, \nabla u_{i,1}^{\text{CEM, tES},r}(x_0)\rangle &= U_i^r - U_1^r \\ \langle M, \nabla u_{i,1}^{\text{PEM, tES}}(x_0)\rangle &= u(p_i) - u(p_1). \end{aligned}$$

So, we have

$$|(U_i^r - U_1^r) - (u(p_i) - u(p_1))| = |\langle M, \nabla u_{i,1}^{\text{CEM, tES},r}(x_0)\rangle - \langle M, \nabla u_{i,1}^{\text{PEM, tES}}(x_0)\rangle|$$

$$= |\langle M, \nabla u_{i,1}^{\text{CEM, tES},r}(x_0) - \nabla u_{i,1}^{\text{PEM, tES}}(x_0)\rangle| \leq \|M\|_2 \cdot \|\nabla(u_{i,1}^{\text{CEM, tES},r} - u_{i,1}^{\text{PEM, tES}})(x_0)\|_2$$

by the Cauchy-Schwarz inequality.
Here, we take an $\epsilon > 0$, such that on the ball around x_0 with radius ϵ, called $B_\epsilon(x_0)$ the conductivity tensor σ is smooth and for an arbitrary constant $C_1 \in \mathbb{R}$, we have

$$\|M\|_2 \cdot \|\nabla(u_{i,1}^{\text{CEM, tES},r} - u_{i,1}^{\text{PEM, tES}})(x_0)\|_2 \leq \|M\|_2 \cdot \|u_{i,1}^{\text{CEM, tES},r} - u_{i,1}^{\text{PEM, tES}} - C_1\|_{C^1(B_\epsilon(x_0))}$$

by the definition of the norm on $C^1(B_\epsilon(x_0))$.
With elliptic regularity and the fact that on the ball we have

$$\nabla \cdot (\sigma \nabla(u_{i,1}^{\text{CEM, tES},r} - u_{i,1}^{\text{PEM, tES}} - C_1)) = 0$$

we can deduce that the function $u_{i,1}^{\text{CEM, tES},r} - u_{i,1}^{\text{PEM, tES}} - C_1$ is smooth on the ball $B_\epsilon(x_0)$ (see [10], theorem 6.3.1.). Here, it plays a role that σ is smooth on the ball $B_\epsilon(x_0)$.
We want to bring these estimations back to the Sobolev norm and can deduce (after potentially shrinking the radius ϵ of the ball that $u_{i,1}^{\text{CEM, tES},r} - u_{i,1}^{\text{PEM, tES}} - C_1 \in H^s(B_\epsilon(x_0))$ for an $s \in \mathbb{R}$. Using Sobolev inequalities, we have for a suitably large s that

$$\|u_{i,1}^{\text{CEM, tES},r} - u_{i,1}^{\text{PEM, tES}} - C_1\|_{C^1(B_\epsilon(x_0))} \leq C_2 \cdot \|u_{i,1}^{\text{CEM, tES},r} - u_{i,1}^{\text{PEM, tES}} - C_1\|_{H^s(B_\epsilon(x_0))}$$

with a suitable constant $C_2 \in \mathbb{R}_+$.
Let $\tilde{u} = (u(p_1), ..., u(p_L))^T$ be the vector with the given potentials with the PEM. We also have, by the definition of the quotient norm, that

$$\|U^r - \tilde{u}\|_{\mathbb{R}^L/\mathbb{R}\cdot 1} \leq \|(U^r - \tilde{u}) - ((U_1^r - u(p_1)), ..., (U_1^r - u(p_1)))\|_2.$$

and the following estimation holds

$$\|(U^r - \tilde{u}) - ((U_1^r - u(p_1)), ..., (U_1^r - u(p_1)))\|_2 \leq (L-1) \max_{2 \leq i \leq L} |(U_i^r - U_1^r) - (u(p_i) - u(p_1))|$$

So far, we have

$$\|U^r - \tilde{u}\|_{\mathbb{R}^L/\mathbb{R}\cdot 1} \leq (L-1) \max_{2 \leq i \leq L} |(U_i^r - U_1^r) - (u(p_i) - u(p_1))|$$

$$\leq (L-1) \cdot \|M\|_2 \cdot \|u_{i,1}^{\text{CEM, tES},r} - u_{i,1}^{\text{PEM, tES}} - C_1\|_{H^s(B_\epsilon(x_0))}$$

Since $C_1 \in \mathbb{R}$ is chosen arbitrarily, we also have

$$\|U^r - \tilde{u}\|_{\mathbb{R}^L/\mathbb{R}\cdot 1} \leq (L-1) \cdot \|M\|_2 \cdot \max_{2 \leq i \leq L} \|u_{i,1}^{\text{CEM, tES},r} - u_{i,1}^{\text{PEM, tES}}\|_{H^s(B_\epsilon(x_0))/\mathbb{R}\cdot 1}$$

We can deduce that for a suitable constant $C_3 \in \mathbb{R}_+$ and $\epsilon_0 < \epsilon$

$$\|u_{i,1}^{\text{CEM, tES},r} - u_{i,1}^{\text{PEM, tES}}\|_{H^s(B_\epsilon(x_0))/\mathbb{R}\cdot 1} \leq C_3 \cdot \|u_{i,1}^{\text{CEM, tES},r} - u_{i,1}^{\text{PEM, tES}}\|_{H^1(B_{\epsilon_0}(x_0))/\mathbb{R}\cdot 1}$$

holds (see [12], lemma 9). In total, we have

$$\|U^r - \tilde{u}\|_{\mathbb{R}^L/\mathbb{R}\cdot 1} \leq (L-1) \cdot C_3 \cdot \|M\|_2 \cdot \max_{2 \leq i \leq L} \|u_{i,1}^{\text{CEM, tES},r} - u_{i,1}^{\text{PEM, tES}}\|_{H^1(B_{\epsilon_0}(x_0))/\mathbb{R}\cdot 1}$$

$$\leq (L-1) \cdot \|M\|_2 \cdot C_3 \cdot C \cdot r^2$$

by A.1.
This shows the convergence of the CEM to PEM with fixed impedances and $r \to 0$.

A.2 Convergence of CEM to PEM in the FEM Setting

We have seen in A.1 that the CEM converges to the PEM analytically for the radius $r \to 0$. It is important to note that the condition that the impedances go to infinity is not necessary for the convergence of the CEM to PEM (see Appendix A.1), but the effect that the electrodes do not effect the potential distribution in the head can be attained by $Z_l \to \infty$.
The proof of the convergence in the FEM-setting has been worked out in corporation with the doctoral student Malte Höltershinken and is presented here:
To also have the convergence in the numerical computations, we set the radius of the electrode small enough. We work with tetrahedral meshes of 1 mm resolution and before finding the right mesh face which represents the electrode interface, we choose the closest center of the boundary faces to represent the center of the electrode. From this center of the face, the distance to the other boundary faces are calculated with the electrode projection `cem_radial` and if they are smaller than the radius r, the intersection is added to the electrode interface. So with every radius $r \neq 0$ the intersection whose center represents the center of the electrode is at least in the electrode interface. By choosing r small enough, we guarantee that the electrode interface e_l consists of only one boundary face.
In the PEM in DUNEuro we enter the codimension as a flag. It decides what dimension the entity has to which the global coordinate of the electrode gets projected. Let $c \in \mathbb{N}_0$ be the codimension we choose. Then the dimension of the entity is $3 - c$. In our simulations we always chose $c = 3$, so the electrodes were projected to a node.
To show a convergence, we instead want the electrode in the PEM case to be projected to the closest center of a boundary face, so the codimension was set to 1.
Now, we want to show why the CEM converges to PEM in this numerical setting:
We look at the FEM for CEM in the matrix form:

$$\begin{pmatrix} A & B \\ B^T & C \end{pmatrix} \begin{pmatrix} u \\ U \end{pmatrix} = \begin{pmatrix} x \\ y \end{pmatrix}$$

as is in 4.5 and at the measured potential vector

$$U = (C - B^T A^{-1} B)^{-1} y - (C - B^T A^{-1} B)^{-1} B^T A^{-1} x.$$

For simplicity we assume that the patch for the local subtraction approach does not grow into the electrode interfaces in which case $y = 0$ and we get

$$U = -(C - B^T A^{-1} B)^{-1} B^T A^{-1} x.$$

To simplify the calculations we further assume $Z_1 = ... = Z_L = \lambda$ and denote the matrices A, B and C with this $\lambda > 0$ as the impedances by A_λ, B_λ and C_λ. It is clear that

$B_\lambda = \lambda^{-1}B_1$ and $C_\lambda = \lambda^{-1}C_1$ with $\lambda^{-1} := \operatorname{diag}(\lambda^{-1}, ..., \lambda^{-1})$. So, for U we get

$$U = -(C_\lambda - B_\lambda^T A_\lambda^{-1} B_\lambda)^{-1} B_\lambda^T A_\lambda^{-1} x,$$

and this is

$$U = -(\lambda^{-1}C_1 - \lambda^{-2}B_1^T A_\lambda^{-1} B_1)^{-1} \lambda^{-1} B_1^T A_\lambda^{-1} x.$$

Further calculations give

$$U = -(C_1 - \lambda^{-1}B_1^T A_\lambda^{-1} B_1)^{-1} B_1^T A_\lambda^{-1} x.$$

When we let $\lambda \to \infty$, it follows

$$U = -C_1^{-1} B_1^T A_0^{-1} x$$

and A_0^{-1} is the inverse of the stiffness matrix of the PEM, because the additional sum in 4.6 goes to zero in the limit.

The vector $A_0^{-1}x$ is the solution in the FEM for the PEM, so we will abbreviate it as $s^{\text{PEM}} \in \mathbb{R}^N$. The entries of this vector are the coefficients in the linear combination with the basis vectors of our solution space, so $u^{\text{PEM}} = \sum\limits_{i=1}^{N} s_i^{\text{PEM}} \cdot \varphi_i$ with the basis $\{\varphi_1, ..., \varphi_L\}$ of our solution space. In this thesis, we only worked with linear basis functions, so the basis are the hat functions.

So, we have

$$U = -C_1 B_1^T s^{\text{PEM}}$$

and the l-th entry of $B_1^T s^{\text{PEM}}$ is

$$(B_1^T s^{\text{PEM}})_l = -\sum_{i=1}^{N} (\int\limits_{e_l} \varphi_i \, dS) \cdot s_i^{\text{PEM}} = -\int\limits_{e_l} \underbrace{\sum_{i=1}^{N} \varphi_i \cdot s_i^{\text{PEM}}}_{=u^{\text{PEM}}} \, dS,$$

so we deduce

$$U_l = -(C_1)_l \cdot (-\int\limits_{e_l} u^{\text{PEM}} \, dS) = \frac{\int\limits_{e_l} u^{\text{PEM}} \, dS}{|e_l|}.$$

Because of the codimension of 1, the PEM gives us the value of the potential at the center of the face to whose center the electrode was projected. We want to show that the same value gets attained for the CEM with infinite impedances, so

$$U_l = \frac{\int\limits_{e_l} u^{\text{PEM}} \, dS}{|e_l|} \overset{!}{=} \frac{\sum\limits_{i=1}^{3} u^{\text{PEM}}(p_i)}{3}$$

for $l \in \{1, ..., L\}$ and p_1, p_2, p_3 being the three nodes of the single face of the electrode interface. It is important to point out again that this equality will hold for the solution space with the hat functions as the basis.

First, we want to pull the integral back to an integral over a triangle T in $\mathbb{R}^2$ with the

corners at $(0,0),(0,1)$ and $(1,0)$. e_l consists of a single triangle F. Let μ be an affine map from the reference triangle in $\mathbb{R}^2$ to F. Then the hat functions for the three nodes p_1, p_2, p_3 are denoted by $\varphi_{p_1}, \varphi_{p_2}, \varphi_{p_3}$ and can be mapped to the hat functions $\tilde{\varphi}_{p_1}, \tilde{\varphi}_{p_2}, \tilde{\varphi}_{p_3}$ by μ.
We see that

$$C \int\limits_T u^{\mathrm{PEM}}(\mu(x))\, dS = \int\limits_{e_l} u^{\mathrm{PEM}}(x)\, dS$$

with the transformation theorem (see [11], chapter 14) and with $C = \sqrt{\det(J_\mu^T \cdot J_\mu)}$ and J_μ being the Jacobian matrix. Here, C is constant, because μ is an affine linear map.
If we replace the left- and the right-hand side with the hat functions, we have

$$C \cdot \sum_{i=1}^{3} (s_i^{\mathrm{PEM}} \cdot \int\limits_T \tilde{\varphi}_{p_i}\, dS) = \sum_{i=1}^{3} (s_i^{\mathrm{PEM}} \cdot \int\limits_{e_l} \varphi_{p_i}\, dS)$$

If we have our coordinates x_1, x_2 in $\mathbb{R}^2$, then the hat functions are

$$\tilde{\varphi}_{p_1}(x_1,x_2) = x_1, \quad \tilde{\varphi}_{p_2}(x_1,x_2) = x_2, \quad \tilde{\varphi}_{p_3}(x_1,x_2) = 1 - x_1 - x_2.$$

We integrate over T and use the theorem of Fubini (see ([11], chapter 7, theorem 2)) to get

$$\int\limits_T \tilde{\varphi}_{p_1}(x_1,x_2)\, dS = \int\limits_0^1 \int\limits_0^{1-x_2} x_1\, dx_1\, dx_2 = \int\limits_0^1 \frac{(1-x_2)^2}{2}\, dx_2 = \left[-\frac{(1-x_2)^3}{6} \right]_0^1 = \frac{1}{6}.$$

Similarly, we calculate this for $\tilde{\varphi}_{p_2}$ and $\tilde{\varphi}_{p_3}$ and see

$$\int\limits_T \tilde{\varphi}_{p_i}(x_1,x_2)\, dS = \frac{1}{6}$$

for every $i \in \{1,2,3\}$. With $s_i^{\mathrm{PEM}} = u^{\mathrm{PEM}}(p_i)$, we deduce

$$\sum_{i=1}^{3} (u^{\mathrm{PEM}}(p_i) \cdot \int\limits_T \tilde{\varphi}_{p_i}\, dS) = \sum_{i=1}^{3} \frac{u^{\mathrm{PEM}}(p_i)}{6}.$$

We thus have

$$\int\limits_T u^{\mathrm{PEM}} \circ \mu\, dS = \sum_{i=1}^{3} \frac{u^{\mathrm{PEM}}(p_i)}{6}$$

with $|T| = \frac{1}{2}$ that

$$\frac{\int\limits_T u^{\mathrm{PEM}} \circ \mu\, dS}{|T|} = \frac{\sum\limits_{i=1}^{3} u^{\mathrm{PEM}}(p_i)}{3}.$$

We conclude with

$$\frac{\int\limits_{e_l} u^{\mathrm{PEM}}(x)\,dS}{|e_l|} = \frac{\int\limits_{T} u^{\mathrm{PEM}} \circ \mu\,dS}{\underbrace{|e_l| \cdot C^{-1}}_{=|T|}} = \frac{\sum\limits_{i=1}^{3} u^{\mathrm{PEM}}(p_i)}{3}$$

and with the affine linearity of u^{PEM} this shows

$$\frac{\sum\limits_{i=1}^{3} u^{\mathrm{PEM}}(p_i)}{3} = u^{\mathrm{PEM}}(\sum_{i=1}^{3} \frac{1}{3} p_i) = u^{\mathrm{PEM}}(x_l)$$

with x_l being the center of the single face of the electrode interface e_l. So, this shows that for a single face as the electrode interface, the set codimension $c = 1$, and $\lambda \to \infty$, the PEM and the CEM are identical.

Bibliography

[1] A. Antal et al. “Low intensity transcranial electric stimulation: Safety, ethical, legal regulatory and application guidelines”. In: *Clinical Neurophysiology* 128.9 (2017), pp. 1774–1809. DOI: `https://doi.org/10.1016/j.clinph.2017.06.001`.

[2] Dietrich Braess. *Finite Elements: Theory, Fast Solvers, and Applications in Solid Mechanics*. 3rd ed. Cambridge University Press, 2007.

[3] Susanne C. Brenner and Larkin R. Scott. *The Mathematical Theory of Finite Element Methods*. Vol. 15. Texts in Applied Mathematics. Springer, 2008. DOI: `10.1007/978-0-387-75934-0`.

[4] Destexhe A Brette R. *Handbook of Neural Activity Measurement*. Cambridge University Press, 2012.

[5] Christopher R. Butson, Christopher B. Maks, and Cameron C. McIntyre. “Sources and effects of electrode impedance during deep brain stimulation”. In: *Clinical Neurophysiology* 117.2 (2006), pp. 447–454. DOI: `https://doi.org/10.1016/j.clinph.2005.10.007`.

[6] Volker A. Coenen et al. “Deep Brain Stimulation in Neurological and Psychiatric Disorders”. In: *Dtsch Arztebl Int* 112.31-32 (Aug. 2015), pp. 519–526. DOI: `10.3238/arztebl.2015.0519`.

[7] O. Elyamany et al. “Transcranial alternating current stimulation (tACS): from basic mechanisms towards first applications in psychiatry”. In: *European Archives of Psychiatry and Clinical Neuroscience* 271 (2021), pp. 135–156. DOI: `10.1007/s00406-020-01209-9`.

[8] Christian Engwer et al. “A Discontinuous Galerkin Method to Solve the EEG Forward Problem Using the Subtraction Approach”. In: *SIAM Journal on Scientific Computing* 39.1 (2017), B138–B164. DOI: `10.1137/15M1048392`.

[9] Tim Erdbrügger et al. “CutFEM forward modeling for EEG source analysis”. In: *Frontiers in Human Neuroscience* Volume 17 - 2023 (2023). DOI: `10.3389/fnhum.2023.1216758`.

[10] Lawrence C. Evans. *Partial differential equations*. Providence, R.I.: American Mathematical Society, 2010.

[11] Otto Forster. *Analysis 3: Maß- und Integrationstheorie, Integralsätze im $\mathbb{R}^n$ und Anwendungen*. 8th ed. Aufbaukurs Mathematik. 38 b/w illustrations, eBook ISBN: 978-3-658-16746-2, Published: 24 January 2017. Springer Spektrum Wiesbaden, 2017, pp. VIII + 312. DOI: `10.1007/978-3-658-16746-2`.

[12] Alexander Frank. *Sensitivity of Optimization in Transcranial Direct Current Stimulation to Electrode Modeling.* Master's thesis. Available at `https://www.sci.utah.edu/~wolters/PaperWolters/2022/MasterFrank.pdf`. Mar. 2022.

[13] Christophe Geuzaine and Jean-François Remacle. "Gmsh: A 3-D finite element mesh generator with built-in pre- and post-processing facilities". In: *International Journal for Numerical Methods in Engineering* 79.11 (May 2009), pp. 1309–1331. DOI: `https://doi.org/10.1002/nme.2579`.

[14] *GitLab branch feature/complete_electrode_model of the project duneuro in which the CEM is implemented and included into.* URL: `https://gitlab.dune-project.org/duneuro/duneuro/-/tree/feature/complete_electrode_model/duneuro?ref_type=heads`.

[15] *Gmsh 4.13.1.* May 2025. URL: `https://gmsh.info/doc/texinfo/gmsh.html`.

[16] David J Griffiths. *Introduction to electrodynamics; 4th ed.* Re-published by Cambridge University Press in 2017. Boston, MA: Pearson, 2013. DOI: `1108420419`.

[17] Florian Grüne. *Validierung von FEM-Ansätzen höherer Ordnung für das EEG-Vorwärtsproblem.* Master's thesis. Available at `https://www.sci.utah.edu/~wolters/PaperWolters/2014/MasterGruene.pdf`. Aug. 2014.

[18] Matti Hämäläinen et al. "Magnetoencephalography-theory,instrumentation, and applications to noninvasive studies of the working human brain". In: *Reviews of modern Physics* 65 (1993), pp. 413–497.

[19] Martin Hanke, Bastian Harrach, and Nuutti Hyvönen. "Justification of point electrode models in electrical impedance tomography". In: *Mathematical Models and Methods in Applied Sciences* 21 (June 2011), pp. 1395–1413.

[20] Malte B. Höltershinken et al. "The Local Subtraction Approach for EEG and MEG Forward Modeling". In: *SIAM Journal on Scientific Computing* 47.1 (Feb. 2025), B160–B189. DOI: `10.1137/23M1582874`.

[21] Malte Bernhard Höltershinken. *Efficient Computation of Transfer Matrices using the Block Conjugate Gradient Method.* Master's thesis. Available at `https://www.sci.utah.edu/~wolters/PaperWolters/2021/MasterHoeltershinken.pdf`. Sept. 2021.

[22] Malte Bernhard Höltershinken. "New mathematics for the EEG and MEG forward and inverse problems, and application to the tDCS stimulation of two epilepsy patients". PhD thesis, in preparation. 2025.

[23] Girish Katti, Syeda Ara, and Dr Shireen. "Magnetic resonance imaging (MRI) - A review". In: *Intl J Dental Clin* 3 (Mar. 2011).

[24] Asad Khan et al. "Can individually targeted and optimized multi-channel tDCS outperform standard bipolar tDCS in stimulating the primary somatosensory cortex?" In: *Brain Stimulation* 16.1 (2023), pp. 1–16. DOI: `https://doi.org/10.1016/j.brs.2022.12.006`.

[25] Asad Khan et al. "Individually optimized multi-channel tDCS for targeting somatosensory cortex". In: *Clinical Neurophysiology* 134 (2022), pp. 9–26. DOI: `https://doi.org/10.1016/j.clinph.2021.10.016`.

[26] J. Kybic et al. “A common formalism for the Integral formulations of the forward EEG problem”. In: *IEEE Transactions on Medical Imaging* 24.1 (2005), pp. 12–28. DOI: `10.1109/TMI.2004.837363`.

[27] Heinrich Mattle. *Fundamentals of neurology.* 2nd. Delhi: Thieme, 2017.

[28] Oriano Mecarelli, ed. *Clinical Electroencephalography.* 1st ed. 343 b/w illustrations, 383 colour illustrations. Topics: Neurology, Anesthesiology, Intensive / Critical Care Medicine, Psychiatry. Springer Cham, 2019, pp. XIX+822. DOI: `10.1007/978-3-030-04573-9`.

[29] Tuuli Miinalainen et al. “A realistic, accurate and fast source modeling approach for the EEG forward problem”. In: *NeuroImage* 184 (2019), pp. 56–67. DOI: `https://doi.org/10.1016/j.neuroimage.2018.08.054`.

[30] J.C. de Munck, B.W. van Dijk, and H. Spekreijse. “Mathematical dipoles are adequate to describe realistic generators of human brain activity”. In: *IEEE Transactions on Biomedical Engineering* 35.11 (1988), pp. 960–966. DOI: `10.1109/10.8677`.

[31] Frank Neugebauer et al. “Validating EEG, MEG and Combined MEG and EEG Beamforming for an Estimation of the Epileptogenic Zone in Focal Cortical Dysplasia”. In: *Brain Sciences* 12.1 (2022). DOI: `10.3390/brainsci12010114`.

[32] Michael A. Nitsche et al. “Transcranial direct current stimulation: State of the art 2008”. In: *Brain Stimulation* 1.3 (2008), pp. 206–223. DOI: `https://doi.org/10.1016/j.brs.2008.06.004`.

[33] Andreas Nüßing. “Fitted and Unfitted Finite Element Methods for Solving the EEG Forward Problem”. English. Dissertation. Westfälische Wilhelms-Universität Münster, 2018.

[34] I. Oguz Tanzer et al. “Representation of bioelectric current sources using Whitney elements in the finite element method”. In: *Physics in Medicine Biology* 50.13 (June 2005), p. 3023. DOI: `10.1088/0031-9155/50/13/004`.

[35] Oula Puonti et al. “Accurate and robust whole-head segmentation from magnetic resonance images for individualized head modeling”. In: *NeuroImage* 219 (2020), p. 117044. DOI: `https://doi.org/10.1016/j.neuroimage.2020.117044`.

[36] S Pursiainen. “EEG/MEG forward simulation through h- and p-type finite elements”. In: *Journal of Physics: Conference Series* 124.1 (July 2008), p. 012041. DOI: `10.1088/1742-6596/124/1/012041`.

[37] S Pursiainen, F Lucka, and C H Wolters. “Complete electrode model in EEG: Relationship and differences to the point electrode model”. In: *Physics in Medicine Biology* 57.4 (Feb. 2012), pp. 999–1017. DOI: `10.1088/0031-9155/57/4/999`.

[38] S. Pursiainen, S. Lew, and C. H. Wolters. “Forward and inverse effects of the complete electrode model in neonatal EEG”. In: *Journal of Neurophysiology* 117.3 (2017). PMID: 27852731, pp. 876–884. DOI: `10.1152/jn.00427.2016`.

[39] S. Pursiainen et al. “Advanced Boundary Electrode Modeling for tES and Parallel tES/EEG”. In: *IEEE Transactions on Neural Systems and Rehabilitation Engineering* 26.1 (Jan. 2018). Epub 2017 Sep 28, pp. 37–44. DOI: `10.1109/TNSRE.2017.2748930`.

[40] Dale Purves et al. *Neuroscience*. Sinauer Associates, 2004.

[41] Walter Rudin. *Functional Analysis*. 2nd. New York: McGraw-Hill, 1991.

[42] J. W. Ruge and K. Stüben. "4. Algebraic Multigrid". In: *Multigrid Methods*, pp. 73–130. DOI: `10.1137/1.9781611971057.ch4`.

[43] L Ruthotto et al. "Diffeomorphic susceptibility artifact correction of diffusion-weighted magnetic resonance images". In: *Physics in Medicine Biology* 57.18 (Sept. 2012), p. 5715. DOI: `10.1088/0031-9155/57/18/5715`.

[44] Yousef Saad. *Iterative methods for sparse linear systems*. SIAM, 2003, pp. I–XVIII, 1–528.

[45] Oliver Sander. *DUNE—The Distributed and Unified Numerics Environment*. Springer, 2020.

[46] J Sarvas. "Basic mathematical and electromagnetic concepts of the biomagnetic inverse problem". In: *Physics in Medicine Biology* 32.1 (Jan. 1987), p. 11. DOI: `10.1088/0031-9155/32/1/004`.

[47] Sophie Schrader et al. "DUNEuro—A software toolbox for forward modeling in bioelectromagnetism". In: *PLOS ONE* 16.6 (June 2021), pp. 1–21. DOI: `10.1371/journal.pone.0252431`.

[48] Andreas Schulze-Bonhage et al. "Focal Cortex Stimulation With a Novel Implantable Device and Antiseizure Outcomes in 2 Prospective Multicenter Single-Arm Trials". In: *JAMA Neurology* 80.6 (June 2023), pp. 588–596. DOI: `10.1001/jamaneurol.2023.0066`.

[49] Andreas Schulze-Bonhage et al. "Two-year outcomes of epicranial focal cortex stimulation in pharmacoresistant focal epilepsy". In: *Epilepsia* n/a.n/a (). DOI: `https://doi.org/10.1111/epi.18448`.

[50] *seaborn.boxplot*. July 2025. URL: `https://seaborn.pydata.org/generated/seaborn.boxplot.html#seaborn.boxplot`.

[51] Aashit K. Shah and Sandeep Mittal. "Invasive electroencephalography monitoring: Indications and presurgical planning". In: *Annals of Indian Academy of Neurology* 17.Suppl 1 (2014), S89–S94. DOI: `10.4103/0972-2327.128668`.

[52] Sara Simula et al. "Transcranial current stimulation in epilepsy: A systematic review of the fundamental and clinical aspects". In: *Frontiers in Neuroscience* Volume 16 - 2022 (2022). DOI: `10.3389/fnins.2022.909421`.

[53] Erkki Somersalo, Margaret Cheney, and David Isaacson. "Existence and Uniqueness for Electrode Models for Electric Current Computed Tomography". In: *SIAM Journal on Applied Mathematics* 52.4 (1992), pp. 1023–1040. DOI: `10.1137/0152060`.

[54] David S. Tuch et al. "Conductivity tensor mapping of the human brain using diffusion tensor MRI". In: *Proceedings of the National Academy of Sciences* 98.20 (2001), pp. 11697–11701. DOI: `10.1073/pnas.171473898`.

[55] Sylvain Vallaghé, Théodore Papadopoulo, and Maureen Clerc. "The adjoint method for general EEG and MEG sensor-based lead field equations". In: *Physics in Medicine Biology* 54.1 (Dec. 2008), p. 135. DOI: `10.1088/0031-9155/54/1/009`.

[56] J. Vorwerk et al. “A Mixed Finite Element Method to Solve the EEG Forward Problem”. In: *IEEE Transactions on Medical Imaging* 36.4 (2017), pp. 930–941. DOI: `10.1109/TMI.2016.2624634`.

[57] Johannes Vorwerk et al. “A guideline for head volume conductor modeling in EEG and MEG”. In: *NeuroImage* 100 (2014), pp. 590–607. DOI: `https://doi.org/10.1016/j.neuroimage.2014.06.040`.

[58] Johannes Vorwerk et al. “The multipole approach for EEG forward modeling using the finite element method”. In: *NeuroImage* 201 (2019), p. 116039. DOI: `https://doi.org/10.1016/j.neuroimage.2019.116039`.

[59] S Wagner et al. “Investigation of tDCS volume conduction effects in a highly realistic head model”. In: *Journal of Neural Engineering* 11.1 (Dec. 2013), p. 016002. DOI: `10.1088/1741-2560/11/1/016002`.

[60] S. Wagner et al. “Using reciprocity for relating the simulation of transcranial current stimulation to the EEG forward problem”. In: *NeuroImage* 140 (2016). Transcranial electric stimulation (tES) and Neuroimaging, pp. 163–173. DOI: `https://doi.org/10.1016/j.neuroimage.2016.04.005`.

[61] S. Wagner et al. “Using reciprocity for relating the simulation of transcranial current stimulation to the EEG forward problem”. In: *NeuroImage* 140 (Apr. 2016). DOI: `10.1016/j.neuroimage.2016.04.005`.

[62] C H Wolters, L Grasedyck, and W Hackbusch. “Efficient computation of lead field bases and influence matrix for the FEM-based EEG and MEG inverse problem”. In: *Inverse Problems* 20.4 (May 2004), p. 1099. DOI: `10.1088/0266-5611/20/4/007`.

[63] C. H. Wolters et al. “Numerical Mathematics of the Subtraction Method for the Modeling of a Current Dipole in EEG Source Reconstruction Using Finite Element Head Models”. In: *SIAM Journal on Scientific Computing* 30.1 (2008), pp. 24–45. DOI: `10.1137/060659053`.

[64] A.J. Woods et al. “A technical guide to tDCS, and related non-invasive brain stimulation tools”. In: *Clinical Neurophysiology* 127.2 (2016), pp. 1031–1048. DOI: `https://doi.org/10.1016/j.clinph.2015.11.012`.

[65] Shasha Wu et al. “Depth versus surface: A critical review of subdural and depth electrodes in intracranial electroencephalographic studies”. In: *Epilepsia* 65.7 (2024), pp. 1868–1878. DOI: `https://doi.org/10.1111/epi.18002`.